Book of Abstracts

THE 47TH ANNUAL SYMPOSIUM ON POLYMER SCIENCE/ENGINEERING

University of Waterloo

Waterloo, Ontario

April 30th– May 1st, 2025

Institute for Polymer Research

University of Waterloo

The Institute for Polymer Research would like to thank the sponsors for their support of the symposium.

2025

PROGRAM

INSTITUTE FOR POLYMER RESEARCH
CELEBRATING 41 YEARS OF OFFICIAL INSTITUTE STATUS
FORTY-SEVENTH ANNUAL SYMPOSIUM
ON POLYMER SCIENCE/ENGINEERING 2025
E7 7303-7363
Faculty Hall
University of Waterloo, Waterloo, Ontario
Wednesday April 30 and Thursday May 1, 2024

8:45 a.m.	**Open Symposium Portal**
8:50	**Welcome and Opening Remarks**
9:00 – 9:20	**Negin Bouzari (Prof. Shahsavan), Chem Eng, Waterloo** Novel Small-Scale Robots for Medical Applications **(Winner of 2024 IPR Award for Academic Excellence in Polymer Science/Engineering)**
9:20 – 10:00	**Industry Speaker: Dr. Nicholas Lanigan, Davwire.** Formulation of Photocurable Resins for the Fabrication of Ferroelectrets
10:00 – 10:20	**5-Min. Mini Presentations** **1) Periklis Alikiotis (Prof. Mekonnen)** Utilizing Lignin as a Sustainable Filler of Polyvinyl Chloride (PVC) Composites: Effects of Ash Content and Loading Levels on Thermomechanical and Combustion Properties **2) Tobechukwu Ohaka (Prof. Mekonnen)** Recyclable and Sustainable Natural Rubber Biocomposite Vitrimers Induced by Dynamic Anhydride-Epoxy Bonds **3) Lauren DiLoreto (Prof. Lin)** Upcycling of Polyolefins into Stress-Responsive Materials **4) Saba Karimi (Prof. Forrest)** Two Relaxation Mechanisms for Rejuvenation of Stable Polystyrene Glass
10:20 – 10:40	**Coffee**
10:40 – 11:00	**Mahnoor Mehmood (Prof. Forrest)** Characterization of Polymer Stable Glasses
11:00 – 11:20	**Ashna Rajeev (Prof. Zhao)** Nanochitin as a Strength Enhancing Agent for Paper-Based Packaging Material
11:20 – 11:40	**Matthew Scarfo (Prof. Shahsavan)** Microscale Photolithography of LCE Soft Actuators and Robots with Magnetically Driven, Discretized Alignment Domains

11:40 – 12:00 **Lu Yin (Prof. Zhao)**
Polypyrrole/Rubber Composite Latex as High-Performance Sustainable Conductive Coating

12:00 – 12:50 **Lunch**

12:50 – 1:30 **Academic presenter: Prof. Megan Roberts, Western**
Nanocellulose for Precision Applications: Combatting Challenges Using Intentional Surface Chemistry Design

1:30 – 1:50 **Franklin Frasca (Prof. Duhamel)**
Probing the Encounter Dynamics between the Side Chains of Small Multifunctional Macromolecules by Pyrene Excimer Formation

1:50 – 2:10 **5-Min. Mini Presentations**

5) **Iris Samputu (Prof. Feng)**
Dehydration of ethylene glycol and gases through the use of polymeric and novel polymer blend membranes

6) **Jinxuan Zhang (Prof. Feng)**
Interfacially crosslinked poly(vinyl alcohol)/poly(vinyl amine) composite membranes incorporated with silver for facilitated olefin/paraffin separation

7) **Hossein Hipakchi (Prof. Mekonnen)**
Direct Ink Writing for Conductive 3D-Printed Healthcare Sensors: Design and Fabrication

8) **Jimmy Papazotos (Prof. Li)**
Novel Polymer Semiconductor Design for Low Level Gas Detection

2:10 – 2:30 **Carlos Villafane (Prof. Kamkar)**
Eco-Friendly Electrochemically Synthesized Graphene/Sodium Alginate Inks for 3D Printing Highly Conductive Hydrogels and Aerogels

2:30 – 2:50 **Junhao Hu (Prof. Schipper)**
Harnessing Light: Exploring Pyrazine Polymers for Single-Molecule Organic Solar Cells

2:50 – 3:10 **Yonglin Wang (Prof. Li), Chem Eng, Waterloo**
Development of High-Performance Organic Cathode Materials Based on Coordination Polymers for Lithium-Ion Batteries
(Winner of the 2023 IPR Award for Academic Excellence in Polymer Science/Engineering)

3:10 – 3:40 **Coffee**

3:40 – 4:00 **Donghan Liu (Prof. Duhamel)**
Interactions of Hydrophobically Modified PAMAM Dendrimers with Surfactant Aggregates Probed by Pyrene Excimer Formation

4:00 – 4:20 **Akliu Getnet (Prof. Mekonnen)**
Lead free single and dual filler loaded nanocomposites for X-ray radiation shielding

4:20 – 4:40 **Kristijan Lulic (Prof. Duhamel)**
Improving the Sensitivity of Pyrene Excimer Formation for Persistence Length Determination of Poly(alkyl methacrylate)s

4:40 – 5:00 **Evangelin Sridhar (Prof. Simon)**
Kinetics of bio polyesters

5:00 – 5:20 **Hunter Little (Prof. Duhamel)**
Using Time-Resolved Fluorescence to Gain New Insights into the Conformation of DNA Aptamers

5:20 – 5:40 **Autumn Cheon (Prof. Tam)**
Sustainable Air Filtration Materials Using Biomacromolecular Nanomaterials

5:40 – 6:05 **5-Min. Mini Presentations**

9) **Noah Gallant**
Characterizing the Size and Structure of Pyrene-Tagged SDS and DTAB Micelles

10) **Drew Davidson (Prof. Kamkar)**
Protecting Firefighters from Cancer through Multifunctional Electrospun Nanocomposites

11) **Karthick Raj Selvam (Prof. Mekonnen)**
Silk Nanofibers for Drug Delivery: A Solution Blow Spinning Approach

12) **Maggie Wong (Prof. Prince)**
Engineering Biomimetic Strain-Stiffening into Polyacrylamide Hydrogels

13) **Dylan McQuarrie (Prof. Prince)**
Leveraging Diels-Alder Adducts for Recyclable Thermosets

6:05 – 6:10 **Closing remarks**

Thursday May 1, 2025
(E7 7303-7363)

8:45 a.m.	**Open Symposium Portal**
8:50	**Welcome and Opening Remarks**
9:00 – 9:50	**Prof. Leonardo Simon, Chem Eng, Waterloo** Industrial Hemp and Development of Sustainable Materials
9:50 – 10:40	**Prof. Xianshe Feng, Chem Eng, Waterloo** Mass Transfer in Pervaporation, Perstraction and Sorption - A Unified Approach
10:40 – 11:00	**Coffee**
11:00 – 11:50	**Prof. Tizazu Mekonnen, Chem Eng, Waterloo** Engineered Polysaccharides and the Modification of Polysaccharides and Poly(lactic acid) for Sustainable Multiphase Polymer Development
11:50 – 11:55	**Closing remarks**

NEGIN BOUZARI
Chem. Eng.
Waterloo

Novel Small-Scale Robots for Medical Applications

Winner of the 2023 IPR Award for Academic Excellence in Polymer Science/Engineering

Novel Small-Scale Robots for Medical Applications

Negin Bouzari[1] and Hamed Shahsavan[1,*]

Abstract
Stimuli-responsive hydrogels have attracted significant attention as a versatile class of soft actuators. Introducing anisotropic properties and shape-change programmability to responsive hydrogels promises a host of opportunities in the development of soft robots. Herein, we report the synthesis and shape-change programming of a hydrogel nanocomposite with multimodal stimulus-response, achieved by introducing anisotropic swelling and mechanical properties through the creation of microstructural and macrostructural anisotropy. Our hydrogel nanocomposites are biocompatible and have tunable mechanical properties. Additionally, their shape-change programmability can be leveraged to create hydrogel constructs capable of performing untethered robotic tasks, such as cargo transport and delivery. We believe the proposed material system holds promise for the development of future surgical microrobots for functioning in confined biological environments where operation of traditional surgical tools is challenging.

Key Words*:* Shape-Change Programming, Stimuli-Responsive Hydrogels, Structural Anisotropy, Soft Robotics

Introduction

Over the past decade, there has been a growing interest in small-scale soft robots due to their potential for minimally invasive medical interventions such as biopsy, targeted drug delivery, and single-cell transport in hard-to-reach biological environments [1], [2]. Soft robots are designed with mechanical properties similar to targeted native tissues, which reduces the risk of tissue damage upon contact. But fabricating small-scale soft robots requires overcoming challenges related to minimizing the size of onboard components like power sources, sensors, and actuators. Researchers in soft robotics have explored the use of stimulus-responsive soft materials with integrated sensing, energy transduction, and actuation capabilities to address these challenges. Stimulus-responsive materials can sense specific environmental cues and respond by changing their properties, a process known as energy transduction. For instance, hydrogels with acrylate chemistry can respond to pH changes by expanding or shrinking, transforming chemical energy into mechanical energy [3]. To operate effectively, shape-change programming, which is the ability of soft robots to leverage the energy transduction capability to fulfill a specific function by undergoing a predetermined shape change, is necessary. Creating structural anisotropy at micro and macro scales is commonly used to provide stimulus-responsive materials with shape-change programming [4], [5]. Among these materials, hydrogel actuators stand out due to their high-water content and compatibility with natural tissues. Here, we introduce a novel stimuli-responsive, biocompatible, and self-healing hydrogel system. Shape-change programming is achieved through structural anisotropy, which at the microscale, is enabled by incorporation and preferential alignment of anisotropic cellulose nanocrystals (CNCs) [3], and at the macroscale, is achieved by employing a cut-and-paste technique to create multi-layered structures. Such anisotropic structures bestow hydrogels with differential swelling, in-plane and across the thickness [6], and as a result, anisotropic shape transformations such as twisting or bending are observed upon exposure to environmental stimuli. Furthermore, these hydrogels have magneto-active properties due to the inclusion of magnetic iron oxide nanoparticles (MNPs), enabling remote magnetic navigation in confined environments. We demonstrate proof-of-concept robotic functions by designing untethered soft grippers capable of performing predicted shape-changes in response to external stimulation. Our findings provide insights into designing adaptable hydrogel nanocomposites and shape-change programming strategies for developing untethered small-scale soft robots with diverse functionalities.

System Concept

[1] Department of Chemical Engineering, University of Waterloo, Waterloo, ON N2L 3G1, Canada.
[*] hshahsav@uwaterloo.ca

In this work, we synthesized stimuli-responsive hydrogels with programmable shape-changes.. The hydrogels were synthesized by copolymerizing 3-dimethyl (methacryloyloxyethyl) ammonium propanesulfonate (DMAPS) and methacrylic acid (MAA). Incorporating sulfobetaine methacrylates like DMAPS with a small proportion of MAA has been recognized to enhance the resulting hydrogel's mechanical properties [7]. This improvement stems from hydrophobic associations facilitated by the CH_3 groups in MAA. The resultant zwitterionic hydrogels exhibit self-healing properties due to dynamic electrostatic interactions between oppositely charged groups and hydrogen bonding [8], [9]. Moreover, DMAPS-MAA copolymers are notably sensitive to variations in pH and ionic strength of the environment, making them ideal building blocks for stimulus-responsive shape-morphing soft robots [3], [10]. At elevated pH levels exceeding 4.7 (beyond the acid dissociation constant of MAA), the ionization of COOH groups in MAA leads to repulsion among the charged COO^- groups, causing hydrogel swelling. This process reverses at lower pH levels. Additionally, for hydrogels rich in DMAPS, a spike in environmental salinity leads oppositely charged ions in the surrounding to neutralize some of the $NH4^+$ and $SO3^-$ groups of DMAPS and to loosen the hydrogel network due to the reduction of electrostatic interactions, which manifests in increased water uptake and volume. In contrast, for hydrogels rich in MAA, a spike in environmental salinity leads to the osmotic pressure difference between the hydrogels and the surrounding medium causing water to expel out from the network, which manifests in decreased water uptake and volume. N, N′-methylenebis(acrylamide) (BIS) is also added to our hydrogel formulation as a chemical crosslinker aiming at improving the hydrogel's integrity and mechanical properties. The system concept is demonstrated in **Figure 1 a-b**.

Microstructural Anisotropy

To introduce microstructural anisotropy to our hydrogels, we used cellulose nanocrystals (CNCs) in our formulation. CNCs are outstanding one-dimensional (1-D) materials that have garnered significant attention owing to their sustainable resources, unique mechanical properties, and surface characteristics [11]. Like other 1-D nanoparticles with high aspect ratios, CNCs can be aligned by applying external shear forces. This approach, which is versatile and compatible with extrusion 3D printing, has previously been employed to induce anisotropy in hydrogels [12], [13]. We synthesized monolithic hydrogels with microstructural anisotropy by casting the precursor onto a glass substrate and confining it with spacers. Subsequently, we applied unidirectional shear forces by moving a glass counter-substrate on top multiple times. Polymerization took place between two glass slides separated by spacers of known thickness under UV light at a wavelength of 365 nm (**Figure 1 c**). Various techniques were utilized to validate the anisotropy present in the hydrogel microstructure. Hydrogels containing CNCs exhibit transparency under natural light but exhibit vivid interference colors when examined using a polarized optical microscope (POM) (as depicted in **Figure 1 e**). Regardless of their orientation with respect to the POM's polarizer/analyzer, hydrogels containing CNCs that were not subjected to unidirectional shear forces (referred to as IGels) demonstrated a heterogeneous multicolor transmission pattern, confirming the isotropic nature of the hydrogel microstructure. This characteristic is observed when the precursor of the hydrogel is polymerized in a polydomain liquid crystalline phase. In contrast, hydrogels exposed to shear forces (referred to as AGels) displayed a uniform monochromatic transmission when viewed through the POM. The transmission through the sample, as observed via POM, is maximal when the longer side of the sample (aligned parallel to the shear direction) is positioned at a 45-degree angle with respect to the polarization axis. Conversely, the sample appears darker when aligned parallel to either the polarizer or the analyzer. This phenomenon serves as a visual indicator of the anisotropic nature of the hydrogel microstructure induced by shear forces. These results suggest that the CNCs present in hydrogel precursors indeed form a monodomain liquid crystalline phase that is aligned along the shearing direction and retained after photopolymerization. The POM image of the AGel cross-section, positioned at a 45-degree angle with respect to the polarization axis, revealed two distinct layers: one bright and one dark, confirming the presence of an anisotropy gradient along the thickness due to the motion of a glass slide on the top surface of the hydrogel precursor that generates a shear stress gradient along the thickness. However, the applied shear force was not substantial enough to align CNCs uniformly throughout the entire thickness of the precursor beyond a certain threshold,

resulting in a gradient in anisotropy. Scanning Electron Microscopy (SEM) image of the AGel surface exposed to shear before polymerization revealed microstructural alignment in the shear direction, while SEM images from its cross-section validated the POM results by showing an anisotropy gradient along the thickness. Typically, AGel samples exhibit less pronounced unidirectional microstructural anisotropy in regions farther from the shear.

Macrostructural Anisotropy

To introduce macrostructural anisotropy to our hydrogels, we used tessellation of hydrogels with different properties into multi-layer structures to program local deformations into our hydrogels (**Figure 1 d**). Interlayer adhesion is a crucial property to realize a cut-and-paste strategy for the preparation of multi-layer constructs. The abundance of zwitterionic moieties and carboxyl groups in our hydrogel formulations facilitates interlayer adhesion between layers of mismatched formulation and properties, in a mechanism similar to the self-healing of hydrogels with noncovalent physical crosslinking. In our hydrogel systems, interlayer adhesion can be obtained as dynamic hydrogen bonds and electrostatic attractions facilitate the interdiffusion of the chains across the interface and their engagement in the new bonds. We chose to use the cut-and-paste technique to combine pieces of MAA-rich (Gel1) and DMAPS-rich (Gel4) hydrogels into integrated multi-layer constructs given the reverse response of Gel1 and Gel4 to a change in environmental salinity (**Figure 1 f**). To evaluate the interlayer adhesion between Gel1 and Gel4 which is necessary for the successful fabrication of hybrid constructs, we performed tensile mechanical testing (**Figure 1 f**). For this, two hydrated hydrogel strips of Gel1 and Gel4 (equilibrated in water for 2 h) were cut in two halves. Half-strips were then overlapped, matched, or mismatched, and kept under gentle pressure. After 6 hours of healing, the stress-strain behavior of the healed samples was evaluated. Compared to the stress–strain behavior of the healed Gel4 hydrogel, the elastic modulus of the bilayer made of Gel1 and Gel4 strips has improved by 30 kPa, which can be attributed to the contribution of the stiffer Gel1 hydrogel and the thicker profile at the overlapped region. The elongation at the break of the Gel1-Gel4 bilayer hydrogel is comparable to that of Gel4. Gel1-Gel4 specimen undergoes failure at around 150% strain, far from the healed area and within the softer Gel4 half-strip. We conclude that the interlayer adhesion is at least as strong as the cohesion of the pristine Gel4 hydrogels.

Shape-Change Programming

The reversible swelling triggered by pH and ionic strength, combined with the structural anisotropy of the hydrogels, provides a robust set of adjustable parameters for programming 2D-to-3D shape-changes, such as bending. For samples with microstructural anisotropy, the unidirectional alignment of CNCs in regions closer to the top surface can guide such bending deformation in preferred directions since this system can be considered as a bimorph with nonidentical swelling behavior across the thickness, where CNCs are randomly oriented on one side and unidirectionally aligned on the other side. The side with unidirectionally aligned CNCs constrains the straining of the side with randomly oriented CNCs. As a result, while one side experiences tension, the other side undergoes compressive stresses. Releasing these internal stresses generates a bending moment, leading to the bending of the initially flat hydrogel. As shown in **Figure 1 g,** strips of AGel with CNC alignment perpendicular and parallel to their long axis exhibit reversible bending, one parallel and the other perpendicular to their long axis. The direction of bending in these strips was influenced by the larger swelling occurring perpendicular to the CNC alignment. When the angle between CNC alignment and the strip's long axis is 45 degrees, the hydrogel twists and forms a helix. Environmental pH was used to stimulate shape-changes in our hydrogels with microstructural anisotropy. For samples with macrostructural anisotropy, the extreme mismatch between expansion/contraction behaviors and stiffness of Gel1 and Gel4, as well as their great interlayer adhesion, can be employed to create tessellated constructs with differential swelling along the thickness. In, the mechanics of stimuli-triggered deformation of a bilayer, for example, Gel1–Gel4, follows Timoshenko's bimetallic theory, which captures the dependence of deformation behavior to geometrical parameters and properties of each layer and the overall bilayer construct. Shape-change programming was achieved by cutting thin hydrogel strips and pasting them to another hydrogel layer in discontinuous domains. The interplay between deformation (expansion or

shrinkage) and mechanical properties of solid backing monolayers, either Gel1 or Gel4, and those of bilayered Gel1–Gel4 domains can be exploited to design responsive constructs capable of buckling upon stimulation (**Figure 1 h**). Environmental salinity was used to stimulate shape-changes in our hydrogels with macrostructural anisotropy.

Cytocompatibility

To assess the potential of our hydrogels for biomedical applications, we investigated their cytotoxicity properties. A live/dead assay was employed for this purpose, and cell proliferation was monitored using fluorescence microscopy over 5 days. The results from the live/dead assay revealed that cell viability remained very high, consistently above 95%, throughout the 5-day incubation period alongside the hydrogels, confirming their cytocompatibility (**Figure 1 i**).

Soft Robotic Applications

After demonstrating the shape-change programmability and biocompatibility of our hydrogels, we proceeded to design miniature grippers that are responsive to pH and ionic strength as a proof-of-concept for untethered robotic applications. We fabricated miniature robots that can be navigated magnetically to transfer a very light cargo in a confined and flooded space resembling a maze (**Figure 1 j**). When the robot encounters a high pH environment (**Figure 1 k**) or high ionic strength (**Figure 1 l**), it twists around the cargo to securely grasp it. Conversely, lowering the pH/salinity causes the twists to open, thus releasing the cargo. To enable remote navigation, we attached a patch of hydrogel containing MNPs to the robot, which enables magnetic navigation of the robot using a strong permanent magnet from outside of the workspace. This innovative approach showcases the potential applications of our hydrogels in untethered robotic systems.

Conclusion

In summary, we have successfully developed shape-morphing hydrogel nanocomposites by introducing structural anisotropy within stimuli-responsive hydrogels at micro and macro scales. Through this process, we introduced hydrogels that exhibit differential swelling and anisotropic mechanical properties, which are crucial for programmable shape-change capabilities. These hydrogel systems have demonstrated sensitivity to environmental changes such as pH and ionic strength, while also exhibiting high cytocompatibility, making them a promising material system for applications in biomedical robotics. As a proof of concept for their potential robotic applications, we designed and implemented small-scale robots capable of navigating and maneuvering in confined spaces using a magnetic field. These robots are capable of remote delivery of light cargoes. These advancements represent a significant step forward in enhancing the adaptability of biomimetic soft robots. Furthermore, the unique characteristics of our hydrogel precursor, including its shear-thinning rheology, photocurable nature, and low cytotoxicity, present exciting opportunities for developing inks suitable for advanced manufacturing techniques such as 3D bioprinting, stereolithography, direct laser writing, and two-photon polymerization at submillimeter scales.

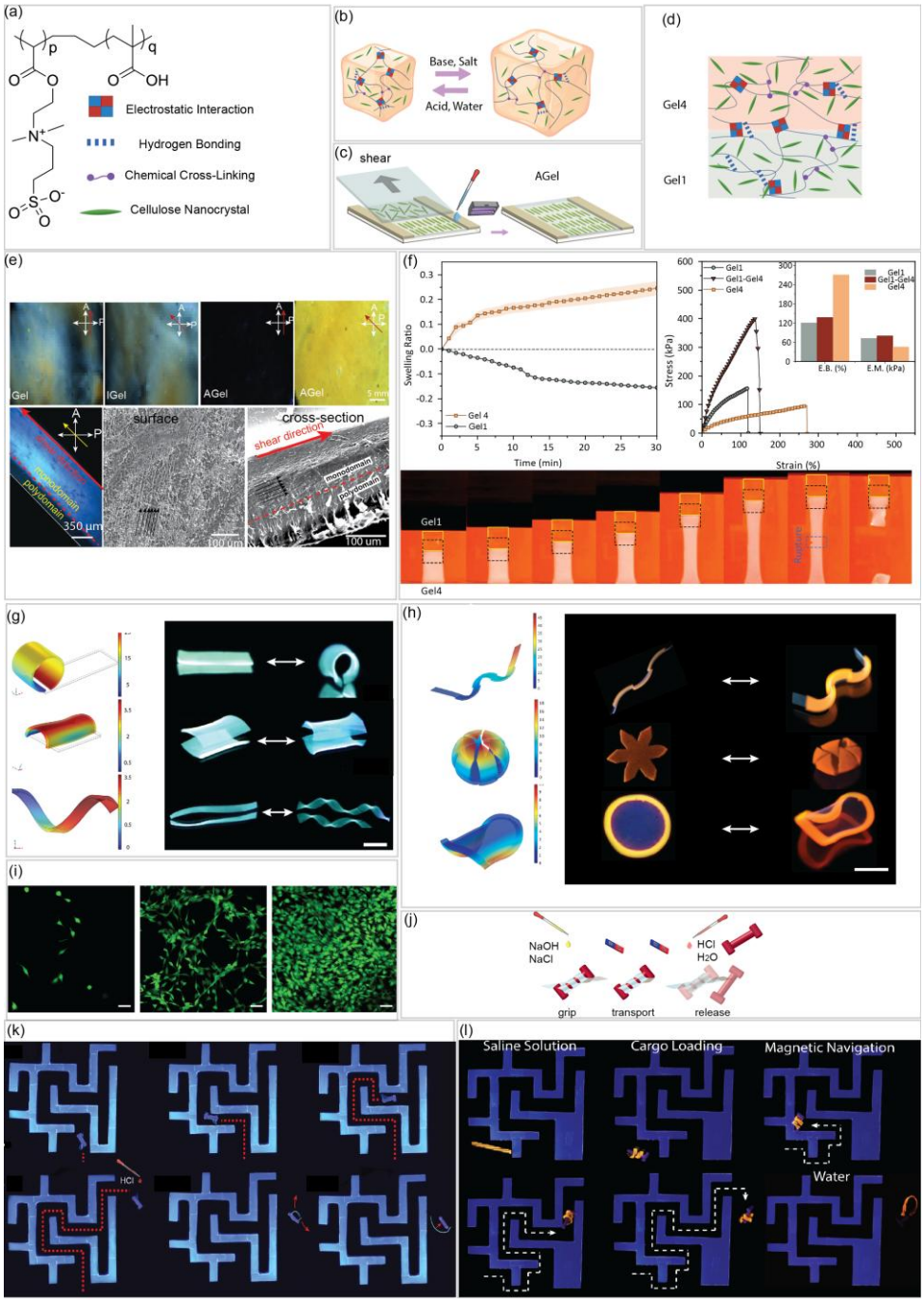

Figure 1. Stimuli-responsive, programmable, and self-healing hydrogels for small-scale robotic applications. a) Chemical structure of the hydrogel copolymer. b) Schematic representation of stimuli-responsiveness of hydrogels. c) Schematic representation of using unidirectional shear force to introduce microstructural anisotropy in the hydrogel. d) Schematic representation of using multilayering technique to introduce macrostructural anisotropy in the hydrogel. e) Investigation of microstructural anisotropy using optical analysis. f) Investigation of swelling and mechanical properties and inter layer adhesion of different hydrogels used in multilayered hydrogel constructs. g) Shape-change programming of monolithic hydrogels with microstructural anisotropy in response to changes of the environmental pH. The scale bar is 10 mm. h) Shape-change programming of heterolithic hydrogels with macrostructural anisotropy in response to changes of the environmental ionic strength. The scale bar is 20 mm. i) Proliferation of the incubated Fibroblast cells with hydrogels on day1, 3, and 5 of incubation. The scale bar is 50 µm. j) Schematic representation of using stimuli-responsive hydrogels for cargo delivery. k) Demonstration of the robotic functionality of the monolithic hydrogels through shape-change programming and magnetic navigation in a confined environment. l) Demonstration of the robotic functionality of the heterolithic hydrogels through shape-change programming and magnetic navigation in a confined environment.

References:

[1] M. Li, A. Pal, A. Aghakhani, A. Pena-Francesch, and M. Sitti, "Soft actuators for real-world applications," *Nature Reviews Materials*, vol. 7, no. 3, pp. 235–249, Nov. 2021, doi: 10.1038/s41578-021-00389-7.

[2] A. W. Feinberg, "Biological Soft Robotics.," *Annual review of biomedical engineering*, vol. 17, pp. 243–265, 2015, doi: 10.1146/annurev-bioeng-071114-040632.

[3] N. Bouzari et al., "Programmable nanocomposites of cellulose nanocrystals and zwitterionic hydrogels for soft robotics," *Nat Commun*, vol. 14, no. 1, p. 6108, 2023.

[4] A. Nojoomi, J. Jeon, and K. Yum, "2D material programming for 3D shaping," *Nature Communications*, vol. 12, no. 1, p. 603, 2021.

[5] H. Arslan, A. Nojoomi, J. Jeon, and K. Yum, "3D Printing of Anisotropic Hydrogels with Bioinspired Motion," *Advanced Science*, vol. 6, no. 2, p. 1800703, Jan. 2019, doi: 10.1002/advs.201800703.

[6] N. Bouzari et al., " Hybrid Zwitterionic Hydrogels with Encoded Differential Swelling and Programmed Deformation for Small-scale Robotics," *Small Methods*, 2024.

[7] Z. Lei and P. Wu, "Zwitterionic Skins with a Wide Scope of Customizable Functionalities," *ACS Nano*, vol. 12, no. 12, pp. 12860–12868, Dec. 2018, doi: 10.1021/acsnano.8b08062.

[8] H. Liu, C. Xiong, Z. Tao, Y. Fan, X. Tang, and H. Yang, "Zwitterionic copolymer-based and hydrogen bonding-strengthened self-healing hydrogel," *RSC Advances*, vol. 5, no. 42, pp. 33083–33088, 2015, doi: 10.1039/c4ra15003a.

[9] R. Nasseri et al., "Programmable nanocomposites of cellulose nanocrystals and zwitterionic hydrogels for soft robotics," *Nature Communications*, vol. 14, no. 1, p. 6108, Sep. 2023, doi: 10.1038/s41467-023-41874-7.

[10] F. Çalılı, P. Kaner, G. Aro, A. Asatekin, and P. Z. Çulfaz-Emecen, "Ionic strength-responsive poly(sulfobetaine methacrylate) microgels for fouling removal during ultrafiltration," *React Funct Polym*, vol. 156, no. August, p. 104738, 2020, doi: 10.1016/j.reactfunctpolym.2020.104738.

[11] R. Nasseri, C. P. Deutschman, L. Han, M. A. Pope, and K. C. Tam, "Cellulose nanocrystals in smart and stimuli-responsive materials: a review," *Materials Today Advances*, vol. 5, p. 100055, 2020, doi: 10.1016/j.mtadv.2020.100055.

[12] H. Bai, A. Polini, B. Delattre, and A. P. Tomsia, "Thermoresponsive composite hydrogels with aligned macroporous structure by ice-templated assembly," *Chemistry of Materials*, vol. 25, no. 22, pp. 4551–4556, Nov. 2013, doi: 10.1021/cm4025827.

[13] R. Dai, L. Meng, Q. Fu, S. Hao, and J. Yang, "Fabrication of Anisotropic Silk Fibroin-Cellulose Nanocrystals Cryogels with Tunable Mechanical Properties, Rapid Swelling, and Structural Recoverability via a Directional-Freezing Strategy," *ACS Sustainable Chemistry and Engineering*, vol. 9, no. 36, pp. 12274–12285, Sep. 2021, doi: 10.1021/acssuschemeng.1c03852.

DR. NICHOLAS LANIGAN
Industry Speaker
Davwire

Formulation of Photocurable Resins for the Fabrication of Engineered Ferroelectrets

Formulation of Photocurable Resins for the Fabrication of Engineered Ferroelectrets

Engineered ferroelectrets are polarized cellular polymer films with controlled internal micro-structures that show significant promise as high-performance piezoelectric materials. Vat photopolymerization (resin printing) is an attractive method to create engineered ferroelectrets; however, commercial resins do not have the required electrical properties. The presentation will discuss formulating resins for vat photopolymerization while balancing the competing requirements of high-resolution and suitable electrical properties. Focus will be placed on the practical aspects of controlling the resolution of a resin and the elements which impact formulation and performance. Several electrical characterization techniques will be highlighted showcasing the tools and challenges associated with understanding the electric properties of dielectric polymer films at high electric fields.

Nicholas Lanigan Biography: Nicholas received both his undergraduate degree (Nanotechnology Engineering, BASc 2013) and graduate degree (Chemistry, PhD 2019) from the University of Waterloo. During his PhD, Nicholas worked under the supervision of Prof. Xiaosong Wang investigating the bulk supramolecular polymerization of metal coordination compounds. After completing his doctorate, Nicholas undertook a brief postdoctoral position with Prof. Em. Mario Gauthier, exploring adhesives based on functionalized polysiloxanes. Subsequently, Nicholas accepted a postdoctoral position sponsored by DAVWIRE at the University of Western Ontario with Prof. Aaron Price. Nicholas worked on the development of photocurable polysiloxane resins for the fabrication of polarized polymer foams called ferroelectrets. Nicholas joined DAVWIRE's team in 2023 to continue developing ferroelectrets for the aerospace and defense industries. Nicholas is currently an R&D manager at DAVWIRE and is also responsible for business development of technical services and products.

PERIKLIS ALIKIOTIS
Chem. Eng.
Waterloo

Utilizing Lignin as a Sustainable Filler of Polyvinyl Chloride (PVC) Composites: Effects of Ash Content and Loading Levels on Thermomechanical and Combustion Properties

Utilizing lignin as a sustainable filler of polyvinyl chloride (PVC) composites :

Effects of ash content and loading levels on thermomechanical and combustion properties

Perry Alikiotis

Lignin

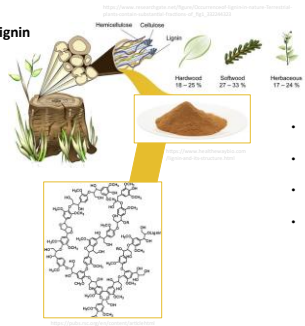

- Second most abundant biopolymer – provides toughness to wood and resistance to rotting.
- Typically regarded as waste from the pulp & paper industry, its utilities are being explored.
- Lignin can be used as a filler, compatibilizer, or reinforcer in certain materials.
- High compatibility with PVC due to hydrophobic nature.

Lignin Grades

- Low quality lignin as received (H) was laboratory purified to generate washed lignin (W). Both grades were compared alongside industrially purified lignin (L).
- Grades were loaded at 18 wt. % and additional samples were made at 9 & 26 wt. % using W lignin

	Ash Content (w/w %)	pH
Wash (W) lignin	3.49	5.2
LpH (L) lignin	0.37	4.5
HpH (H) lignin	63.50	8.9

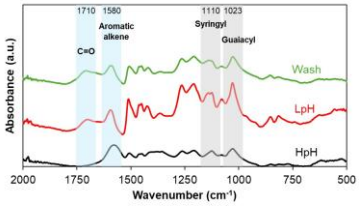

Tensile Properties

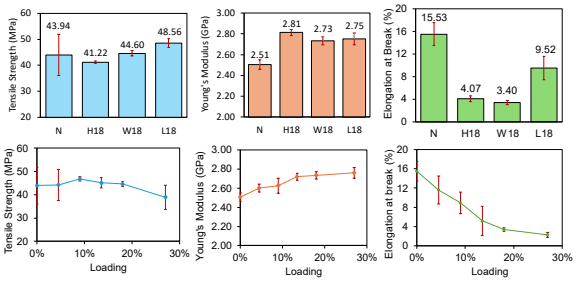

Combustion Properties

LOI: Limiting Oxygen Index

S: Comprehensive combustion index
C: Flammability index
D_i: Ignition index
D_b: Burnout index

$$S = \frac{R_{max} \times R_{ave}}{T_i^2 \times T_b}$$

$$C = \frac{R_{max}}{T_i^2}$$

$$D_i = \frac{R_{max}}{t_i \times t_{max}}$$

$$D_b = \frac{R_{max}}{\Delta t_{1/2} \times t_{max} \times t_b}$$

	LOI
N	45.8%
H18	42.1%
L18	41.0%
W18	41.4%
W9	43.0%

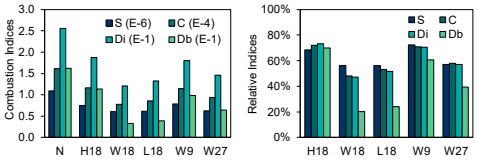

Apparent Pyrolysis Kinetics

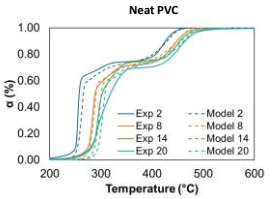

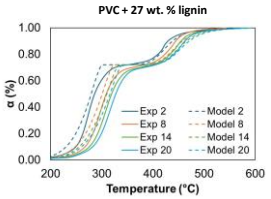

	E (kJ/mol)	A (1/min)	Contribution
D1C1 (A4)	133.17	1.07E+12	0.53
D1C2 (F2)	138.38	9.48E+11	0.20
D2 (D3)	291.65	5.66E+19	0.27

	E (kJ/mol)	A (1/min)	Contribution
D1 (D4)	161.01	1.85E+13	0.72
D2 (F3)	300.82	6.01E+21	0.28

TOBECHUKWU OHAKA
Chem. Eng.
Waterloo

Recyclable and Sustainable Natural Rubber Biocomposite Vitrimers Induced by Dynamic Anhydride-Epoxy Bonds

RECYCLABLE AND SUSTAINABLE NATURAL RUBBER BIOCOMPOSITE VITRIMERS INDUCED BY DYNAMIC ANHYDRIDE-EPOXY BONDS

Tobechukwu Ohaka,
Ph.D Candidate, Chemical Engineering

[1] Schematic of anhydride-epoxy NR vitrimer

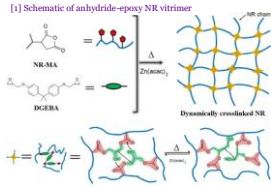

[2] Schematic of maleic anhydride modification of CNC

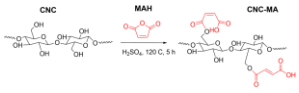

[1] **Recyclable and Self-Healing Natural Rubber Vitrimers from Anhydride–Epoxy Exchangeable Covalent Bonds** DOI: 10.1021/acsapm.3c01238
[2] **Recyclable and Sustainable Natural Rubber Biocomposite Vitrimers Induced by Dynamic Anhydride–Epoxy Bonds** DOI: 10.1021/acsapm.4c01954

Objective and Context

- Develop recyclable, high-performance rubber materials using vitrimers and cellulose nanocrystals (CNC) as a sustainable alternative to traditional vulcanized rubber.

Vitrimers use dynamic covalent crosslinks enabling rubber reprocessing

Nanofillers enhance the physical properties of rubber

Cellulose Nanocrystals (CNC)s are high molecular weight, bio-sourced nanofillers

Modifying CNCs with similar functional groups to the vitrimer chemistry can improve polymer-filler interactions

What I Did

1. Functionalize CNCs with maleic anhydride (MA) to make maleic anhydride modified CNCs (CNC-MA)
2. Torque mix natural rubber with MA, Bisphenol A diglycidyl ether (DGEBA), Zn(ACAC)2, CNCs and CNC-MA
3. Thermally cure batches at 180C/3000 psi to make crosslinked material
4. Physical characterization (Tensile testing, FTIR, DSC, DMA, etc....)
5. Cut tested material into pieces (~0.5g), thermally cure material at 180C/3000 psi, retest

Key Findings

CNC-MA dispersed better than unmodified CNC and provided higher crosslinking density, improving performance.

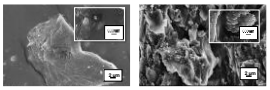

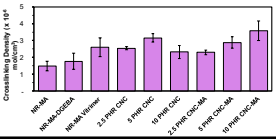

CNC and CNC-MA improved mechanical properties by 20–37.6%

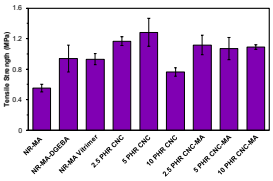

Recycling and Performance

Nanofiller amount and type impacted the thermomechanical properties during recycling

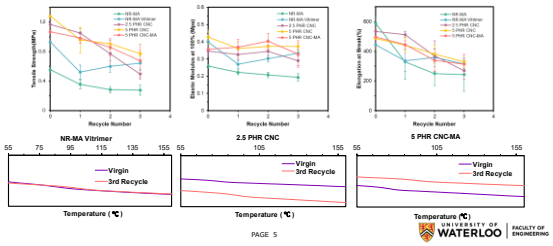

UNIVERSITY OF WATERLOO
FACULTY OF ENGINEERING

Questions?

LAUREN DILORETO
Chemistry
Waterloo

Upcycling of Polyolefins into Stress-Responsive Materials

UPCYCLING OF POLYOLEFINS INTO STRESS-RESPONSIVE MATERIALS

4/30/25

Lauren DiLoreto

Advisor: Yangju Lin
Department of Chemistry

UNIVERSITY OF WATERLOO | FACULTY OF SCIENCE

LinAB
Polymer Research for Sustainability Solutions

Project Motivation

64 million tons of polyolefin waste generated annually

Instead: upcycle existing polyolefin waste

High – Value Mechanochromic Polyolefins

Resistance to degradation resulting in their accumulation in our environment

High recycling costs vs. cheap manufacturing costs

Niaounakis, M. *The Problem of Marine Plastic Debris* In Management of Marine Plastic Debris, William Andrew Publishing, 2017; pp 1-555.

UNIVERSITY OF WATERLOO | FACULTY OF SCIENCE

Spiropyran -Based Mechanochromic Polymers

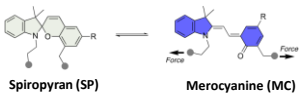

Spiropyran (SP) **Merocyanine (MC)**

- Alter optical properties in response to force
- Labile C-O bond
- Tunable *R* group influencing thermal stability and SP/MC equilibrium

Current Crosslinking of Polyolefins with Spiropyran:

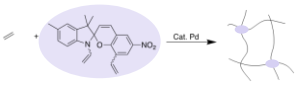

- Require additives and or catalysts
- Copolymerization prevents use of post consumer plastics

Qu, W. *Adv. Sci.* **2024**, 11, 2307568

UNIVERSITY OF WATERLOO | FACULTY OF SCIENCE

Polyolefin Crosslinkers

Covalent Crosslinker
Lab scale capability

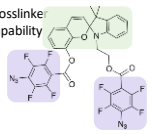

Dynamic Covalent Crosslinker
Large scale reprocessing capability

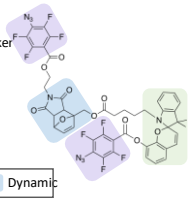

Mechanophore | Nitrene Generating | Dynamic

Nitrene Generation **C – H insertion**

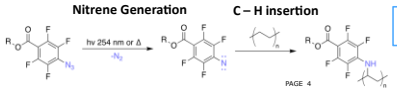

C-H insertion allows for universal crosslinking of post-consumer plastics

UNIVERSITY OF WATERLOO | FACULTY OF SCIENCE

Reprocessability Enabled by a Dynamic Crosslinker

Covalent Adaptable Network with furan-maleimide adducts:

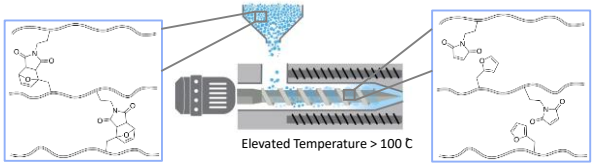

Crosslinked **Dissociated**

UNIVERSITY OF WATERLOO | FACULTY OF SCIENCE

Synthetic Route for Dynamic Crosslinker

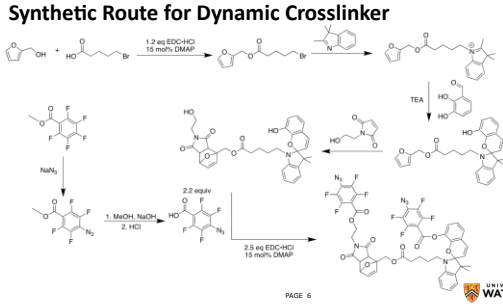

UNIVERSITY OF WATERLOO | FACULTY OF SCIENCE

SABA KARIMI
Physics
Waterloo

Two Relaxation Mechanisms for Rejuvenation of Stable Polystyrene Glass

UNIVERSITY OF WATERLOO

2025 IPR Symposium

Two relaxation mechanisms for rejuvenation of stable polystyrene glass

Saba Karimi

Karimi, S., Yin, J., & Forrest, J. A., Anomalous relaxation mechanism for rejuvenation of stable polystyrene glass, The Journal of Physical Chemistry- In review (2025)

UNIVERSITY OF WATERLOO **Background: Glass**

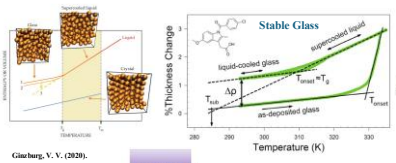

Ginzburg, V. V. (2020).

- Higher density
- Higher kinetic stability
- surface mobility

MULTI-WAVELENGTH ELLIPSOMETER

$$\rho = \frac{R_p}{R_s} = \tan(\Psi) e^{i\Delta}$$

2

UNIVERSITY OF WATERLOO **Background: Rejuvenation in Thin Films**

Rejuvenation is the transformation from glassy state to supercooled liquid (SCL) in equilibrium.
Rejuvenation in thin films occurs by **propagation of front originating from interface.**

The propagation velocity of that front has been correlated to the relaxation dynamics. $\upsilon = C\tau_\alpha^{-\gamma}$

Where τ_α is alpha relaxation time and $\gamma \sim 0.8 - 1$

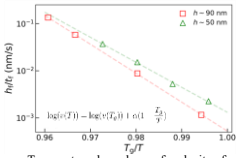

Temperature dependence of velocity of isothermal rejuvenation

Ediger, M. D. (2017). Perspective: Highly stable vapor-deposited glasses. The Journal of Chemical Physics
C. Rodríguez-Tinoco, M. González-Silveira, M. A. Ramos, and J. Rodríguez-Viejo, (2022)

Karimi, S., Yin, J.,Salez, T., & Forrest, J. A. (2024).

3

UNIVERSITY OF WATERLOO **Two-steps relaxation mechanisms**

We observed two -step behaviour in rejuvenation in polystyrene stable glasses in thickness near 140 nm.

- What simulation illustrates this two-step behaviour?
- Does this mean there are two distinct relaxation processes?
- What is the physical explanation for this behavior?

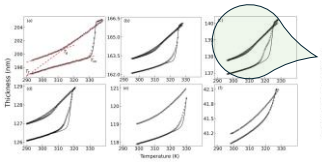

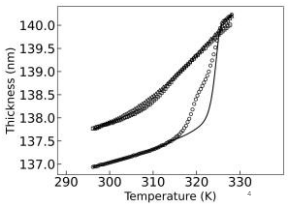

Karimi, S., Yin, J., & Forrest, J. A. (2025)

4

UNIVERSITY OF WATERLOO **Two-steps relaxation mechanisms**

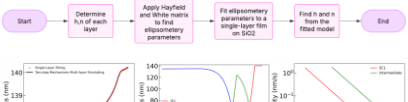

$$\log(v(T)) = \log(v(T_g)) + \alpha(1 - \frac{T_g}{T})$$

$$n_{int} = \frac{n_{SG} + n_{SCL}}{2}$$

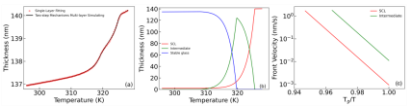

Compare physical aging and vapour deposition

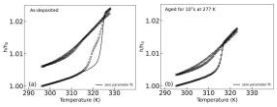

- Results showed there are two distinct relaxation processes that can couple to the material density

5

UNIVERSITY OF WATERLOO

2025 IPR Symposium

Thank You For Your Attention

Any Questions?

6

MAHNOOR MEHMOOD
Physics
Waterloo

Characterization of Polymer Stable Glasses

Title: Characterization of Polymer Stable Glasses

Abstract:

The glassy state is widespread in nature and technology, playing crucial roles in food processing, biochemical stabilization, and preservation. Examples include window glass, optical fibers, engineering plastics, metallic glasses, and amorphous silicon used in photovoltaic cells. Supercooling liquids is often necessary to achieve this state, exploiting viscosity to delay crystallization.

When a liquid is cooled below its freezing point, rapid cooling can prevent crystallization. However, as cooling continues, molecules rearrange more slowly eventually reaching a point where they cannot sufficiently explore different configurations within the given cooling rate timeframe. This transition out of equilibrium happens within a narrow temperature range where the molecular relaxation time reaches around 100 seconds, and the rate of change of volume or enthalpy with respect to temperature sharply (yet continuously) decreases to a level comparable to that of a crystalline solid. The resulting material is referred to as glass. Slower cooling rates provide more time for molecular rearrangement in a liquid, allowing it to reach lower temperatures before falling out of the equilibrium. As a result, the glass transition temperature (T_g) decreases with slower cooling rates.

By extrapolating the supercooled line, Kauzmann realized that if one could slow down liquid so slowly, one could cool it all the way down to the temperature where the entropy of the supercooled liquid is equal to the entropy of the crystal, without the occurrence of the glass transition, the temperature at which it happens is known as Kauzmann Temperature T_K (above absolute temperature), below that entropy of the supercooled liquid can be less than the entropy of the crystal, this is known as Kauzmann paradox. The glass at the T_K is known as the ideal glass which has the densest amorphous packing.

Physical aging is a common phenomenon in glasses, which is the slow evolution of molecules of a glass towards the equilibrium configuration/state. Recently a more convenient way has been introduced which is the physical vapour deposition to fabricate the glasses which has the densest packing and high kinetic stability equivalent to the glasses which has been aged for million years in a conventional way. Stable glasses are also a point of interest as they have properties near to the ideal glasses.

The non-destructive nature of AFM allows us to determine the moduli of as-deposited glass, the supercooled liquid, and ordinary glass from a single sample, providing a comprehensive understanding of the mechanical properties at different states. Furthermore, AFM enables highresolution spatial mapping of mechanical properties, allowing us to capture variations in modulus across thin films with nanoscale precision.

Our lab has recently begun investigating the elastic modulus of polystyrene (PS) films using atomic force microscopy (AFM). In this study, we examine the mechanical properties of PS films as a function of molecular weight (Mn), film thickness, and thermal stability.

To assess the influence of molecular size on the mechanical properties of PS films, we measured the elastic modulus for films of approximately 100 nm thickness with Mn values of 11,200, 60,000, and 214,000 kg/mol. Our results indicate a decrease in elastic modulus with decreasing Mn, suggesting that lower molecular weights result in softer films due to increased chain mobility and reduced entanglements. Additionally, we studied PS films with Mn = 214,000 kg/mol as a function of annealing time at $T_g + 20$ K. The AFM technique, being non-destructive, allowed us to measure the moduli of as-deposited glass, the supercooled liquid, and ordinary glass from a single sample, providing insight into the impact of annealing on mechanical relaxation and stability.

We also explored the mechanical properties of stable polymer glasses of PS prepared by physical vapor deposition (PVD). These glasses exhibit fictive temperatures as low as T_g – 20 K and kinetic stability down to deposition temperatures of ~ 0.84* T_g. Utilizing enhanced surface dynamics, PVD enables the formation of highly packed amorphous materials in a layer-by-layer fashion, leading to denser and mechanically robust films.

For PS glasses prepared at T_g – 16 K, we examined the effect of film thickness (90–200 nm) on the elastic modulus. Our findings reveal a significant increase in modulus as thickness decreases to 90 nm, which suggests that for films thinner than 140 nm, substrate effects become prominent. Furthermore, we investigated the stability-dependent mechanical properties of PS films, observing that modulus increases with increasing stability.

We have also measured the young modulus as a function of stability. The stable PS with fictive temp of T_g – 20 K, the modulus exhibited an approximately 70% increase compared to ordinary glass, indicating enhanced packing and mechanical resistance in highly stable films.

In addition, we studied the rejuvenation of stable PS glasses by heating films below T_g and monitoring the time it required to fully transform into ordinary glass. We systematically measured the modulus of stable glass, as well as 20%, 40%, 60%, 80%, and 100% rejuvenated glass. Our results indicate that the modulus of stable glasses decreases as the duration of heat treatment increases.

This study provides valuable insights into the mechanical behavior of stable polymer glasses and highlights the capabilities of AFM in probing the elastic properties of vapor-deposited polymer films with high precision.

.

ASHNA RAJEEV
Chem. Eng.
Waterloo

Nanochitin as a Strength Enhancing Agent for Paper-Based Packaging Material

Nanochitin as a strength enhancing agent for paper-based packaging material

Ashna Rajeev[1], Sarswati Koul[2], Aaron Guan[2], Boxin Zhao[1*]

[1] *Department of Chemical Engineering, 200 University Avenue West, Waterloo, Ontario, Canada, N2L 3G1*

[2] *Neptune Nanotechnologies, 37-90 Nolan Court, Markham, Ontario, Canada, L3R 4L9*

[*] zhaob@uwaterloo.ca

EXTENDED ABSTRACT

Introduction

Paper-based packaging materials offer a promising solution for a circular economy and a sustainable alternative to petroleum-based packaging. However, their poor mechanical strength, limited durability, weak barrier properties, and potential fire hazards present significant challenges. To address these issues, researchers have explored various sustainable additives for reinforcing the paper fiber matrix. These include polysaccharides (cellulose, starch, chitin, chitosan, and alginate), lignin, lipids, and proteins (such as whey protein, casein, collagen, and gelatin) [1, 2, 3, 4, 5]. These materials can either be integrated into the paper matrix or applied as a surface coating to enhance performance.

In this work, we investigate the potential of nanocrystalline chitin (NCH) as an additive for enhancing the mechanical properties of paper pulp, for developing advanced paper-based packaging solutions. Chitin, the second abundant polysaccharide after cellulose, is a key component found in crustacean shells, insect exoskeletons, and fungal cell walls. It is isolated from underutilized fishery waste in the form of nanofibrils and nanoparticles, through a multi-step process: purification, demineralization to remove calcium-based minerals, deproteinization to eliminate protein complexes, and discoloration [6]. The chemical structure of chitin closely resembles that of cellulose, consisting of N-acetyl-β-D glucosamine linked by 1,4-β-glycosidic bonds. The primary difference lies in the C2 position, where chitin features an acetamido group instead of cellulose's hydroxyl group [7]. Through comprehensive material characterization, we elucidate the complex interplay between nanochitin particles and paper fibers, revealing a dual-mechanism interaction that combines electrostatic attraction with extensive hydrogen bonding networks. By systematically varying chitin concentrations up to 5 wt% and characterizing the resulting NCH-Pulp fiber architectures, we demonstrate how these nanoscale interactions translate into significant mechanical enhancements in the composite materials.

Materials and Methods

Canadian unbleached softwood kraft pulp was obtained commercially, while nanocrystalline chitin (NCH) was synthesized by Neptune Nanotechnologies (PCT/CA2023/051058) [8]. The dry pulp was hydrated overnight, disintegrated, and filtered to form a wet pulp cake (10–15% fiber consistency). It was then stored in a refrigerator for later use. To study NCH-pulp fiber interactions, a 50:50 NCH/Pulp composite was prepared. Wet pulp was dispersed in water for 24 hours, while NCH particles were sonicated for 5 minutes. The NCH dispersion was then mixed with the pulp and stirred at 60 °C for 24 hours. For composite handsheet preparation, the pulp cake was dispersed in 500 mL of water (0.3 wt%) and stirred for 24 hours. Aqueous dispersion of NCH particle (1.5, 2.5, and 5 wt% relative to dry pulp) were added to the pulp, with neat pulp (0 wt% NCH) as a control. The mixture was stirred at 60 °C for 24 hours. Handsheets (60g/m^2) were prepared per TAPPIT-205. NCH/Pulp composite handsheets were prepared using a LABTECH sheetformer(Model 301-1) per TAPPI T 205. The NCH/Pulp suspension (0.019 wt%) underwent agitation

(5s), settling (10s), and couching (5s) with blotting sheets. The wet handsheets were pressed at 667 kPa for 10 minutes and dried using a speed dryer at 120 ◦C or 150 ◦C.

Results and Discussions

TEM imaging revealed that NCH particles have a rod-like structure with a high aspect ratio (Figure 1(a)), averaging 128 nm in length and 10 nm in width. The zeta potential at neutral pH was +28 mV, indicating positive surface charges from amine group protonation. X-ray diffraction confirmed their crystalline

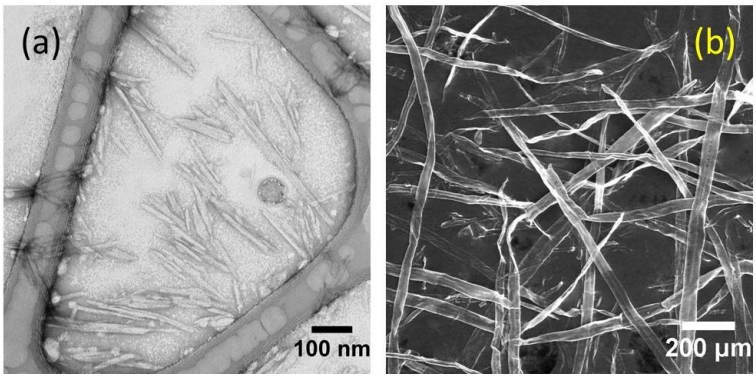

Figure 1: (a) TEM images of NCH Particles; (b) E-SEM image of disintegrated paper pulp fibers.

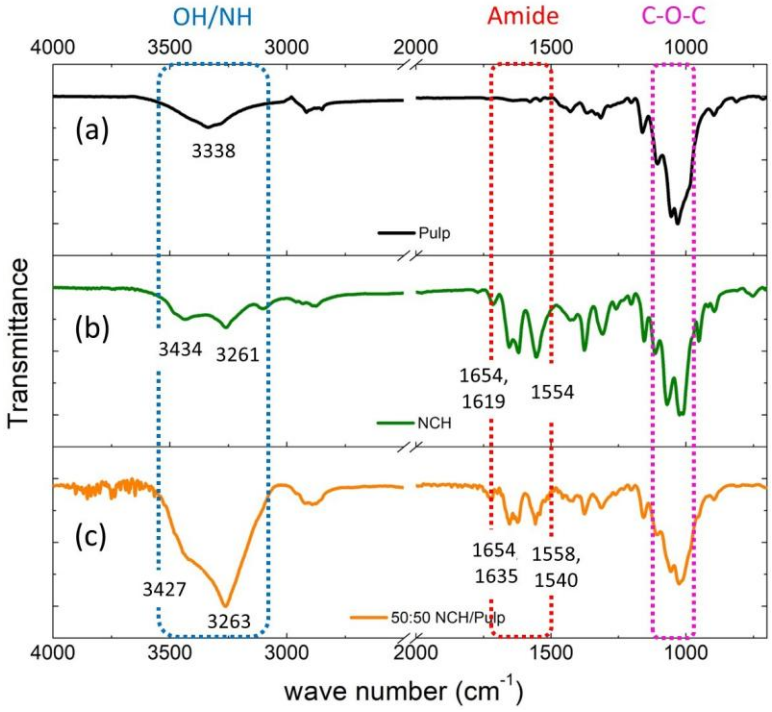

Figure 2: FT-IR spectra of (a) neat paper pulp, (b) neat NCH, and (c) 50:50 NCH/Pulp composite.

structure. Similarly, the E-SEM observation shows the entangled network of disintegrated unbleached pulp fibers, with millimeter-scale lengths and approximately 25 μm diameters (Figure 1(b)).

Chemical interactions

Figure 2(a) presents the FT-IR spectrum of the paper pulp, exhibiting characteristic absorption bands of cellulose. This spectrum reveals a prominent peak at 3338 cm^{-1} attributed to O-H stretching vibrations.

Figure 2(b) shows the FT-IR spectrum of neat NCH exhibiting the characteristics peaks of the α-chitin structure. A notable feature is the presence of two distinct bands in the amide I region at 1654 and 1619 cm^{-1}. The higher wave number peak (1654 cm^{-1}) corresponds to intermolecular hydrogen bonding between two adjacent chitin molecules through -NH and -C=O functional groups. The peak at lower wave number (1619cm^{-1}) signifies the intramolecular hydrogen bonding within a chitin backbone via -NH and -C=O [9]. The other characteristic peaks exhibited by NCH are: O-H stretching at 3430 cm^{-1}, N-H stretching at 3258 cm^{-1} and 3100 cm^{-1}, C-H symmetric and anti-symmetric stretching at 2927-2875 cm^{-1}, and amide II (N-H bending) vibrational mode at 1554 cm^{-1}.

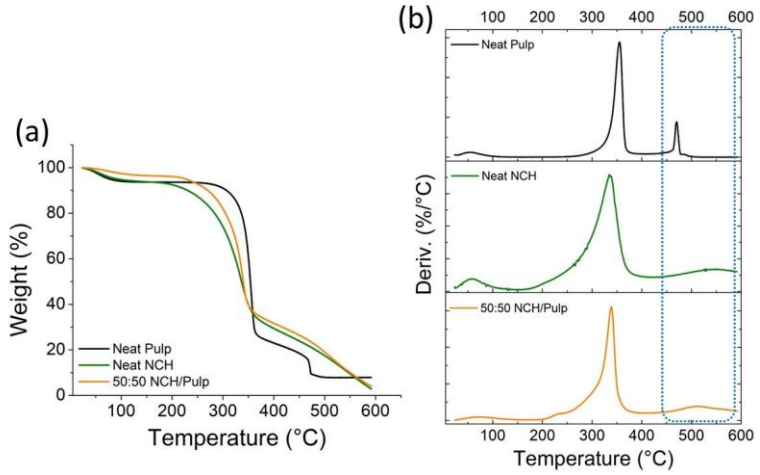

Figure 3: (a) TGA and (b) DTG curves of neat pulp, neat NCH, and 50:50 NCH/Pulp composite.

While, Figure 2 (c) shows the FT-IR spectrum of 50:50 NCH/paper composite. In the OH/NH stretching region (around 3500–3000 cm^{-1}), highlighted in blue rectangle, the NCH/Pulp composite showed significant shifts from paper's original OH position by 75 cm^{-1}. The OH peak of NCH/Pulp composite converged toward chitin's NH peak position, suggesting specific interactions between paper's OH groups and chitin's NH groups. The NCH/Pulp composite shows a distinct shoulder around 3427 cm^{-1}, indicating the partial retention of NCH's original OH environment. The amide band, which was absent in the neat paper's spectrum appeared in the NCH/paper composite (marked within red rectangles in Figure 2). With respect to the neat NCH's amide I peak at higher wavenumber, the NCH/Pulp composite did not show a significant shift. Whereas, the amide I peak at lower wavenumber showed a significant shift of 16 cm^{-1} by the NCH/Pulp composite, while maintaining its characteristic shape. This signifies the changes in the intramolecular H-bonding via the -NH and C=O, as mentioned above, could be on the surface of the chitin particles. Furthermore, the amide II band exhibited peak splitting in the NCH/pulp composite, contrasting with the single peak in neat NCH, indicating modified hydrogen bonding environments due to the existence of different modes of N-H bending from the partial retention of original OH environment, in consistent with the trendin the OH region. However, the C-O-C region (around 1000 cm^{-1}, highlighted in pink rectangle) exhibited minimal peak shifts in the composites compared to neat paper. This evidence

indicates that interactions occur primarily through peripheral hydroxyl functionalities of cellulose and NH and C=O moieties of NCH particles, without significant alterations to the polymer backbone.

Thermal degradation characteristics

TGA and derivative thermogravimetric (DTG) curves of neat paper pulp, neat NCH particles, and 50:50 NCH/pulp composites are presented in Figure 3. For the 50:50 NCH/Pulp composite, the second and most significant decomposition step or the active pyrolytic stage appeared at 338 °C. The positioning of the second peak of the NCH/pulp composites between those of neat pulp and neat NCH indicates interactions such as hydrogen bonding and electrostatic attractions. Furthermore, the third degradation step of the NCH/Pulp composite occurred at 510 °C exhibiting a broad and less intense peak at higher temperatures, similar to neat chitin samples, contrasting with the sharp, intense peak of neat paper pulp. This indicates that the alteration in char structure due to NCH incorporation, facilitated by the hydrogen bonding network between NCH and paper fibers (as evidenced by FTIR), results in the formation of a more thermally stable char residue. The modification of this high-temperature oxidation peak, influenced by these strong interfacial interactions, suggests potential improvement in flame retardancy properties of the composites, though further studies would be needed to confirm this effect.

Mechanism of interaction between chitin and paper fibers

Compiling the observations based on FT-IR analysis and thermal degradation data presented, we propose a dual-mechanism interaction between NCH particles and paper fibers, as illustrated schematically

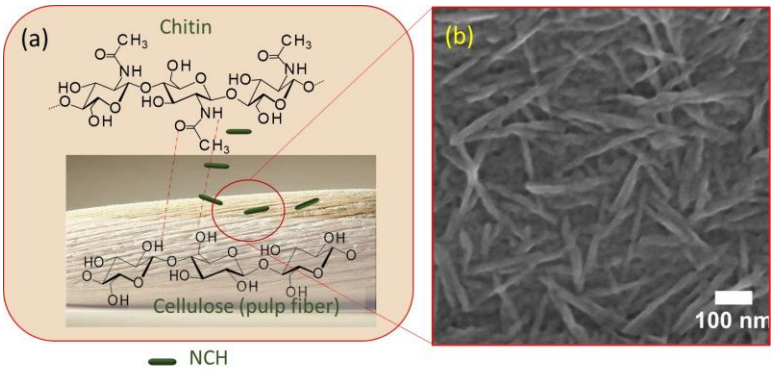

Figure 4: (a) Schematic showing the interaction mechanism between paper fibers and nanochitin particles. (b) SEM image of NCH particles adhered to the surface of a paper fiber. The scale bar represents 100 nm.

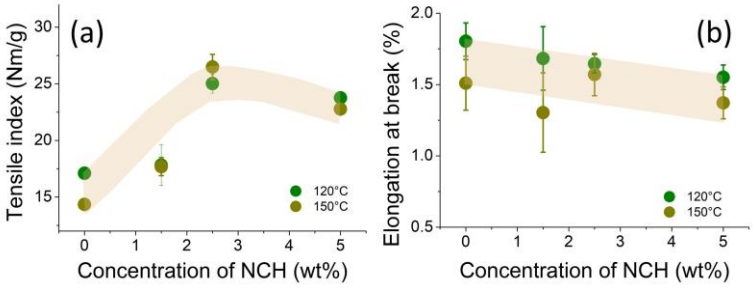

Figure 5: (a) Tensile index and (b) % elongation at break of NCH/Pulp handsheets prepared at 120 °C and at 150 °C as a function of NCH loading. Shaded regions are included as visual guides to emphasize the trend.

in Figure 4 (a). Through systematic morphological, thermal, and spectroscopic characterization, we established a comprehensive interaction mechanism wherein initial electrostatic attractions between oppositely charged components facilitate the formation of dynamic, twinkling hydrogen bonds between chitin nanoparticles and paper fibers in the aqueous environment, subsequently evolving into stable hydrogen bonding networks.

Tensile properties of nanochitin/paper composite handsheets

Building upon the observed interaction between NCH particles and paper fibers, we proceeded to examine how these interactions influence the mechanical performance of the NCH/pulp composites through comprehensive tensile property testing. Figure 5 (a) illustrates the substantial enhancements in tensile index achieved through the incorporation of NCH particles. The trend, shown by the shaded region in the graph, clearly indicates that the tensile indices increased up to a concentration of 2.5 wt% and then slightly decreased at 5 wt%. At a 2.5 wt% concentration, the NCH/Pulp composite yielded tensile index augmentations of 46% and 85% at 120 ◦C and 150 ◦C, respectively. Notably, concentrations exceeding 2.5 wt% led to either a marginal decline or plateau in tensile index values, probably due to the saturation effect. Conversely, Figure 5 (b) showed a consistent but gradual decrease in elongation properties of the NCH/Pulp composites, with increase in the nanochitin particles, over the temperature range. At 2.5 wt%, the elongation at break of the composite decreased by 8.7% at 120 ◦C and 4% at 150 ◦C. While tensile index values are primarily reported for paper-based materials, a representative stress-strain curve for the samples is provided in Figure S3 of the ESI to facilitate comparison with conventional polymeric materials. The observed increase in tensile strength of the NCH/Pulp composites can be attributed to the interaction between NCH particles and pulp fibers, enhancing the overall network strength. These nanoparticles improve stress transfer between fibers, allowing for better distribution of applied forces.

REFERENCES

[1] P. Samyn, A. Barhoum, T. Öhlund, A. Dufresne, Nanoparticles and nanostructured materials in papermaking, Journal of Materials Science 53 (2018) 146–184.

[2] N. M. Julkapli, S. Bagheri, Developments in nano-additives for paper industry, Journal of wood science 62 (2016) 117–130.

[3] S. Kopacic, A. Walzl, A. Zankel, E. Leitner, W. Bauer, Alginate and chitosan as a functional barrier for paper-based packaging materials, Coatings 8 (7) (2018) 235.

[4] X. Wu, M. Babi, J. Moran-Mirabal, R. H. Pelton, Grafting polyanhydride polymers to cellulose nanofibers, Cellulose (2024) 1–18.

[5] Z. Song, G. Li, F. Guan, W. Liu, Application of chitin/chitosan and their derivatives in the papermaking industry, Polymers 10 (4) (2018) 389.

[6] L. Bai, L. Liu, M. Esquivel, B. L. Tardy, S. Huan, X. Niu, S. Liu, G. Yang, Y. Fan, O. J. Rojas, Nanochitin: chemistry, structure, assembly, and applications, Chemical reviews 122 (13) (2022) 11604–11674.

[7] M. R. Gal, M. Rahmaninia, M. A. Hubbe, A comprehensive review of chitosan applications in paper science and technologies, Carbohydrate Polymers 309 (2023) 120665.

[8] Q. Guan, Solvent systems and methods for processing chitin (Feb. 2024).

[9] G. Cárdenas, G. Cabrera, E. Taboada, S. P. Miranda, Chitin characterization by sem, ftir, xrd, and 13c cross polarization/mass angle spinning nmr, Journal of Applied Polymer Science 93 (4) (2004) 1876–1885.

MATTHEW SCARFO
Chem. Eng.
Waterloo

Microscale Photolithography of LCE Soft Actuators and Robots with Magnetically Driven, Discretized Alignment Domains

Microscale Photolithography of LCE Soft Actuators and Robots with Magnetically Driven, Discretized Alignment Domains

Matthew Scarfo [a,b], Ramón Santiago Herrera Restrepo [a,c], Hamed Shahsavan [a,b,d]*

[a] Department of Chemical Engineering, University of Waterloo, ON, N2L 3G1, Canada
[b] Institute for Polymer Research, University of Waterloo, ON, N2L 3G1, Canada
[c] Departament de Ciència de Materials i Química Física, Universitat de Barcelona, 08028 Barcelona, Spain
[d] Centre for Bioengineering and Biotechnology, University of Waterloo, ON, N2L 3G1, Canada
*Corresponding author: hshahsav@uwaterloo.ca

Extended Abstract:

In the domain of Liquid Crystal Elastomers (LCEs), the effective downscaling of LCEs is essential to unlocking their practical applications as soft robots and actuators in biomedical and MEMS devices. Of equal importance, the alignment-fabrication strategies must be versatile, high throughput, and cost-effective. In recent literature, state-of-the-art photo-printing equipment such as DLW, DMD, and DLP coupled with patterned surfaces or external fields exemplify promising alignment fabrication strategies to achieve downscaling [1-4]. However, they are tremendously expensive and inaccessible to many. Henceforth, the inexpensive prototype developed in the present work showcases an alignment-fabrication strategy that utilizes photolithography and magnetic fields to obtain microscale LCE actuators and soft robots with high throughput. By combining stepwise photopolymerization through a photomask with a variable external field, the careful choice of mask design and director discretization demonstrates versatile programmability. Herein, this straightforward approach is used to produce a variety of LCE constructs with discretized alignment domains from the millimetre to micrometre scale, exhibiting fast photothermal and photochemical actuatable shape-change.

Liquid Crystal Elastomers (LCEs) are a class of shape changing polymers composed of crosslinked liquid crystal (LC) units called mesogens, typically of the thermotropic class. LCEs are characterized by their anisotropic, reversible, and untethered stimuli-responsive deformations that are intrinsically related to the ordering of mesogens in the polymer network. Stimuli such as heat or light induce disorder to the network, and consequently shape reconfiguration, which is reversed upon removal of the stimulus owing to the self-ordering nature of LCs coupled with elasticity of a polymer network. These soft bodied materials have demonstrated elongations of actuation up to 400% [5] and the ability to move objects hundreds of times their weight [6], with actuation speeds on the order of milliseconds to seconds. Numerous LCEs developed in the literature exhibit actuations that can lead to locomotion or performing useful functions such as cargo transport. The miniaturization of these constructs is expected to unlock the future of LCEs in applications such as minimally invasive biomedical soft robots, or flexible and tunable actuators in microelectromechanical systems (MEMS).

An elastic network of LCs manifests its shape change based on not only its programmed alignment and geometry, but also in the mechanism of stimulation. In the simplest example, a thin film of LCE with uniform alignment of mesogens along the length, referred to as the

nematic director field ($\hat{n}$), would demonstrate a contraction along this director when heated above its nematic-isotropic transition temperature (T_{NI}). The disorientation of mesogens in plane induces stresses along the director leading to bulk anisotropic shape-contraction. This is a mechanism inherent to thermotropic LCs induced directly or indirectly by photothermal heating of fillers. For the same 2D construct, the additional crosslinking of azobenzene moieties can enable out-of-plane bending via cis-trans isomerization induced by light, referred to as a photochemical mechanism. The reconfiguration of these molecules from linear to bent-like induces stresses normal to the plane, and thus shape-bending. 3D deformation modes such as twisting, bending, buckling, and shearing could also be realized in the thermotropic mechanism by controlling the initial shape of the LCE and alignment in up to three dimensions via alignment engineering. Typical variations of alignments are continuous (e.g. splay, twist), but could also be made discontinuous by creating discretized regions of alignment throughout the sample space.

Discretized alignment architectures demonstrate versatility in the programming of unique, three-dimensional deformations, as the boundaries of the discretized regions can be precisely tuned throughout the sample space (limited only by the choice of alignment-fabrication method). The discontinuity, or mismatch, between alignment regions create elastic instabilities upon actuation, realizing localized deformation modes such as buckling or bending. Therefore, the sum of these regions introduces high degrees of freedom in the overall shape-change programming of LCEs ranging from microscopic to macroscopic scale. A popular alignment-fabrication strategy for achieving discretized alignments, which is pertinent to the current work, involves the stepwise photopolymerization of regions of LC that are exposed to external magnetic fields. Thermotropic LCs which are rod-like will rotate to orient with the direction of the applied field to minimize magnetic energy density, owing to anisotropy of their magnetic susceptibility. By inducing uniform alignment, but polymerizing discrete regions at a time, the field direction can be varied between each fabrication step to obtain neighbouring regions with distinct alignments.

Magnetic fields offer unique advantages over traditional alignment techniques. Mechanical stretching or shear alignment is confined to uniform alignments coupled to sample architecture. Command coatings or patterned surfaces, while capable of discretization, are limited to thin-film geometries and require expensive chemicals or equipment and can be time consuming to prepare. On the other hand, a strong enough magnetic field is capable of aligning mesogens on demand, on different length scales, decoupled from the system geometry. Therefore, even without discretization, a high degree of freedom in shape-programming can be obtained from uniform magnetic field alignment alone [7].

Two-dimensional microscale LCE freeforms with discretized alignments in two-dimensions are developed in this work, utilizing a straightforward lithography method. The prototype device is capable of fabricating LCE actuators and soft robots on different length scales, with feature sizes (and discretized alignment regions) as small as 50 µm. This approach involves stepwise photopolymerization with collimated light through a photomask with rotational symmetry, wherein the rotation of the photomask is coupled to the rotation of a Halbach array, which generates the magnetic field to align LCs. Therefore, the alignment of LCs

varies in two dimensions, with each feature having a director field that differs from a neighbouring feature, i.e., discretized, by a specific angle dictated by the rotation of the magnetic field. By adjusting the angle between the photomask features and the magnetic field, one may access theoretically infinite rotational degrees of freedom in the director fields. Subsequently, using a double-photomask approach, kirigami-inspired actuators could be fabricated by first printing hinges with desired alignment, followed by printing of passive isotropic features.

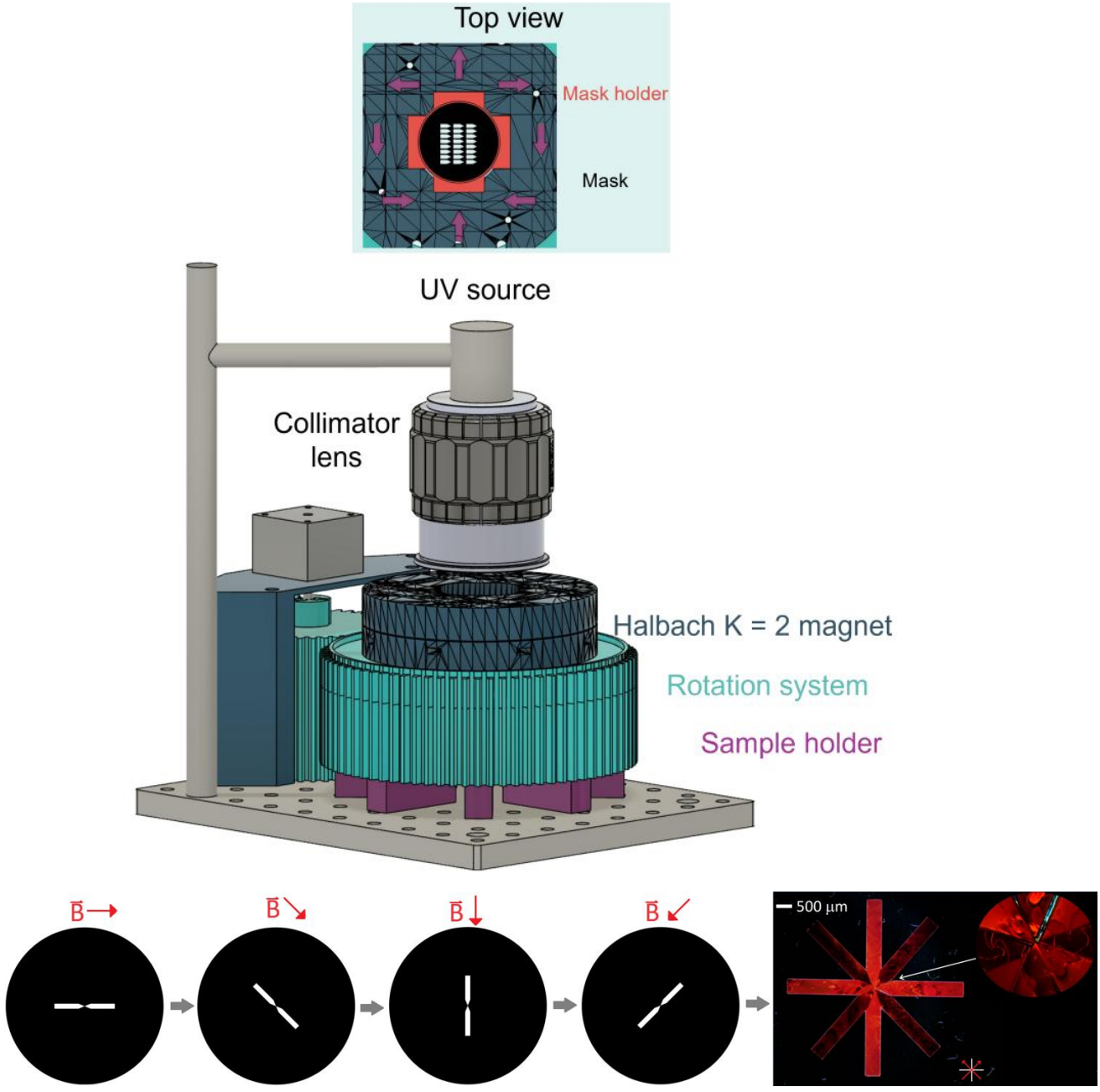

Figure 1: Prototype Overview and Printing Scheme ($\vec{B}$ is the applied magnetic field direction)

Two light-responsive formulations, a photothermal LCE [8] and photochemical LCN [9], were used in this development. The effects of different photo-printing parameters were characterized and optimized using the Taguchi method, based on preliminary information from photo-rheological examination. Furthermore, the discretized domains of alignment are characterized visually by polarized optical microscopy (POM) and quantitatively by UV-Vis dichroism tests. To ultimately demonstrate the prototype's application, the two formulations are used to print grippers, checkerboards, fans, cubes, and snakes with light-driven actuation.

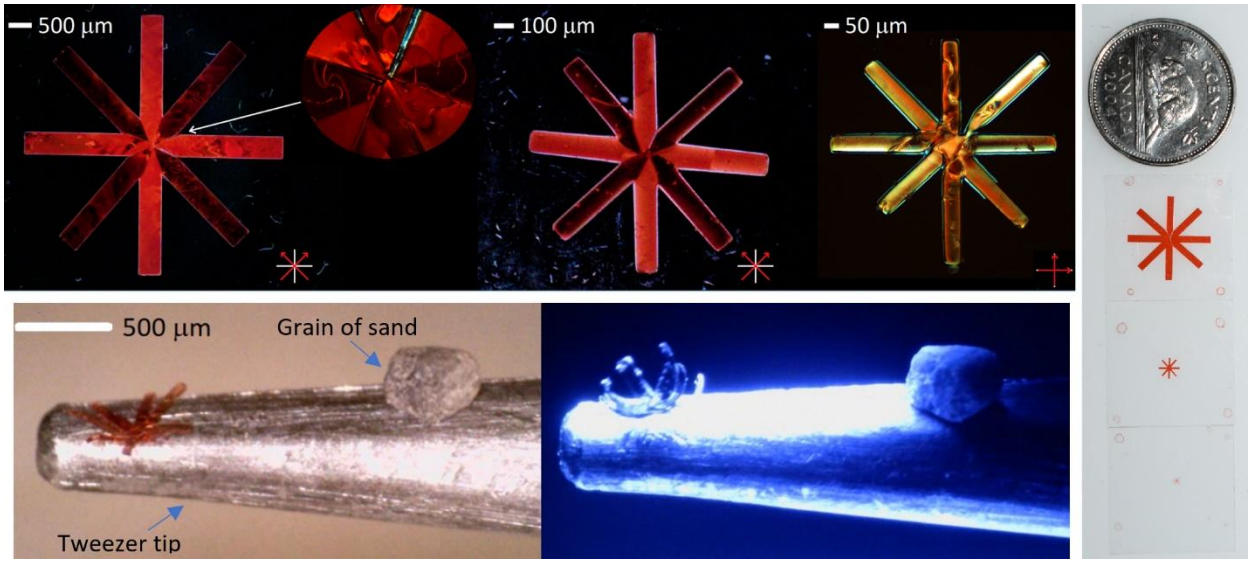

Figure 2: Scaling Down of LCE Grippers and their Light-Driven Actuation

References:

[1] *ACS Appl. Mater. Interfaces* 2019, 11, 31, 28236–28245

[2] *Adv. Mater.* 2024, 36, 2414209.

[3] *Adv. Funct. Mater.* 2025, 35, 2413513.

[4] *Adv. Mater.* 2020, 32, 2002753.

[5] *Adv. Funct. Mater.* 2006, 16, 556.

[6] *C. R. Chim.* 2009, 12, 85.

[7] *Proc. Natl. Acad. Sci. U.S.A.* 2018, 115 (51) 12950-12955

[8] *Soft Matter* 2022, 18, 8063-8070.

[9] *Adv. Funct. Mater.* 2024, 2413129.

LU YIN
Chem. Eng.
Waterloo

Polypyrrole/Rubber Composite Latex as High-Performance Sustainable Conductive Coating

Polypyrrole/Rubber Composite Latex as High-Performance Sustainable Conductive Coating

Lu Yin, Ali Vahidifar, Aleksander Cholewinski, Jenna Liu, Steven Yu, and Boxin Zhao

Abstract

Conductive inks have been exploited to print flexible and conductive pathways on the surface of insulators, offering promising applications in chemical engineering, electronics, and sensors. However, their development and large-scale production are hindered by complex preparation processes, high-cost conductive fillers, and use of toxic solvents. In this study, we present a greener one-pot synthesis of water-based conductive composite latex by using polypyrrole (PPy) as the conductive filler and carboxylated styrene butadiene rubber (XSBR) as the flexible binder, aimed at sustainable manufacturing. The resulting XSBR/PPy latex, requiring no post-treatment, demonstrates good storage stability and can be easily applied onto various flat and curved substrates including plastic, glass, rubber, and balloon, exhibiting a conductivity of approximately 2×10^{-3} S/cm and an excellent surface adhesion. Its low cost, ease of synthesis, and scalability make it a good candidate as a conductive ink and antistatic material in the field of polymer applications.

Background

Flexible and conductive coatings interact on the surface of the materials and improve the surface conductivity of the bulk insulator. Thanks to this, surface coatings can significantly decrease the materials' expense and maintain their integrity. To satisfy industrial demands, conductive inks, mainly metal-based (silver and copper) and carbon-based (graphene and CNT), are widely reported and applied in combination with advanced printing techniques. Generally, conductive inks are composed of conductive filler, polymer binder, solvent, and additive. The appropriate selection of materials is crucial to formulate the conductive inks in order to meet the requirements of sustainable manufacturing and competitive cost. In most cases, hazardous binders and toxic solvents are used, leading to the emission of harmful volatile organic compounds (VOCs) that are harmful for human being and environment. To overcome this issue, eco-friendly water-based conductive inks have been developed to significantly reduce VOCs emission. Compared with

organic solvents, water is more environmentally friendly, non-toxic, readily available, and cost-effective, making it an ideal choice for sustainable applications in various chemical processes. However, it is challenging and tedious to achieve stable and uniform waterborne conductive inks for metal- and carbon-based conductive fillers because of their hydrophobicity. In addition, this raises the cost of already-expensive conductive fillers, and it is unrealistic for a large scale of production. As an alternative, intrinsically conductive polymers, such as polyaniline and polypyrrole (PPy), are good candidates as conductive fillers. PPy is especially appealing due to its high stability, ease of synthesis, and low cost. Even though several examples of conductive coatings containing conductive polymers have been reported, it is still tricky to fabricate adhesive and stable waterborne latex in a large scale-up at a low cost.

In this work, we reported the in-situ synthesis of environmentally friendly waterborne carboxylated styrene butadiene rubber (XSBR)/PPy conductive composite latex, which can serve as a flexible conductive ink. XSBR was selected as the flexible and adhesive rubber binder due to its good adhesion and stretchability. Pyrrole (Py) was polymerized in situ in the latex, acting as conductive fillers in the rubber matrix. Anionic surfactant was utilized to better disperse the positively charged PPy and to simultaneously decrease the surface tension of water to improve the wettability of composite latex on different substrates. The waterborne conductive latex shows excellent stability and can be easily drop-casted, dip-coated, or sprayed onto different surfaces, and scaled up at a low expense. The formed coatings show good adhesion and flexibility on various substrates including rubber, glass, and plastic. Meanwhile, the coatings sprayed on flat and/or curved substrates, such as balloon, plastic, glass, and natural rubber sheet, exhibit antistatic properties, making it potential candidate as an antistatic material.

Results

The in-situ polymerization of Py was conducted in the XSBR latex in the presence of APS. XSBR was selected as the host matrix, which is expected to show good compatibility with doped filler and good adhesion with different substrates. SDS aqueous solution was utilized to help to disperse the oily Py monomers and form a homogenous solution. Then, XSBR latex was poured into SDS/Py solution under vigorous mechanical stirring at 5 ^{o}C, followed by adding APS for the oxidative polymerization. The resultant composite latex can be drop-casted, dip-written, and sprayed onto a substrate to form the conductive pathway and coating. The composite latex remains stable in air over one month.

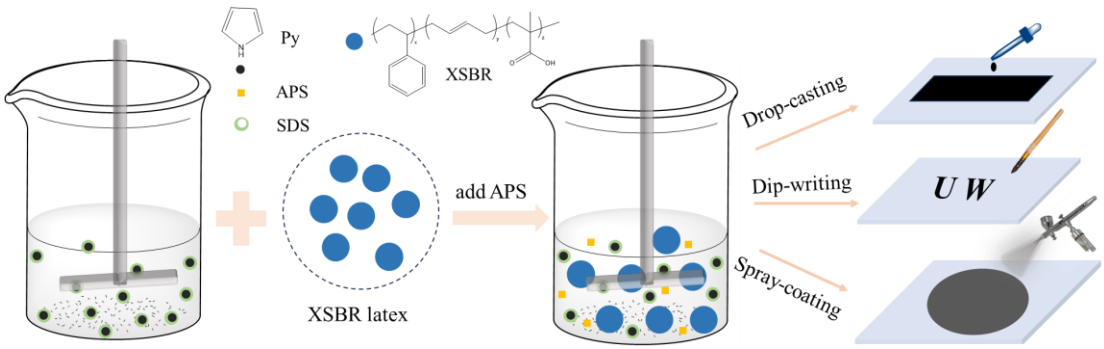

Figure 1. Schematic illustration of in-situ synthesis of composite latex, chemical structures of XSBR and Py, and application methods.

A plot of electrical conductivity for different loading fractions of Py in Figure 2a shows that the surface conductivity of the composite coatings increases with increasing Py ratio up to maximum of ~2.0 $\times 10^{-3}$ S/cm when the weight mass of Py is 15%. When the Py ratio is 5%, the high resistance of coating is more than the limit of device (20 MΩ), which is regarded as non-conductive composite. The current-voltage characterization in Figure 2b shows the same trend, in which a larger current value was detected in the samples with a higher Py ratio at the same applied potential. Importantly, the nonlinear increase of currents in three samples demonstrates their semiconductor nature, which is mainly dominated by electron tunneling and hopping conduction pathways.

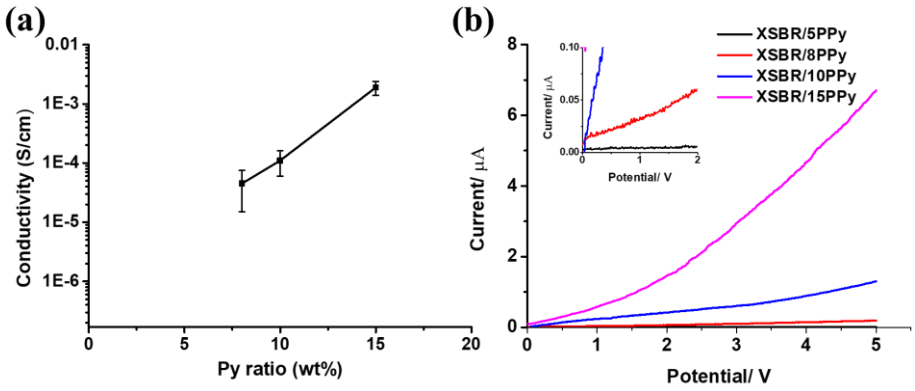

Figure 2. (a) Py weight ratio versus electrical conductivity of coatings on glass substrates with the thickness of ~80 μm; (b) Current-Voltage (I-V) characteristic curves of the composite films with different content of PPy.

The images in Figure 3 (a-c) show that the three samples have distinct current responses at the pA scale. XSBR/15PPy film has largest conductance current of ~64 pA under an applied 2 V bias due to its highest PPy content, while XSBR/8PPy and XSBR/10PPy have values of ~16 pA and ~20 pA, respectively.

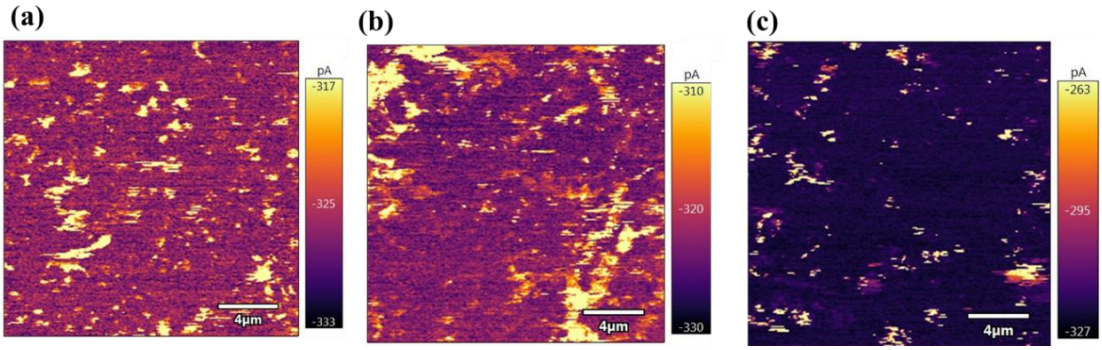

Figure 3. C-AFM micrographs of surfaces of conductive composite films in (a) (XSBR/8PPy), (b) (XSBR/10PPy), and (c) (XSBR/15PPy)). The bright irregular domains represent the conductive fillers that were distributed in the non-conductive XBSR matrix.

The composite latex can form uniform coating patterns on flat, curved, or rough surfaces, depending on the application methods. As shown in Figure 4, conductive pathways can be created by drop-casting on soft polyethylene terephthalate (PET) and polyurethane (PU) substrates, demonstrating excellent flexibility and adhesion of coatings even after many cycles of bending. Interestingly, the antistatic character of the dried coating was compared between uncoated (i) and coated (ii) substrates by approaching polystyrene microsphere.

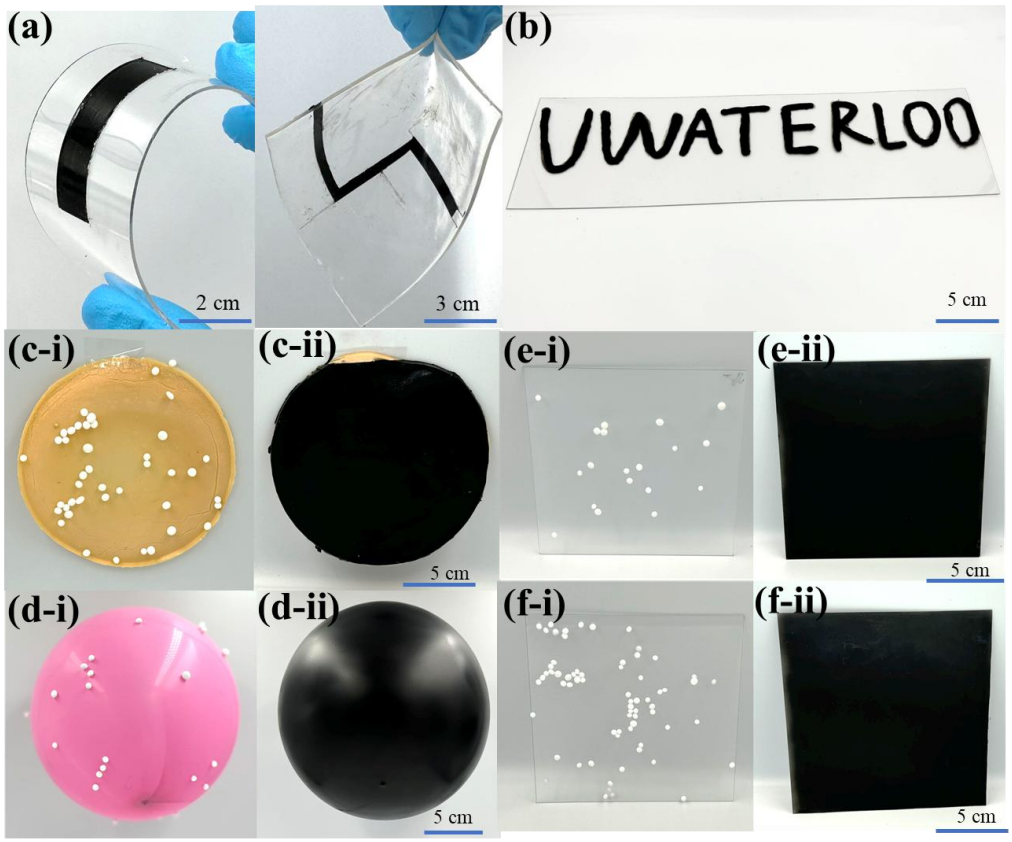

Figure 4. (a) Drop-casted patterns on the PET and PU substrates which can easily bent by nearly 90°; (b) Dip-writing pattern on PET; (c-f) uncoated (i) and spray-coated (ii) natural rubber (c), balloon (d), glass (e) and PET (f) showing antistatic properties treated by mechanical rubbing

PROF. MEGAN ROBERTS
Academic Presenter
Western

Nanocellulose for Precision Applications: Combatting Challenges Using Intentional Surface Chemistry Design

Nanocellulose for Precision Applications: Combatting Challenges Using Intentional Surface Chemistry Design

Cellulosic materials, and in particular cellulose nanocrystals (CNCs), show significant promise in many applications where synthetic polymer components are traditionally used. To improve their compatibility, stability, and dispersibility however, surface-modification is often required. During this presentation, the design and careful modification of CNC surface chemistry will be discussed within the context of two projects where (1) CNCs were used to answer questions about polymer surface interactions with cancer cells and (2) a novel method of surface functionalization was used to disaggregate uncharged CNCs. To round out this talk, a third project concerning the optimization of CNC-stabilized oat oil emulsions will be briefly discussed in order to exhibit how the potential of such materials in industrially relevant applications increases once their chemical interactions at different interfaces become well understood.

Megan defended a Polymer Chemistry PhD at University of Toronto in 2021 before moving to New Brunswick to teach organic chemistry at Mount Allison University for a year. At the end of this sabbatical replacement, she crossed Canada and took up a postdoc position at the University of British Columbia-associated Bioproducts Institute. In January 2025, Megan began her independent career as an Assistant Professor at Western University where she is working to understand how the structure of biomolecules links to their assembly. She intends to establish tools that will allow her to predict biomolecular behaviour and from this, build new classes of biomaterials for healthcare that can fully integrate with living systems.

A more detailed biography can be found on Megan's website at www.therobertslab.ca/about-megan

FRANKLIN FRASCA
Chemistry
Waterloo

Probing the Encounter Dynamics between the Side Chains of Small Multifunctional Macromolecules by Pyrene Excimer Formation

Probing the Encounter Dynamics between the Side Chains of Small Multifunctional Macromolecules by Pyrene Excimer Formation

Franklin Frasca and Jean Duhamel

INTRODUCTION

The ability of pyrene to fluoresce differently whether it exists either as a lone monomer or an excited dimer, also known as an excimer, formed upon the encounter between a ground-state and an excited pyrene, provides a powerful tool for obtaining information about the dynamics and conformation of macromolecules of any size in solution. Pyrene excimer formation (PEF) allows for the characterization of many complex pyrene-labeled macromolecules (PyLMs) in solution which would be difficult to characterize by any other common techniques based on scattering, viscosity, or NMR experiments. Due to the high molar extinction coefficient and fluorescence quantum yield of pyrene, PEF also enables the study of PyLMs under extremely dilute conditions (~ 1 – 10 mg/L) which provides an unperturbed view of the PyLM of interest at concentrations that are orders of magnitude lower than other characterization methods.

In earlier works, PEF was used to determine the rate of end-to-end cyclization (k_{cy}) of monodisperse linear chains with a pyrene appended to each end by using time-resolved (TRF) and steady-state (SSF) fluorescence.[1-3] These studies took advantage of a theoretical study by Wilemski and Fixman,[4,5] that demonstrated that the slowest internal relaxation time of a polymer described the rate constant k_{cy} of end-to-end cyclization, which was proportional to the rate constant for PEF determined through the analysis of the fluorescence decays of a pyrene end-labeled polymer. Furthermore, the limitation of having only two pyrenes per molecule restricted the determination of k_{cy} to chains that were sufficiently short to enable PEF between the two terminal pyrenyl labels. Following this preliminary work, the Model Free Analysis (MFA), which makes no assumptions about the nature of PEF to determine the average rate constant of PEF ($\langle k \rangle$), was developed to describe the internal dynamics and conformation of any pyrene-labeled macromolecule, including the short linear oligomers studied previously.

Because PEF is a bimolecular process, the rate of PEF depends on the local pyrene concentration ($[Py]_{loc}$) of a pyrene-labeled molecule in solution given by Equation 1. In Equation 1, n_{Py} is the number of ground-state pyrenes after excitation of one pyrene monomer and L_{Py} represents the square root of the average squared end-to-end distance between every pair of pyrenyl labels attached to the PyLM, whose volume (V_{PyLM}) is proportional to $(L_{Py}/l)^3$, where l represents a bond length. The general scheme of PEF and the associated SSF spectrum of a PyLM are shown in Figure 1.

$$[Py]_{loc} = \frac{n_{Py}}{V_{PyLM}} \propto \frac{n_{Py}}{(L_{Py}/l)^3} \tag{1}$$

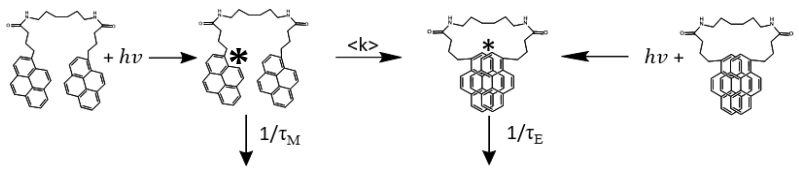

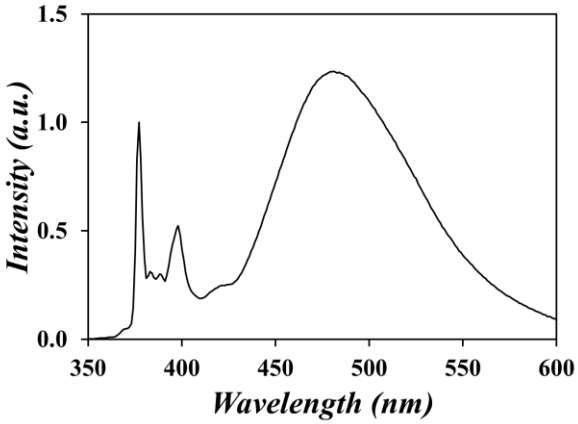

Figure 1. Top: General kinetic scheme for PEF. Bottom: Steady-state fluorescence spectrum of hexamethylene *bis*(1-pyrenebutyramide) (Py_2-HexAm), normalized to the monomer peak at 377 nm; λ_{ex} = 344 nm, [Py] = 2.5×10^{-6} M in THF.

Integration of the SSF excimer and monomer emissions between 500 – 530 and 372 – 378 nm yields the monomer (I_M) and excimer (I_E) intensities, respectively, which are used to determine the I_E/I_M ratio as a gauge of PEF efficiency for the PyLM in solution. While useful for many studies, the SSF spectra are affected by several artifacts due to solvent effects, aggregation of the pyrenyl labels (right pathway for PEF in the reaction scheme shown in Figure 1), and/or the presence of residual unreacted pyrene derivative used in the preparation of the PyLM which can distort the spectra and greatly complicate the use of the I_E/I_M ratio. On the other hand, MFA of the monomer and excimer decays obtained through TRF measurements can yield both the molar fractions of different pyrene species contributing to PEF and $<k>$, the average rate constant for PEF by diffusion (left pathway for PEF in the reaction scheme in Figure 1). The number average lifetime ($<\tau>$) is obtained through the MFA and is used to determine $<k>$ as seen in Equation 2. Both $<k>$ and the I_E/I_M ratio have been shown in previous work to be proportional to $[Py]_{loc}$ based on Equation 3.**Error! Bookmark not defined.**-7 k_{diff} in Equation 3 is the bimolecular rate constant for PEF by diffusion, and provides a measure of the dynamics of the PyLM in solution. Since $[Py]_{loc}$ is related to the conformation of the macromolecule through L_{Py}, so is $<k>$ according to Equation 3.

$$<k>=\frac{1}{<\tau>}-\frac{1}{\tau_M} \tag{2}$$

$$\frac{I_E}{I_M}\propto k_{diff}\times[Py]_{loc}=<k> \tag{3}$$

The linear relationship between $<k>$, the I_E/I_M ratio, and $[Py]_{loc}$ has thus far only been demonstrated quantitatively for series' of pyrene end-labeled dendrimers and polymeric bottle brushes and randomly labeled linear chains.**Error! Bookmark not defined.**,8,9 This work serves to extend t he validity of this relationship established for PyLMs to pyrene-labeled small multifunctional molecules.

EXPERIMENTAL

A series of diamines, polyamines, diols, and polyols were labeled with pyrene to yield both pyrene end-labeled linear diols (Py-DOs) and diamines (Py-DAs), and branched pyrene-labeled polyols

(Py-POs) and polyamines (Py-PAs) having more than 2 pyrenes, whose structures are shown in Figures 2 and 3 respectively and are collectively referred to as the PySMs. Dilute solutions of each PySM with [Py] = 2.5×10^{-6} M were prepared in THF, dioxane, DMF, and DMSO, a set of common organic solvents which solubilize a wide range of both synthetic and bio-based macromolecules. Their SSF spectra were acquired to yield their I_E/I_M ratios, and MFA of the monomer and excimer TRF decays yielded their <*k*> values.

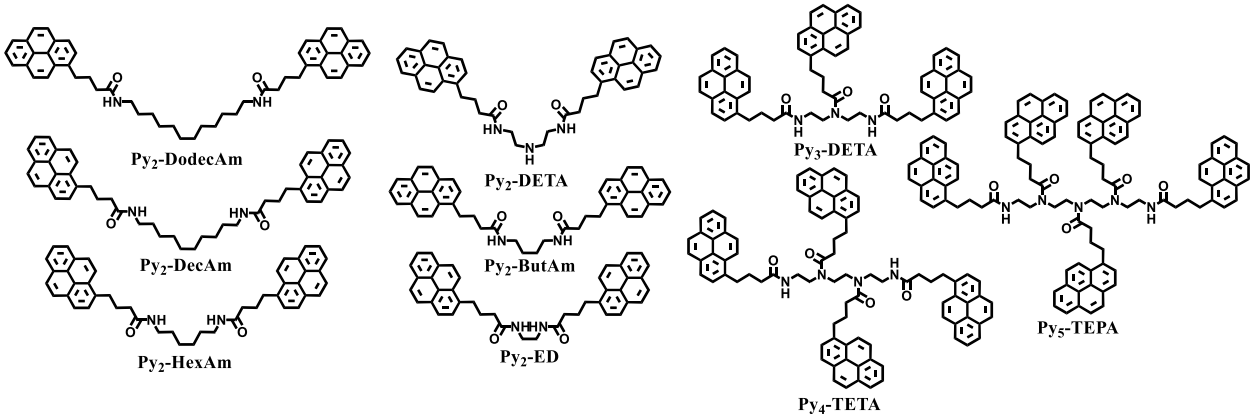

Figure 2. Chemical structures of the Py-DAs & Py-PAs prepared for this study.

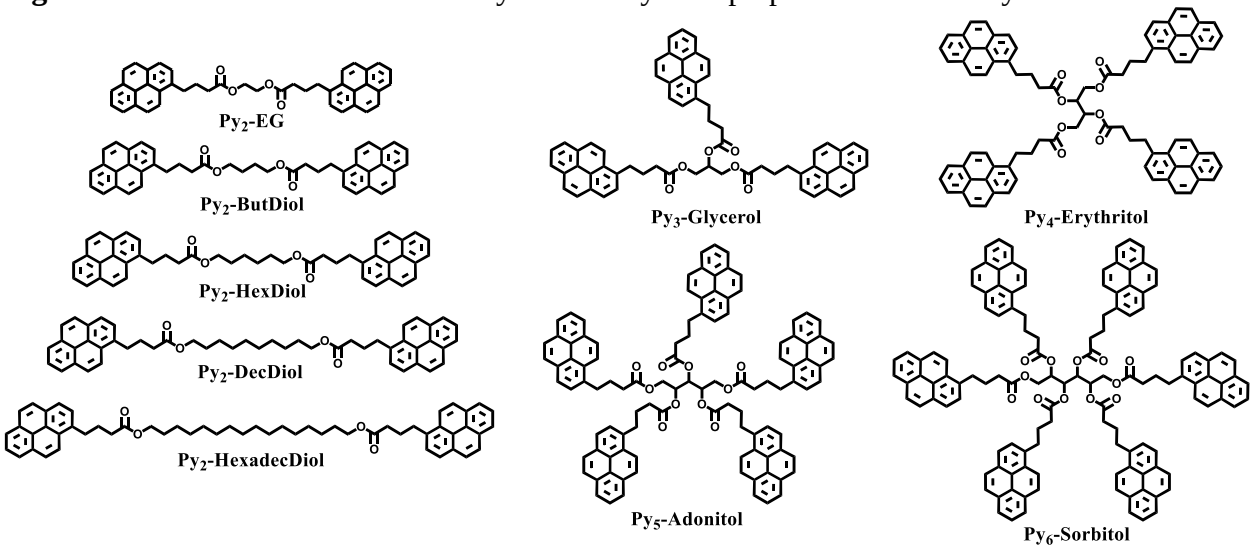

Figure 3. Chemical structures of the Py-DOs & Py-POs prepared for this study.

RESULTS & DISCUSSION

Integration of the SSF spectra and MFA of the TRF decays yielded the I_E/I_M ratio and <*k*>, respectively, for each PySM in THF, dioxane, DMF, and DMSO. $[Py]_{loc}$ was calculated for each Py-PA and Py-PO according to Equation 1 to generate plots of <*k*>-*vs*-$[Py]_{loc}$ in each solvent studied, which are shown in Figure 4.

The <*k*> values for the Py-DAs and Py-PAs in both DMF and DMSO seen in Figure 4B exhibit a linear trend against $[Py]_{loc}$, supporting the validity of Equation 1 for determination of $[Py]_{loc}$ and in turn the internal density of these PySMs by assuming that their internal segments obey Gaussian statistics.

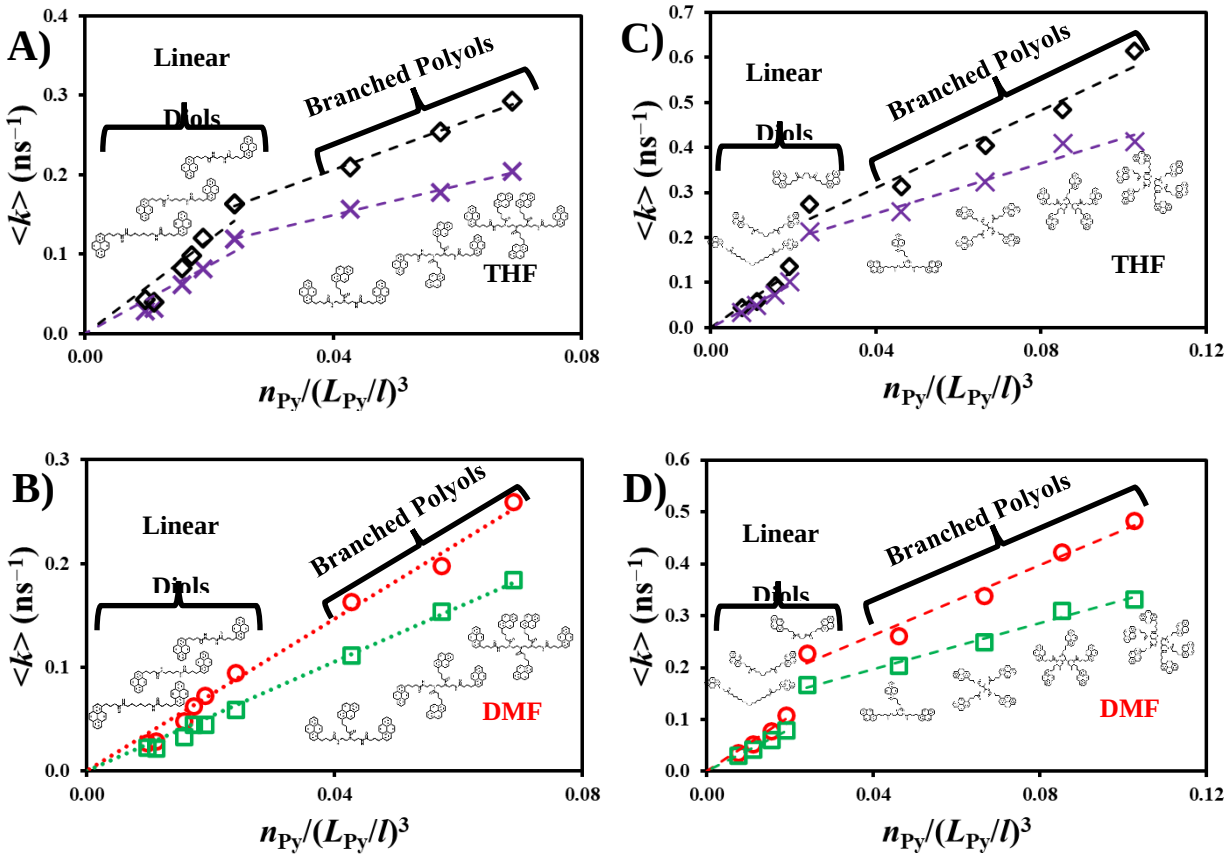

Figure 4. Plots of $<k>$-*vs*-$n_{Py}/(L_{Py}/l)^3$ obtained from the MFA of the monomer and excimer fluorescence decays for Py-DAs & Py-PAs acquired in A) THF and dioxane, and B) DMF and DMSO, and the Py-DOs & Py-POs acquired in C) THF and dioxane, and D) DMF and DMSO; [Py] = 2.5×10^{-6} M.

The Py-DOs and Py-POs span a wider range of $[Py]_{loc}$ values in Figure 4 than the Py-DAs and Py-PAs and thus reach higher $<k>$ values. The Py-PAs in THF and dioxane however showed a distinct breakpoint transitioning from the linear Py-DAs to the branched Py-PAs and a lessened sensitivity to $[Py]_{loc}$. The Py-POs showed the same trend of $<k>$-*vs*-$[Py]_{loc}$ in all 4 solvents, with a breakpoint between the linear diol Py-DOs and branched Py-POs.

It appears that the Py-POs in any solvent and the Py-PAs in less-polar THF and dioxane show a sensitivity to $[Py]_{loc}$ different from that of their linear Py-DO and Py-DA counterparts. This could be rationalized through a bias towards excimer formation among pyrenes being close to each other, where steric hindrance in the branched PySMs prevents each excited pyrene from 'seeing' each other pyrene in the Py-PO or Py-PA constructs. The fast rate of pyrene side chain motion on the Py-PO or Py-PA backbones could be providing too little time for distant pyrenes to interact before being bumped out of the way by a 'closer' pyrene to form an excimer. This effect may be eliminated for the Py-PAs in polar DMF and DMSO through polar solvent interactions with the amides which favours more sp^2 character in a Py-PA backbone, slowing the side-chain dynamics such that each pyrene can form excimer with each other pyrene in the PySM. A depiction of this effect is shown in Figure 5, highlighting the lower number of ground state pyrenes available for PEF and thus lower apparent $[Py]_{loc}$ value for the PySMs.

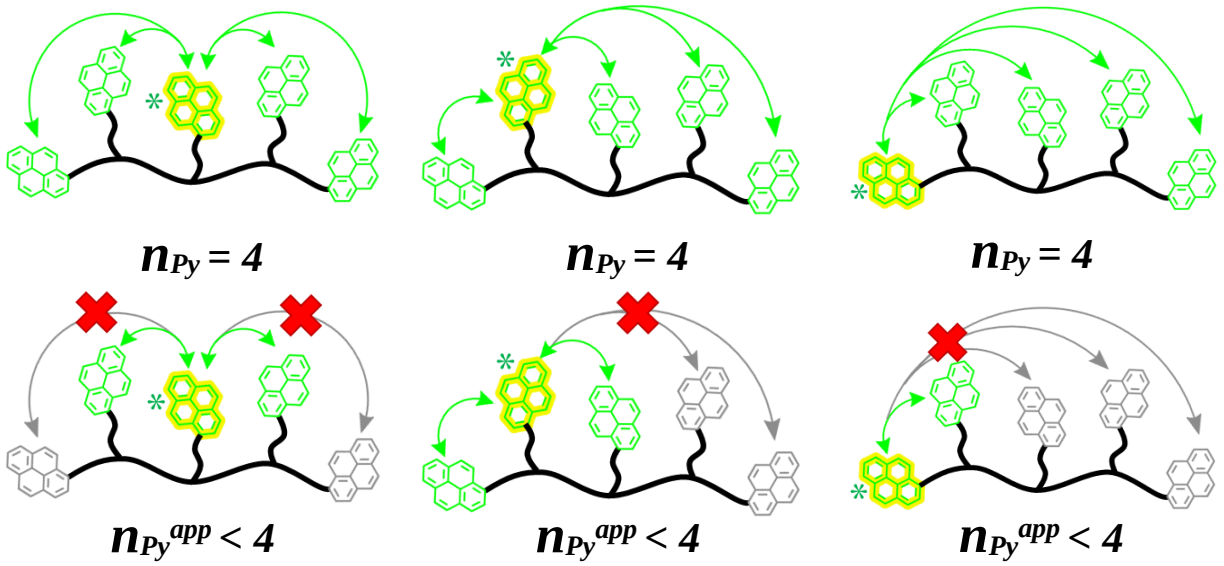

Figure 5. Depiction of reduced pyrene excimer formation using Py_5-Adonitol as example.

Since both the Py-PAs and Py-POs have a similar mix of difunctional and branched structures, it leaves the amide or ester groups, respectively, as the major difference between the two families, although a difference in the side-chain spacing on the backbone between the two could also be at play. It is worth noting that the pyrene groups are linked directly to amines in the backbone of the branched Py-PAs, whereas the ester linkages of the Py-POs reside 1 atom away from the polyol backbone, possibly providing a greater degree of flexibility and higher k_{diff} value to the Py-POs in contrast to the Py-PAs.

CONCLUSIONS

A series of PySMs were synthesized and their SSF spectra and TRF decays were acquired and analysed. Equation 1 was applied to determine $[Py]_{loc}$ for each Py-DA, Py-PA, Py-DO, and Py-PO before $\langle k \rangle$ was obtained from the MFA of the monomer and excimer fluorescence decays and plotted as a function of $[Py]_{loc}$ in THF, dioxane, DMF, and DMSO. The $\langle k \rangle$-*vs*-$[Py]_{loc}$ trends were linear for the Py-DAs and Py-PAs in DMF and DMSO proving the assumption that their internal segments obeyed Gaussian statistics in calculation of $[Py]_{loc}$ was valid. The Py-DAs and Py-PAs in THF or dioxane – along with the Py-DOs and Py-POs in all four solvents – showed a distinct breakpoint transitioning from the linear Py-DOs and Py-DAs to the branched Py-PAs or Py-POs which implied a lower number of ground state pyrenes available for PEF, and thus lower than predicted $\langle k \rangle$ values rationalized through a reduced efficiency for PEF among distant pyrene moieties. These results should open the door for future studies of the internal dynamics of more complex PyLMs and PySMs in solution.

REFERENCES

[1]. Winnik, M. A.; Redpath, T. The Dynamics of End-to-End Cyclization in Polystyrene Probed by Pyrene Excimer Formation. *Macromolecules* **1980**, *13*, 328-335.

[2]. Winnik, M. A.; Redpath, A. E. C.; Paton, K.; Danhelka, J. Cyclization dynamics of polymers: 10 Synthesis, fractionation, and fluorescent spectroscopy of pyrene end-capped polystyrenes. *Polymers* **1984**, *25*, 91-99.

[3]. Winnik, M. A. End-to-End Cyclization of Polymer Chains. *Acc. Chem. Res.* **1985**, *18*, 73-79.

[4]. Wilemski, G.; Fixman, M. Diffusion controlled intrachain reactions of polymers. I Theory. *J. Chem. Phys.* **1974**, *60*, 866-877.

[5]. Wilemski, G.; Fixman, M. Diffusion controlled intrachain reactions of polymers. II Results for a pair of terminal reactive groups. *J. Chem. Phys.* **1974**, *60*, 878-890.

[6]. Duhamel, J. New Insights in the Study of Pyrene Excimer Fluorescence to Characterize Macromolecules and their Supramolecular Assemblies in Solution. *Langmuir* **2012**, *28*, 6527-6538.

[7]. Thoma, J. L.; McNelles, S. A.; Adronov, A.; Duhamel, J. Direct Measure of the Local Concentration of Pyrenyl Groups in Pyrene-Labeled Dendrons Derived from the Rate of Fluorescence Collisional Quenching. *Polymers* **2020**, *12*, 2919.

8. Little, H.; Patel, S.; Duhamel, J. Probing the inner local density of complex macromolecules by pyrene excimer formation. *Phys. Chem. Chem. Phys.* **2023**, *25*, 26515.

[9]. Thoma, J. L.; Duhamel, J. Characterization of the Local Volume Probed by the Side-Chain Ends of Poly(oligo(ethylene glycol) 1-Pyrenemethyl ether methacrylate) Bottle Brushes in Solution Using Pyrene Excimer Fluorescence. *Macromolecules* **2021**, *54*, 9341-9350.

IRIS SAMPUTU
Chem. Eng.
Waterloo

Dehydration of Ethylene Glycol and Gases Using Polymeric and Novel Polymer Blend Membranes

DEHYDRATION OF ETHYLENE GLYCOL AND GASES USING POLYMERIC AND NOVEL POLYMER BLEND MEMBRANES

30/04/2025

Iris Samputu, Supervised by Prof. Xianshe Feng
Department of Chemical Engineering

UNIVERSITY OF WATERLOO | FACULTY OF ENGINEERING

OVERVIEW

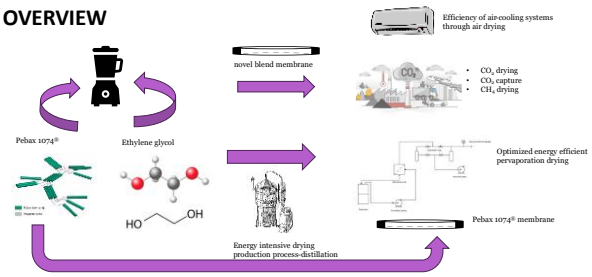

UNIVERSITY OF WATERLOO | FACULTY OF ENGINEERING

METHODS - GAS DRYING

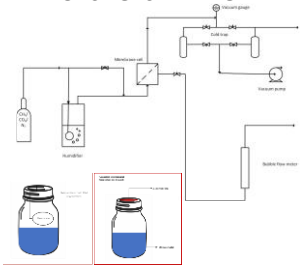

Solubility test | Inverted cup temperature test

Permeability:

$$P_{H_2O} = \frac{m_{H_2O} L}{A M_{H_2O} (P_f X - P_p Y) t}$$

$$P_{N_2,CH_4,CO_2} = \frac{Q_{N_2,CH_4,CO_2} L}{A(P_f - P_p) t}$$

Ideal selectivity:

$$\alpha_{ij} = \frac{P_i}{P_j}$$

Diffusivity and Solubility:

$$S_{H_2O} = \frac{\Delta m_{membrane}}{V_{membrane}\, M_{H_2O} P^{sat}_{H_2O}}$$

P=DS

$$D_i = D_{0i} \exp(-\frac{E_{D_i}}{RT})$$

$$S_i = S_{0i} \exp(-\frac{\Delta H_{s_i}}{RT})$$

UNIVERSITY OF WATERLOO | FACULTY OF ENGINEERING

RESULTS - GAS DRYI

Effect of % EG weight concentration

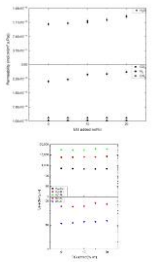

Effect of temperature and energy analysis

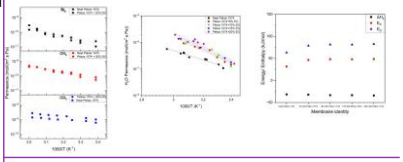

Effect of relative humidity (concentration of water) in feed

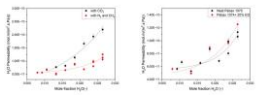

UNIVERSITY OF WATERLOO | FACULTY OF ENGINEERING

UNIVERSITY OF WATERLOO | FACULTY OF ENGINEERING | iBET | NSERC CRSNG

THANK YOU

JINXUAN ZHANG
Chem. Eng.
Waterloo

Interfacially Crosslinked Poly(vinyl alcohol)/Poly(vinyl amine) Composite Membranes Incorporated with Silver for Facilitated Olefin/Paraffin Separation

INTERFACIALLY CROSSLINKED POLYVINYL ALCOHOL/POLYVINYL AMINE COMPOSITE MEMBRANES INCORPORATED WITH SILVER FOR FACILITATED OLEFIN/PARAFFIN SEPARATION

Jinxuan Zhang, supervised by prof. Xianshe Feng
Chemical Engineering

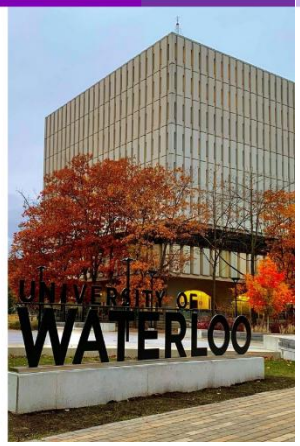

UNIVERSITY OF WATERLOO | FACULTY OF ENGINEERING

CSChE 2024

Olefin/paraffin separation

Feedstock Products

- Physical properties of C_2 and C_3 olefin and paraffin

	Kinetic diameter [nm]	Boiling point [K]	Critical temperature [K]	Polarizability $\alpha^{[a]}$ [cm]
Ethylene	0.423	169.5	282.3	42.5
Ethane	0.442	184.5	305.3	44.3
Propylene	0.468	225.5	364.9	62.6
Propane	0.506	231.1	369.8	63.3

- Facilitated transport membranes (FTMs)

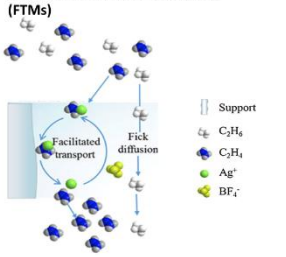

DOI : 10.1021/ie00022a002

UNIVERSITY OF WATERLOO | FACULTY OF ENGINEERING

Previous work- Polyvinyl alcohol/polyvinyl amine (PVA/PVAm) membrane

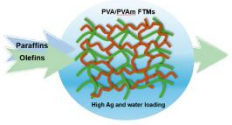

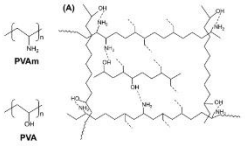

PVA/PVAm blend

In FTMs,
- ✓ Ag^+ enables the complexation reaction, and water enhances carrier mobility.

In PVA/PVAm FTMs
- ✓ Metal-chelating and hygroscopic properties.
- ✓ High and well-balanced Ag^+ and water content.
- ✓ Post-treatment (e.g., crosslinking) is required to ensure mechanical stability.

Permeability

$$P = \frac{Vl}{At(p_{feed} - p_{perm})}$$

P : the permeability in gas permeation
V (cm^3) : the volume of permeate gas
t (s) : the measurement time
l (cm) : the thicknesses of the membranes

Selectivity

$$\alpha_{i/j} = \frac{P_i}{P_j}$$

P_i and P_j : the permeability of component i and j

UNIVERSITY OF WATERLOO | FACULTY OF ENGINEERING

PVA/PVAm-Ag^+ composite FTMs

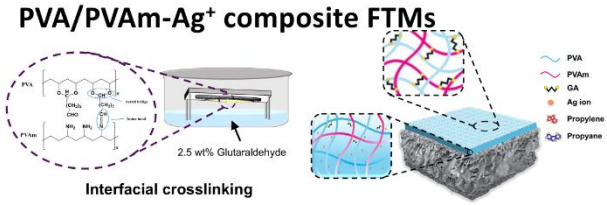

Interfacial crosslinking

- FTIR analysis

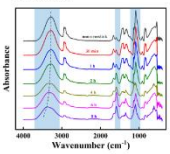

- SEM image for the bottom and surface

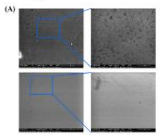

- Ag^+ and water content

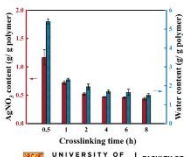

UNIVERSITY OF WATERLOO | FACULTY OF ENGINEERING

Results

- Olefin permeability

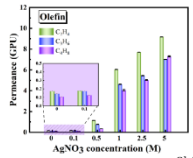

- Paraffin permeability

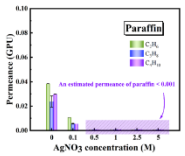

- Olefin/paraffin selectivity

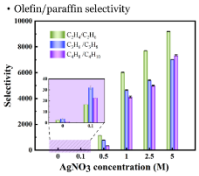

UNIVERSITY OF WATERLOO | FACULTY OF ENGINEERING

ACKNOWLEDGEMENTS

NSERC CRSNG
NOVA Chemicals
ALBERTA INNOVATES

Thanks to prof. Xianshe Feng and my group members!

UNIVERSITY OF WATERLOO | FACULTY OF ENGINEERING

HOSSEIN HIPAKCHI
Chem. Eng.
Waterloo

Highly Conductive Waterborne Polyurethane for Direct Ink Writing of 3D-Printed Healthcare Sensors: Design and Fabrication

HIGHLY CONDUCTIVE WATERBORNE POLYURETHANE FOR DIRECT INK WRITING OF 3D -PRINTED HEALTHCARE SENSORS: DESIGN AND FABRICATION

3/21/2025

Hossein Ipakchi
Supervised by Professor Tizazu Mekonnen

UNIVERSITY OF WATERLOO | FACULTY OF ENGINEERING

Background

Waterborne Polyurethane (WPU)

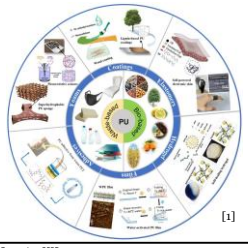

[1]

Direct Ink Writing (DIW)

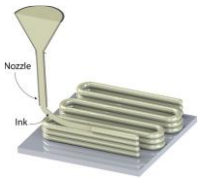

[1]Recent Advances in Environment-Friendly Polyurethanes from Polyols Recovered from the Recycling and Renewable Resources: A Review

Objectives

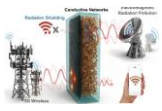

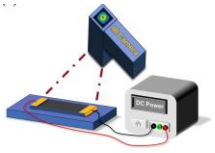

[1]Directional Electromagnetic Interference Shielding Based on Step-Wise Asymmetric Conductive Networks.

Experimental

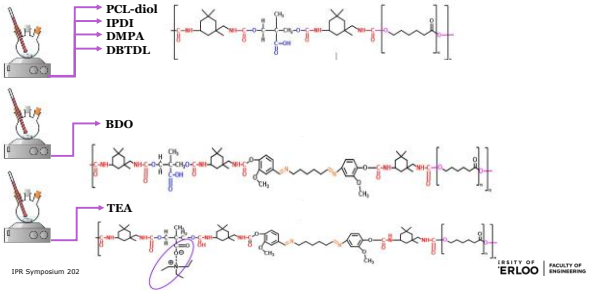

Results

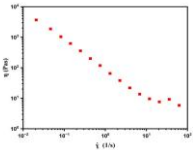

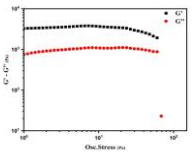

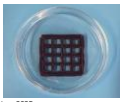

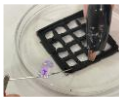

Conclusions and Next steps

Conclusions:

1- WPU with an NCO/OH ratio of 1.25 ensures a stable liquid system.

2- Graphene oxide, used as a rheology modifier at a 3 wt% concentration, enables 3D-printing capability in WPU.

3- The printed part exhibits electrical conductivity at 3V.

Next steps:

- Optimize the ink formula and processing conditions.
- Utilizing Printed Parts for the Advancement of Human Healthcare Sensors.

JIMMY PAPAZOTOS
Chem. Eng.
Waterloo

Highly Selective Conductive Polymer Design for Gas Sensing Applications

HIGHLY SELECTIVE CONDUCTIVE POLYMER DESIGN FOR GAS SENSING APPLICATIONS

Jimmy Papazotos,
Department of Chemical Engineering
Printable Electronic Materials Lab

UNIVERSITY OF WATERLOO | FACULTY OF ENGINEERING

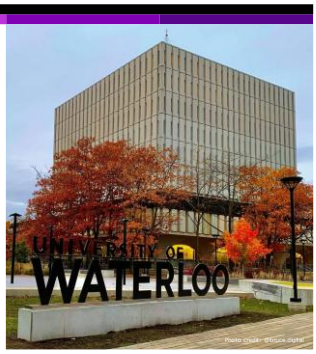

Conductive Polymers and their Role in Electronics

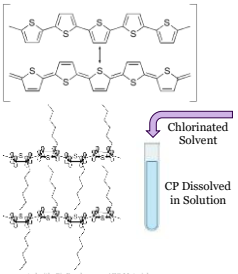

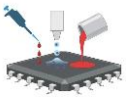

Solution Processability

Flexibility

Structural Customization

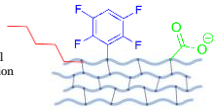

UNIVERSITY OF WATERLOO | FACULTY OF ENGINEERING

Design for Analyte Selectivity in Gas Sensitive Polymers

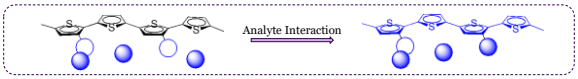

Analyte: Ethanol

- Molecular Size
- H-Bonding

Material Requirements:

- Electrical conductivity
- Solution processable
- Selective to ethanol molecular size
- Selective to hydrogen bonding

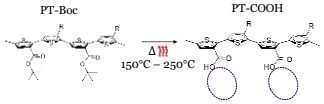

UNIVERSITY OF WATERLOO | FACULTY OF ENGINEERING

Size Selective Gas Sensing Response

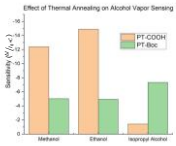

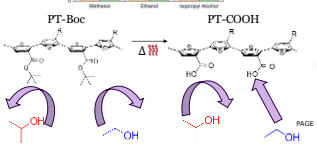

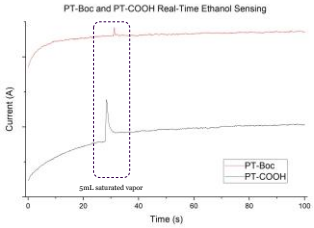

UNIVERSITY OF WATERLOO | FACULTY OF ENGINEERING

Chemical Selectivity with Interfering VOCs

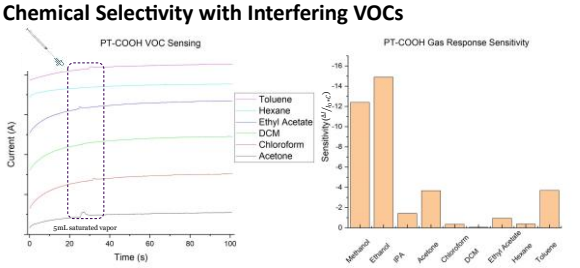

UNIVERSITY OF WATERLOO | FACULTY OF ENGINEERING

ANY QUESTIONS?

NSERC CRSNG

Canada NRC·CNRC

WATERLOO INSTITUTE FOR nanotechnology

WATERLOO ENGINEERING

CARLOS VILLAFANE
Chem. Eng.
Waterloo

Eco-Friendly Electrochemically Synthesized Graphene/Sodium Alginate Inks for 3D Printing Highly Conductive Hydrogels and Aerogels

Eco-Friendly, Highly Conductive, Electrochemically Synthesized Graphene/Sodium Alginate Inks for 3D Printing Tough Hydrogels and Aerogels

Carlos Villafane, Rahin Ali, Ziyu Zhuge, Milad Kamkar*

*Milad.kamkar@uwaterloo.ca

Engineering applications are facing an ever-growing list of performance and sustainability demands as our society evolves. The need for sustainable materials that can be tailored for specific applications is more urgent than ever. We are living in a time where it's no longer enough to design for function alone—we must also consider what happens to our devices after their useful life ends. Sustainability is not just a current issue—it is an accelerating global challenge. For example, the volume of electronic waste (e-waste) has doubled over the past two decades, with more than 50 million tonnes produced annually. As this trend continues, developing materials and technologies that are not only high-performing but also environmentally responsible is critical to ensuring a more circular and resilient future [1]. At the same time the demand for consumer electronics is expected to grow steadily and reach USD 2.321 billion by 2035 [2].

In this regard, technological advances help us build society as requirements change and evolve. More specifically, advances in materials design and engineering are responsible for delivering solutions to society's problems. A study published by Petrașcu et Al. showed that the field of smart materials has been experiencing significant growth due to the features its advances bring in the development of high-performance products and applications [3]. In other words, the development of more advanced materials directly enables the creation of better, more efficient, and more versatile applications across a wide range of industries. For these reasons we present a formulation of an eco-friendly, 3D printable, conductive hydrogel for the sustainable manufacturing of electronics and electromagnetic shields. Herein, we showcase the potential application of these 3D structures for electromagnetic interference (EMI) shielding. This study systematically identifies the optimal ratio of sodium alginate and electrochemically synthesized graphene nanosheets (EGNs) for 3D printing, featuring a high electrical conductivity and thus outstanding EMI shielding efficiency of up to 27 dB.

To justify the selection of sodium alginate and EGN, we will consider them individually. Sodium alginate (SA) is a natural biopolymer comprised of β-d-mannuronic acid (M) and αl-guluronic acid (G) and it can be extracted from kelp of algae or bacteria [4]. The interest in this component is related to its gelation capabilities and the ability to enhance the mechanical properties of composite

materials. The mechanical properties of SA are dependent on the molecular arrangement of its structure [5]. This biopolymer can be easily degraded through enzymatic processes, is non-toxic and non-contaminating, and can be extracted from a variety of natural sources, making it an attractive candidate for sustainable material development.

On the other hand, EGNs confer electrical conductivity and EMI shielding capabilities to the hydrogel by virtue of its appreciable electrical properties through different mechanisms, which will be discussed in the following paragraphs. What makes EGNs sustainable is not the intrinsic nature of the nanosheets themselves, but rather the synthesis process used to produce them. In the work presented, sustainability is achieved through green, low-impact fabrication methods, which reduce the use of harmful chemicals and minimize environmental footprint. The electrochemically synthesized nanosheets arise after a process comp exfoliation and filtration described in detail elsewhere [6] which bypasses the need for harsh chemicals and extensive energy processes that threaten the environment.

Since the components are inherently ecofriendly and conductive, the next step consisted of finding the optimal concentration and ratio of SA and EGNs to achieve a 3D printable hydrogel. This was done by preparing 32 different combinations of concentrations arising from SA in four different levels, i.e., 8, 10, 12 and 14 wt%, and EGNs in eight levels 0.15, 0.25, 0.5, 0.75, 1.00, 1.20, 1.40, and 1.80 wt%. Figure 3 illustrates the step-by-step process for hydrogel preparation.

To reduce the number of candidates, a simple test was performed in which hydrogels were transferred to a vial and inverted for 1 minute. Figure 1 presents the results of this preliminary screening test. If a hydrogel flowed easily within the designated time frame, it was deemed ineligible for further assessment, effectively eliminating over 50% of the initial sample pool from continued evaluation. Indeed, having yield stress is a prerequisite for a hydrogel to be printable.

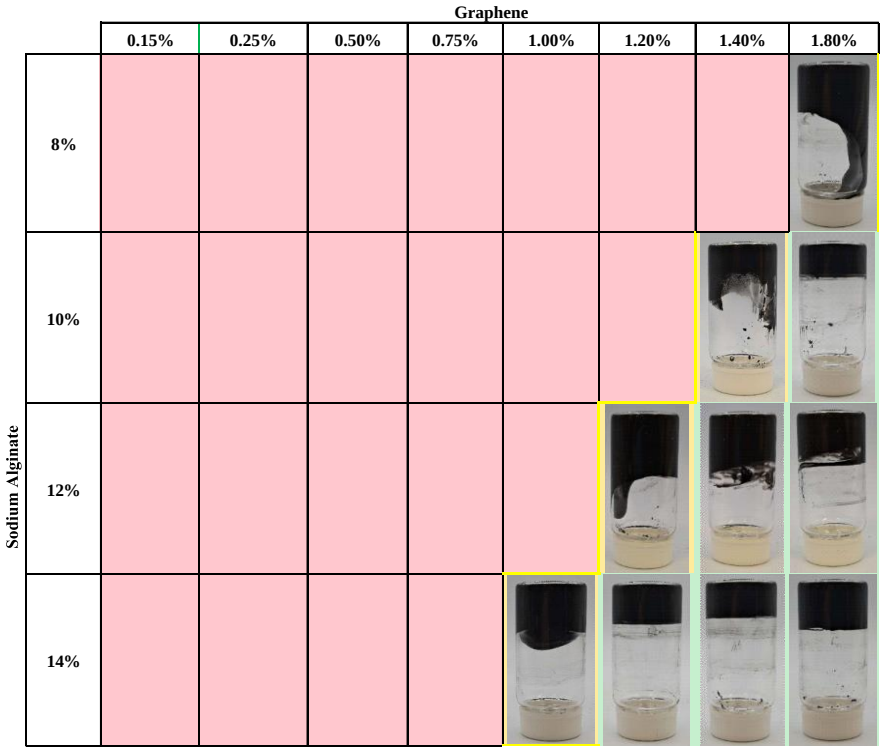

Figure 1. Results of 1 minute vial inversion test. A heatmap consisting of three colors. Red implies a failed test, yellow implies the candidate held its position for 1 minute and flowed afterwards requiring further assessment, green implies a passed test.

To further evaluate the behavior of the hydrogel, we conducted a filament formation test to narrow down the sample set. This test consisted of loading each candidate into the Cellink BioX printer and extrude each sample to observe whether a continuous filament with shear thinning behavior could be formed. If a candidate formed the filament a green circle would be assigned to its corresponding location in the heatmap. On the other hand, if no continuous filament could be formed a red cross would be assigned. The results are presented in Figure 2. This strategy yielded six promising candidates which were evaluated and optimized for printing. From a research strategy standpoint first, we focused on the validation of the concept followed by a systematic identification of ideal ratio of concentration of materials. All samples were prepared following the procedure shown in Figure 3A.

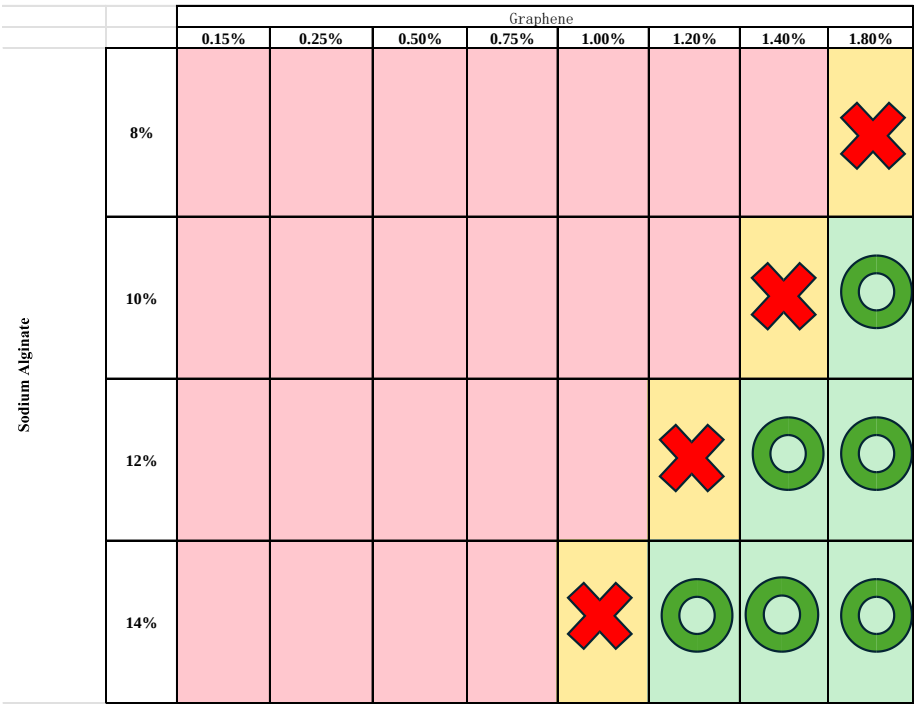

Figure 2. Results of shear thinning filament test. Updated heatmap template from figure 1 we in which we assign a red cross and green circle signifying failed and passed test, respectively.

Although all the filtered hydrogels demonstrated adequate printability, ionic crosslinking was performed to enhance their mechanical properties, as well as to ensure shape retention and improved handleability of the printed structures. To this aim, a 20% $CaCl_2$ solution was sprayed onto the printed construct immediately after the extrusion of each layer, initiating effective crosslinking. This process is shown in Figure 3B.

As a proof of concept, a hydrogel containing the highest concentrations of both components—14% SA and 1.8% EGNs—was prepared and assessed for electrical conductivity and electromagnetic interference (EMI) shielding. The formulation exhibited excellent printability (see Figure 3C) and promising functional performance, reaching shielding efficiency values up to 27 dB, thereby highlighting its potential for application in printed electronics.

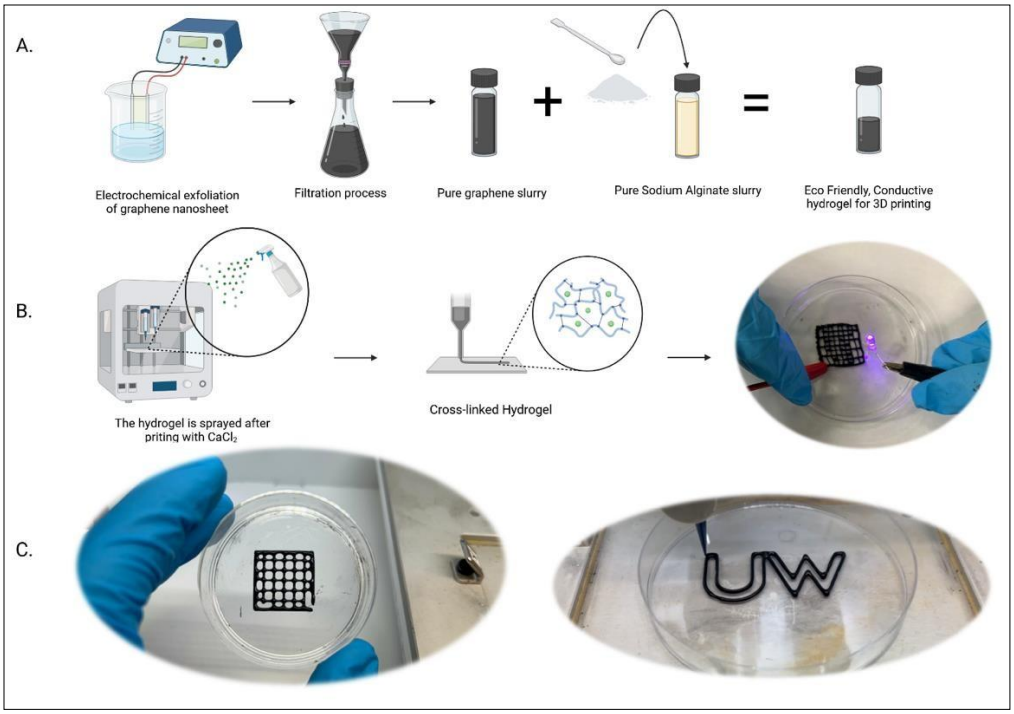

Figure 3. Schematic and results of the investigation. A. Synthesis of the ecofriendly conductive hydrogel for 3D printing. B. Printing and crosslinking processes. C. Results of printed structures using the hydrogel with highest concentration of SA and G.

References

[1] Future Markets, Inc., "The Global Market for Sustainable Electronics and Semiconductor Manufacturing 2025-2035," *Advanced and Emerging Technology Market Research*, Mar. 04, 2025. https://www.futuremarketsinc.com/the-global-market-for-sustainable-electronics-andsemiconductor-manufacturing-2025-2035/

[2] "Consumer Electronics Market Size, Share & Trends 2025-2035," *Metatech Insights*. https://www.metatechinsights.com/industry-insights/consumer-electronics-market-1290

[3] R. M., S.-G. Racz, and D.-M. Rusu, "Mapping Smart Materials' Literature: An Insight between 1990 and 2022," *Sustainability*, vol. 15, no. 20, p. 15143, Oct. 2023, doi: 10.3390/su152015143.

[4] B. Zhang, W. Lan, and J. Xie, "Chemical modifications in the structure of marine polysaccharide as serviceable food processing and preservation assistant: A review," *International Journal of Biological Macromolecules*, vol. 223, pp. 1539–1555, Nov. 2022, doi: 10.1016/j.ijbiomac.2022.11.034.

[5] Russo, R., Malinconico, M., & Santagata, G. (2007). Effect of cross-linking with calcium ions on the physical properties of alginate films. *Biomacromolecules*, *8*(10), 3193–3197. https://doi.org/10.1021/bm700565h

[6] E. Erfanian *et al.*, "Electrochemically synthesized graphene/TEMPO-oxidized cellulose nanofibrils hydrogels: Highly conductive green inks for 3D printing of robust structured EMI shielding aerogels," *Carbon*, vol. 210, p. 118037, Apr. 2023, doi: 10.1016/j.carbon.2023.118037.

JUNHAO HU
Chemistry
Waterloo

Harnessing Light: Exploring Pyrazine Polymers for Single-Molecule Organic Solar Cells

Harnessing Light: Exploring Pyrazine Polymers for Single-Molecule Organic Solar Cells

(Extended Abstract)

Junhao Hu

Supervisor: Prof. Schipper

Introduction

Organic solar cells (OSCs) have emerged as a transformative alternative to conventional inorganic photovoltaics, offering unparalleled advantages such as mechanical flexibility, ultralightweight architectures, and scalable solution-processability. These properties position OSCs as ideal candidates for next-generation applications, including wearable electronics,semi-transparent building-integrated systems, and disposable IoT devices. Despite these merits, the field remains constrained by its reliance on the bulk-heterojunction (BHJ) architecture—a design that blends donor and acceptor materials into a nanoscale interpenetrating network to facilitate charge separation [1].

In BHJ-based OSCs, photon absorption generates tightly bound electron-hole pairs (excitons), which must diffuse to donor-acceptor interfaces to dissociate into free charges. This process hinges critically on the energy offset between the donor and acceptor materials, as well as the nanoscale morphology of the blend [2]. Consequently, optimizing the phase-separated microstructure—to maximize interfacial area while maintaining percolation pathways for charge extraction—has dominated research efforts for decades. However, this morphology-dependent paradigm introduces intrinsic trade-offs between charge generation, recombination, and stability, limiting the achievable power conversion efficiencies (PCEs) and complicating large-scale fabrication [2,3].

In this work, we propose an alternation for conventional BHJ strategies by exploring single-material organic solar cells (SM-OSCs). Our approach circumvents the need for intricate morphology control by designing a unified photoactive material capable of spontaneous exciton dissociation. Central to this concept is the suppression of exciton binding energy (*Eb*)—the energy barrier that must be overcome to split excitons into free charges. Based on Wannier exciton model, the *Eb* is reverse proportional to the dielectric constant which is also correlated to polarity of the material. The higher the polarity of the material is, the higher the dielectric constant and thus the lower Eb [4]. We hypothesize that excitons can self-dissociate immediately upon formation, eliminating reliance on donor-acceptor interfaces. This would not only simplify device fabrication but also mitigate recombination losses inherent to BHJ systems.

Experiments & Results

Our previous work investigated bithiazole-N,N-dioxide compounds. We observed that as we progress from bithiazole to mono-N-oxide and finally to di-N-oxide, the exciton binding energy Eb is dramatically reduced. This reduction was determined by subtracting the optical band gap (obtained via UV–vis spectrometry) from the electrochemical gap measured by cyclic voltammetry. In our initial studies, we designed small conjugated molecules with a bithiazole core; after oxidation to form the mono-N-oxide and di-N,N-dioxide derivatives, Eb decreased from 684 meV (bithiazole) to 69 meV (bithiazole-N,N-dioxide). Time-dependent photoluminescence

measurements confirmed this substantial reduction, bringing the exciton binding energy into the range typical for perovskite solar cells (50–100 meV) [5].

Encouraged by these findings, we next aimed to broaden the light absorption range by incorporating a "push–pull" architecture. By introducing electron-donating groups (such as triphenylamine) and electron-withdrawing groups (such as cyanoacrylate) into the molecular framework, we successfully extended the absorption spectrum to cover most of the visible region, up to 580 nm [6,7].

However, the intrinsic insolubility of these bithiazole-N,N-dioxide compounds made film fabrication challenging. Considering that most high-performance organic solar cells are polymer-based and offer improved solubility, we opted to replace the bithiazole-N,N-dioxide core with a pyrazine-1,4-N,N-dioxide unit to develop a polymeric system [8,9]. For the synthesis of this polymer, we employed a direct arylation reaction with thiophene [10]. To enhance the solubility of the di-N,N-oxide pyrazine unit, we pre-installed a long alkyl chain on the starting material prior to oxidation. We also explored 3,4-dihexylthiophene and bithiophene as coupling partners. All direct arylation reactions proceeded efficiently, and UV–vis spectroscopy revealed an absorption range extending up to 600 nm. We are currently investigating additional coupling partners to further extend absorption across the entire visible spectrum, thereby maximizing light-harvesting capabilities.

In parallel, we expanded our monomer library by synthesizing novel di-N,N-oxide derivatives. Using trifluoroperacetic acid (generated *in situ* from urea peroxide and trifluoroacetic acid), we oxidized 2,5-dibromopyrazine and 2,5-dichloropyrazine to their respective 1,4-dioxide forms. These intermediates enabled versatile functionalization via nucleophilic aromatic substitution (SNAr) [8,11]. For example, we successfully synthesized 2,5-bis(octyloxy)pyrazine-1,4-dioxide, demonstrating the feasibility of tailoring solubility and electronic properties through side-chain engineering.

Conclusion

In summary, our investigation demonstrates that enhancing molecular polarity through the incorporation of N-oxide motifs offers a promising pathway for the development of single-material organic solar cells (SM-OSCs). Our systematic approach—progressing from bithiazole to mono-N-oxide and finally to di-N,N-dioxide derivatives—successfully reduced the exciton binding energy from 684 meV to 69 meV, thereby facilitating spontaneous exciton dissociation. Furthermore, the integration of a push–pull architecture significantly broadened the absorption spectrum up to 600 nm, and the transition to a polymeric system based on pyrazine-1,4-N,N-dioxide addressed solubility challenges while maintaining efficient light-harvesting capabilities. The expansion of our monomer library via versatile synthetic routes further underscores the potential of side-chain engineering in tuning both solubility and electronic properties. Collectively, these findings validate the feasibility of our SM-OSC approach as a viable alternative to traditional BHJ systems and lay the groundwork for future advancements in high-efficiency, scalable organic photovoltaic technologies.

Figure and Graph

Figure 1. Optical and electrochemical properties of extended p-conjugated bithiazole series, with time-dependent photoluminescence measurements of bis(4-hexylphenyl)-bithiazole series [6].

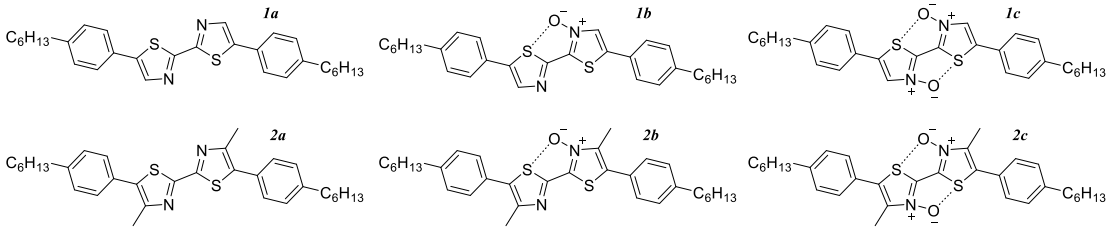

Entry	$E_{g[ec]}$ (meV)	$E_{g[opt]}$ (meV)	E_b (meV)	***Entry***	$E_{g[ec]}$ (meV)	$E_{g[opt]}$ (meV)	E_b (meV)
1a	2950	2800	150	***2a***	2660	2600	60
1b	2780	2750	30	***2b***	2560	2540	20
1c	2620	2700	-80	***2c***	2480	2520	-40

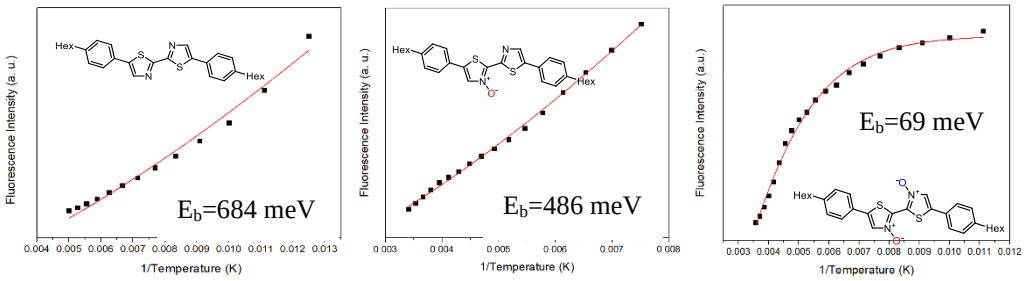

Figure 2. UV-vis spectrum of mono-N-oxide bithiazole and poly (N,N-dioxide pyrazine-bithiophene)

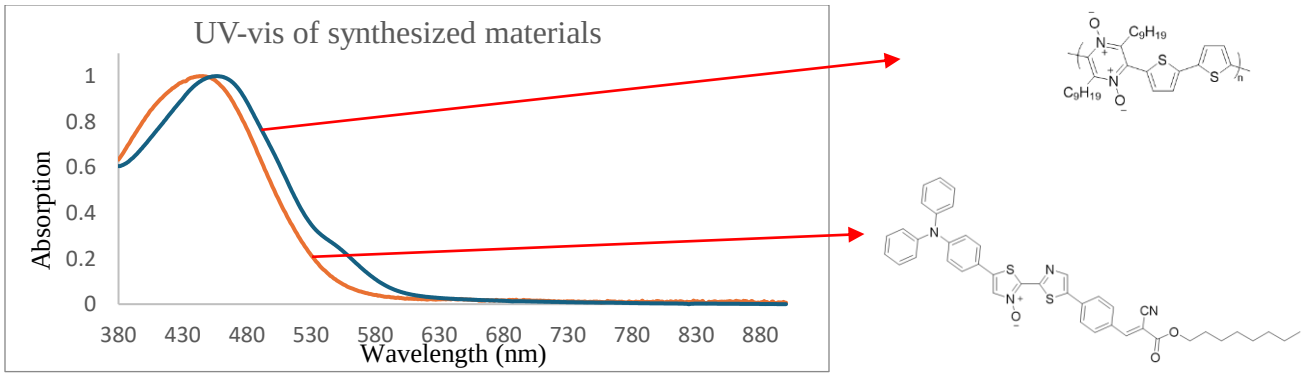

Figure 3. Reaction scheme of direct arylation polymerization of di-N,N-oxide pyrazine derivatives

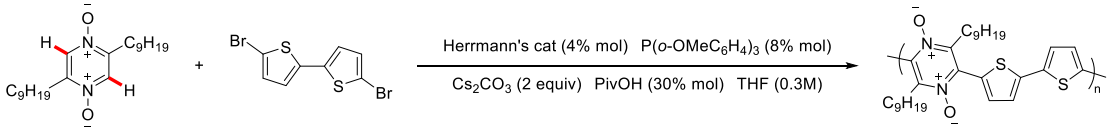

Acknowledgement

I would like to thank Franklin Frasca and Dr. Jean Duhamel for their assistance with the time-dependent photoluminescence measurements.

Reference

(1) Yi, J.; Zhang, G.; Yu, H.; Yan, H. Advantages, Challenges and Molecular Design of Different Material Types Used in Organic Solar Cells. *Nature Reviews Materials*. Nature Research January 1, 2024, pp 46–62.

(2) Roncali, J.; Grosu, I. The Dawn of Single Material Organic Solar Cells. *Advanced Science*. John Wiley and

Sons Inc. January 9, 2019.

(3) Lucas, S.; Kammerer, J.; Pfannmöller, M.; Schröder, R. R.; He, Y.; Li, N.; Brabec, C. J.; Leydecker, T.; Samorì, P.; Marszalek, T.; Pisula, W.; Mena-Osteritz, E.; Bäuerle, P. Molecular Donor–Acceptor Dyads for Efficient Single-Material Organic Solar Cells. *Solar RRL* **2021**, *5* (1).

(4) Grunert, M.; Großmann, M.; Runge, E. Predicting Exciton Binding Energies from Ground-State Properties. *Phys Rev B* **2024**, *110* (7).

(5) Yoo, J. J.; Seo, G.; Chua, M. R.; Park, T. G.; Lu, Y.; Rotermund, F.; Kim, Y. K.; Moon, C. S.; Jeon, N. J.; Correa-Baena, J. P.; Bulović, V.; Shin, S. S.; Bawendi, M. G.; Seo, J. Efficient Perovskite Solar Cells via Improved Carrier Management. *Nature* **2021**, *590* (7847), 587–593.

(6) Sinclair, G. S.; Claridge, R. C. M.; Kukor, A. J.; Hopkins, W. S.; Schipper, D. J. N-Oxide S-O Chalcogen Bonding in Conjugated Materials. *Chem Sci* **2021**, *12* (6), 2304–2312.

(7) Sinclair, G. S.; Kukor, A. J.; Imperial, K. K. G.; Schipper, D. J. Transition-Metal-Free Ipso-Arylative Condensation. *Macromolecules* **2020**, *53* (13), 5169–5176.

(8) Kayhan Göktürk, A.; Porter, A. A. E.; Sammes, P. G. Pyrazine Chemistry. Part 13. Preparation and Reactions of Pyrazine N-Oxides Related to Mycelianamide. *J Chem Soc Perkin 1* **1982**, 953–959.

(9) Chen, Z.; Ye, D.; Xu, G.; Ye, M.; Liu, L. Highly Efficient Synthesis of 2,5-Disubstituted Pyrazines from (Z)-β-Haloenol Acetates. *Org Biomol Chem* **2013**, *11* (39), 6699–6702.

(10) Pouliot, J. R.; Grenier, F.; Blaskovits, J. T.; Beaupré, S.; Leclerc, M. Direct (Hetero)Arylation Polymerization: Simplicity for Conjugated Polymer Synthesis. *Chemical Reviews*. American Chemical Society November 23, 2016, pp 14225–14274.

(11) Blake, K. W.; Sammes, P. G. *Preparation and Reactions of Some Substituted Pyrazine Di-N-Oxides*.

YONGLIN WANG
Chem. Eng.
Waterloo

Development of High-Performance Organic Cathode Materials Based on Coordination Polymers for Lithium-Ion Batteries

Winner of the 2023 IPR Award for Academic Excellence in Polymer Science/Engineering

Extended Abstract

Title: Development in Coordination Polymer-Based Organic Cathode Materials for Lithium-Ion Batteries: Enhanced Stability and Electrochemical Performance

The development of high-performance lithium-ion batteries (LIBs) requires advances in cathode materials that offer improved stability, capacity, and cyclability. Organic cathodes, particularly those based on quinone derivatives such as 2,5-dihydroxy-1,4-benzoquinone (DHBQ), hold significant promise due to their high theoretical capacities and environmental advantages. However, their practical application is hindered by issues such as solubility in electrolytes, structural degradation, and limited cycling stability. Introducing metal ligands and forming coordination polymers can mitigate the solubility issues of organic cathode materials in electrolytes. However, this approach may reduce energy density since most metals do not participate in battery redox reactions. To address this challenge, we synthesized two types of coordination polymers, each adopting a distinct strategy to stabilize DHBQ: (1) incorporating transition metal complexes that actively participate in redox reactions, and (2) utilizing lightweight metal coordination to minimize energy density loss while still reducing solubility. Additionally, we investigated the degradation mechanisms of these coordination polymers in batteries and proposed different strategies to enhance their performance and stability.

The first study investigates the synthesis and electrochemical performance of a cobalt (II)-DHBQ-based coordination polymer (Co-DHBQ·$2H_2O$) as a cathode material. This approach represents the first strategy, where metal complexes actively participate in the battery reaction, enhancing capacity retention. The successful synthesis of Co-DHBQ·$2H_2O$ effectively reduced the solubility of DHBQ in the electrolyte, addressing one of the major limitations of organic cathodes. To further understand the cycling performance, we explored the degradation mechanism of Co-DHBQ·$2H_2O$-

based batteries and identified key factors affecting long-term stability. Our study revealed that the presence of coordinated water plays a crucial role in maintaining the structural integrity of the material and enabling a reversible four-electron transfer process (redox reactions occurring in both DHBQ and Co). Additionally, controlling the voltage window was found to be essential for optimizing capacity retention and stability. With a carefully adjusted voltage range, the Co-DHBQ·$2H_2O$ cathode demonstrated a high initial discharge capacity of 783 mAh/g and excellent long-term stability, retaining 199 mAh/g after 750 cycles. To highlight the importance of coordinated water, we compared the electrochemical performance of Co-DHBQ·$2H_2O$ with its anhydrous counterpart. The removal of coordinated water led to significant structural instability, resulting in rapid capacity decay and reduced cycling stability. In contrast, Co-DHBQ·$2H_2O$ exhibited superior long-term performance due to the stabilizing effect of coordinated water, which maintained the layered structure and enabled efficient lithium-ion transport. These findings emphasize that coordinated water plays a crucial role in preserving the material's integrity and optimizing electrochemical performance. The study highlights the importance of coordination polymer chemistry, water coordination, and voltage window control in the development of high-performance coordination polymer-based cathode materials.

Building on these findings, we then investigated an alternative strategy using Li_2DHBQ, a coordination polymer designed to minimize energy density loss while reducing solubility. This approach represents the second stabilization strategy, emphasizing the trade-off between solubility reduction and maintaining high specific capacity. To further understand the limitations of Li_2DHBQ-based batteries, we investigated their degradation mechanism, which was primarily caused by the pulverization of active material during cycling. This structural degradation led to capacity loss and reduced cycle life, highlighting the need for stabilization strategies. To mitigate

the pulverization process, we employed a novel approach using reduction-induced SEI formation. Lowering the discharge cutoff voltage to 0.5 V facilitated the formation of an organic-rich SEI layer on the Li_2DHBQ cathode, which effectively prevented material fragmentation and stabilized the electrode morphology. As a result, the Li_2DHBQ-based battery demonstrated a significant improvement in cycling stability, retaining 170 mAh/g after 200 cycles at 500 mA/g. This approach proved highly effective in preserving the cathode structure compared to conventional cycling conditions, where the capacity retention was only 87 mAh/g. These findings emphasize the importance of SEI formation and optimization in stabilizing organic coordination polymer-based cathodes for LIBs.

To further enhance electrode durability, we introduced fluoroethylene carbonate (FEC) as an electrolyte additive to form an artificial cathode-electrolyte interphase (CEI) layer on the Li_2DHBQ cathode. The optimized 1% FEC concentration facilitated the formation of a thin, uniform, and protective CEI, which effectively prevented electrolyte decomposition, minimized cathode fragmentation, and enhanced lithium-ion transport. Electrochemical characterization revealed that the CEI layer significantly improved battery stability, reducing the capacity decay rate to 0.013% per cycle between the 100th and 200th cycles. Furthermore, the FEC-modified cathode maintained a high capacity of 185 mAh/g at 500 mA/g, demonstrating excellent high-rate capability. This study highlights the advantages of CEI engineering as an alternative to conventional SEI formation, providing a more controlled and effective approach to stabilizing organic cathodes. These findings underscore the potential of electrolyte additive-induced interphase engineering in improving the long-term performance and durability of lithium-ion batteries.

In summary, we explored strategies to improve the stability and electrochemical performance of

coordination polymer-based organic cathodes for lithium-ion batteries. We demonstrated that Co-DHBQ·2H_2O effectively reduces DHBQ solubility while maintaining structural stability through coordinated water interactions, enabling a four-electron redox process and achieving 199 mAh/g after 750 cycles. For Li_2DHBQ, we identified active material pulverization as a key degradation mechanism and addressed it using reduction-induced SEI formation, which significantly improved cycling stability (170 mAh/g after 200 cycles). To further enhance electrode durability, we introduced fluoroethylene carbonate (FEC) as an electrolyte additive, forming a protective CEI layer that minimized electrolyte decomposition and fragmentation, leading to a capacity of 185 mAh/g at 500 mA/g with improved long-term stability. These findings highlight the importance of water coordination, interfacial engineering, and electrolyte additives in stabilizing organic cathodes, providing a viable pathway for high-performance, long-life coordination polymer-based lithium-ion batteries.

Keywords: Coordination polymer, Organic cathode, Solid electrolyte interphase, Lithium-ion battery.

DONGHAN LIU
Chemistry
Waterloo

Interactions of Hydrophobically Modified PAMAM Dendrimers with Surfactant Aggregates Probed by Pyrene Excimer Formation

Interactions of Hydrophobically Modified PAMAM Dendrimers with Surfactant Aggregates Probed by Pyrene Excimer Formation

Donghan Liu, Sanjay Patel, Jean Duhamel

Institute for Polymer Research, Waterloo Institute for Nanotechnology, Department of Chemistry, University of Waterloo, 200 University Avenue West, Waterloo, ON N2L 3G1

INTRODUCTION

Endowed with a modular structure that can be adjusted to impart numerous properties, poly(amido amine) (PAMAM) dendrimers are being investigated for their potential use in waste water treatment, energy storage, and biomedical applications including the development of new generation carriers for targeted delivery systems.[1] However, the use of PAMAM dendrimers in the pharmaceutical field is hindered by the cytotoxicity of their numerous amino terminals.[2] Recently, studies have shown that hydrophobic modification of these primary amines significantly reduces cytotoxicity, which has led to a surge in research interest for hydrophobically modified PAMAM dendrimers (HM-PAMAM). To date, most studies on HM-PAMAM have focused on the imaging of tissues or cells for viability tests and they would benefit from a molecular level understanding of how HM-PAMAM interacts with cell membranes. For instance, determining the location, conformation, and internal dynamics of HM-PAMAM in lipid bilayers is of great importance to further develop drug-specific delivery systems and for understanding the mechanism of HM-PAMAM endocytosis.[3] Unfortunately, no experimental technique can currently deliver this information, which can only be obtained through molecular dynamics simulations.

Several techniques can be applied to probe the conformation of macromolecules in solution. They include scattering such as static (SLS) and dynamic (DLS) light scattering and small angle X-ray (SAXS) and neutron (SANS) scattering, circular dichroism (CD), intrinsic viscosity, and NMR. All these techniques have their pros and cons, but one common feature is the 1 – 10 g/L range of polymer concentrations typically needed to generate sufficient signal for analysis. However, the characterization of individual HM-PAMAM in the hydrophobic microdomains generated by 10-50 g/L aqueous solutions of surfactants or lipids would require HM-PAMAM concentrations that are at least 100 times more dilute, bringing the HM-PAMAM concentration below the workable concentration range of the more conventional techniques thus preventing their applicability. To address this problem, more sensitive techniques are needed. To this end, fluorescence experiments based on pyrene excimer formation (PEF) were conducted in this study to characterize the HM-PAMAM conformation at the molecular level as they interacted with surfactant aggregates. Fluorescence can probe macromolecules in the 1 – 10 mg/L concentration range, 3-to-4 orders of magnitude lower than the conventional methods. Although a drawback of PEF is that the conformation of the macromolecule might be affected by the hydrophobicity and bulkiness of the pyrene derivative used as a label, it should not be a concern in this study since pyrene is similar in size and hydrophobicity to the drugs commonly attached to PAMAM dendrimers. In other words, the pyrene-labeled PAMAM generation 0 dendrimers referred to as PyCX-PAMAM-G0 in this study, where *X* (= 4, 6, 8, 10, and 12) represents the number of carbon atoms used to link pyrene to the dendrimer, are excellent mimics of HM-PAMAM. The conformation of the PyCX-PAMAM-G0 samples was characterized as the dendrimers interacted with surfactant micelles prepared from pure sodium dodecyl sulfate (SDS), pure dodecyl trimethyl ammonium bromide (DTAB), and mixtures of SDS and DTAB in varying ratios. While pure SDS and DTAB micelles are spherical in aqueous solution, mixed micelles made of SDS and DTAB adopt a rod-like conformation[4] where the central cylindrical region is tightly packed with both surfactants in an approximately 1:1 ratio and the ends are hemispheres primarily composed of the surfactant in excess. A change in surfactant fraction only affects the length of the cylinder.

Examples of the structures generated by the surfactants and the conformation of the PAMAM associated with these structures are shown in Figure 1.

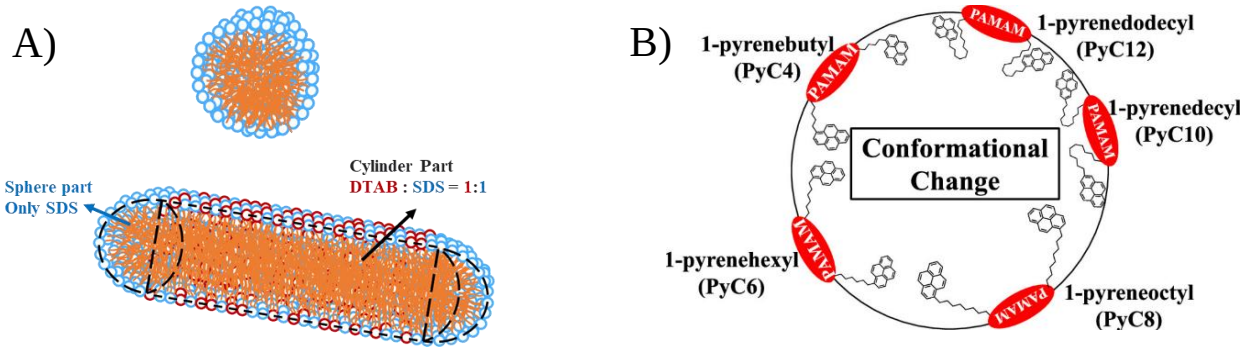

Figure 1. A) Structure of (top) an SDS micelle and (bottom) a mixed micelle composed of a 70:30 SDS:DTAB mixture. B) Conformation of PyCX-PAMAM-G0 inside a spherical micelle.

In this study, the average rate constant (<*k*>) for PEF was determined by fitting with a sum of exponentials the time-resolved fluorescence (TRF) decays of each PyCX-PAMAM-G0 in organic solvents and surfactant aggregates. The linear relationship found between <*k*> and the theoretical local concentration ($[Py]_{loc}$) for the PyCX-PAMAM-G0 in organic solvents demonstrated that the internal segments of the dendrimers obeyed Gaussian statistics. A similar relationship was also obtained for the PyCx-PAMAM-G0 samples with shorter linkers (*X*=4,6,8) in all surfactant aggregates indicating that these three dendrimers adopt the same conformation in organic solvents and in surfactant aggregates. However, <*k*> was found to significantly deviate from the linear relationship for the PyCX-PAMAM-G0 samples with longer linkers (*X*=10,12) in surfactant aggregates. Such drastic changes were attributed to a conformational change. Further investigation revealed that this conformational change occurs because the decyl and do decyl longer linkers tend to interact with the relatively more hydrophobic core of the pure surfactant micelles. In the mixed micelles, which adopted a rod-like shape, this deviation was less pronounced with increasing micelle size, which reflected a longer cylindrical section (see Fig. 1A). This observation suggested that the conformational change of dendrimers with a longer linker does not happen in the cylinder part which is sufficiently hydrophobic at the surface due to the close packing of SDS and DTAB molecules. Further demonstration of this finding is provided by the similar trends obtained from experiments with surfactant aggregates consisting of an 80:20 SDS:DTAB mixture at various NaCl concentrations. NaCl is found to induce an extension of the cylindrical region of the rod-like micelles, while the deviation of <*k*> for the dendrimers with longer linkers from the linear <*k*>-*vs*-$[Py]_{loc}$ relationship obtained for the dendrimers with the shorter linkers is attenuated with increasing NaCl concentration, indicating that the PyCX-PAMAM-G0 dendrimers experience an overall more hydrophobic environment.

EXPERIMENTAL

Chemicals: Sodium chloride, sodium dodecyl sulfate (SDS), dodecyl trimethyl ammonium bromide (DTAB), *N*,*N*-dimethyl formamide (DMF), dimethyl sulfoxide (DMSO), and chloroform were purchased from Sigma-Aldrich and used as received. The synthesis and characterization of the PyCX-PAMAM-G0 samples and the PAMAM-G0 sample end-labeled with 1-naphthaleneacetic acid (NpC2-PAMAM-G0) were described earlier.

UV–Vis Absorption Measurements: The absorption spectra were acquired on a Cary 100 UV–visible spectrophotometer with a 5.0 cm path length quartz cuvette. Compared to a traditional cuvette with a 1.0 cm path length, the longer 5.0 cm path length yielded a larger absorbance for the very dilute aqueous PyCX-PAMAM-G0 solutions. The detection of sharp peaks in the absorption spectra was taken as evidence that the highly hydrophobic 1-pyrenealkanoyl derivatives used to label the PyCX-PAMAM-G0 dendrimers were solvated inside the surfactant micelles.

Fluorescence measurements: The PyCX-PAMAM-G0 samples were excited at 344 nm. First, their steady-state fluorescence spectra were acquired by scanning the fluorescence intensity from 350 to 650 nm. The fluorescence decays of the pyrene monomer and excimer of the PyCX-PAMAM-G0 samples were acquired with an emission wavelength set at 375 and 510 nm and with a cutoff filter at 370 and 495 nm, respectively. The fluorescence decays of the pyrene monomer and excimer were analyzed globally according to the Model Free Analysis (MFA), which acknowledges that any fluorescence decay can be fitted with a sum of exponentials, to determine $<k>$ through Eq. 1. α_i and τ_i represents the pre-exponential factors and decay times of each exponential used in the decay analysis, respectively.

$$< k >= \frac{\sum_{i=1}^{n} a_i}{\sum_{i=1}^{n} a_i \tau_i} - \frac{1}{\tau_M} = \frac{1}{< \tau >} - \frac{1}{\tau_M} \quad \textbf{(1)}$$

Local Concentration of Pyrenyl Labels for a PyCX-PAMAM-G0 Sample: The local concentration ($[Py]_{loc}$) of pyrenyl labels within the macromolecular volume generated by the PyCX-PAMAM-G0 samples was obtained by dividing the number (n_{Py}) of ground-state pyrenyl labels by the cube of the average end-to-end distance (L_{Py}). For the PyCX-PAMAM-G0 samples with four pyrenyl labels, n_{Py} equals 3 since one of the four pyrenyl labels must be excited to be detected for fluorescence measurements and is required for PEF. The expression of L_{Py} has been derived mathematically for low-generation PAMAM dendrimers earlier and is given in Eq. 2.[5]

$$L_{Py}^2(N) = \left(2a + \frac{\left[2 - 2^{N+2} + (N+1) \times 2^{N+3} \right] b + 2^{N+1} c + 2^{N+1} - 1}{2^{N+2} - 1} \right) \times l^2 \quad \textbf{(2)}$$

In Eq. 2, N is the generation number equal to 0 for the PyCX-PAMAM-G0 samples, a is the number of carbon atoms in the linker connecting the pyrene moiety to the PAMAM dendrimer and equals X (= 4, 6, 8, 10, and 12), b (= 7) represents the number of non-hydrogen atoms in the aminoethyl propionamide building block of the PAMAM dendrimer, and c (= 4) is the number of non-hydrogen atoms in the ethylene diamine core of the dendrimer.

RESULTS AND DISCUSSION

The conformation of the PyCX-PAMAM-G0 samples were first studied in the two organic solvents DMF and DMSO at a concentration of 0.6 μM. Their SSF spectra are presented in Fig. 2A. MFA of their fluorescence decays yielded $<k>$ which increased linearly with increasing $[Py]_{loc}$ for both solvents in Fig. 2B. This result suggests that all internal segments of the PyCX-PAMAM-G0 samples linking every two pyrene pair obey Gaussian statistics. To probe the PyCX-PAMAM-G0 samples as they interacted with surfactant aggregates, each dendrimer was suspended with surfactants in chloroform before the chloroform was evaporated under a gentle flow of nitrogen to yield a film, which was dry for the samples with SDS but required that it be kept under vacuum overnight for the samples with DTAB to remove residual chloroform. After adding the required amount of water to the films, clear solutions of 0.5 to 1.0 μM PyCX-PAMAM-G0 samples were obtained in 50 mM surfactant aqueous solutions that yielded the well-resolved absorption bands expected from the pyrenyl labels and a well-defined rise time in the fluorescence decays of the pyrene excimer. Since the surfactant concentration of 50 mM was well above the critical micelle concentration of 8 mM for SDS and 15 mM for DTAB, the surfactants formed micelles that were hosting the PyCX-PAMAM-G0 samples. The same linear relationship was observed between $<k>$ and $[Py]_{loc}$ for the PyCX-PAMAM-G0 samples with shorter linkers (X=4, 6, 8) as shown in Fig. 2C, indicating that the conformation of these dendrimers in the surfactant micelles was the same as in pure solvents. Interestingly, $<k>$ obtained for dendrimers with longer linkers (X=10,12) significantly deviated from the linear relationship observed for the samples with the shorter linkers

resulting in a characteristic check mark pattern. To further investigate the cause of this change, FRET experiments were conducted whereby NpC2-PAMAM-G0 was mixed with the PyCX-PAMAM-G0 samples with X = 10 and 12 in the 50 mM surfactant solutions with an 80:20 SDS:DTAB mixture.

The fluorescence spectra of the NpC2/PyCX-PAMAM-G0 mixtures were compared to the sum of the fluorescence spectra acquired for the 50 mM SDS and DTAB solutions with NpC2-PAMAM-G0 only and PyCX-PAMAM-G0 only. The identical fluorescence spectra obtained for the NpC2/PyCX-PAMAM-G0 mixtures and the sum of the fluorescence spectra of the individual components of the mixtures ruled out FRET between the naphthalene- and pyrene-labeled dendrimers and confirmed that the surfactant micelles hosted isolated dendrimers. Meanwhile, L_{Py} of the dendrimers with longer linkers equaled 1.47 and 1.54 nm for X=10 and X=12, respectively, and was much smaller than the diameter of the SDS and DTAB micelles equal to 3.7 and 3.3 nm, respectively. Consequently, the checkmark pattern observed in Figure 2C was not a result of intermolecular interactions between dendrimers located inside a same micelle or dendrimer size. It was therefore concluded that it was caused by a conformational change of the dendrimer induced by strong hydrophobic interactions between the longer linkers and the more hydrophobic core of the pure surfactant micelles. A schematic representation of the conformational change expected for the PyCX-PAMAM-G0 samples with X = 10 and 12 is shown in Fig. 1B.

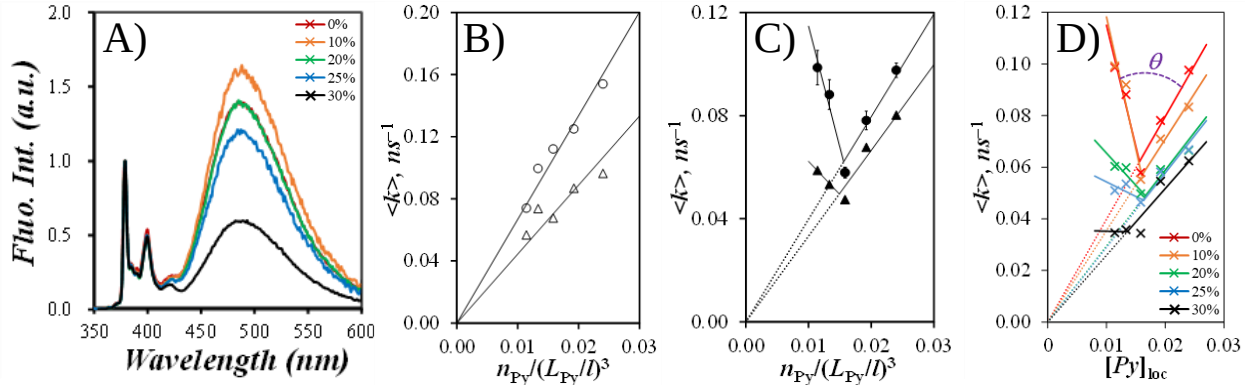

Figure 2. A) SSF spectra of PyCX-PAMAM-G0 in DMF. B) <*k*> for the PyCX-PAMAM-G0 samples in DMF and DMSO and C) 50 mM SDS and DTAB aqueous solutions. Symbols: (empty circles) DMF, (empty triangles) DMSO, (filled circles) SDS, (filled triangles) DTAB. D) <*k*> for the PyCX-PAMAM-G0 samples in a 50 mM aqueous solution of the (red) 100:0, (orange) 90:10, (green) 80:20, (blue) 75:25, and (black) 70:30 SDS:DTAB mixtures.

Experiments were then carried out in mixed micelles prepared from SDS and DTAB mixtures with the molar fraction (f_{DTAB}) of DTAB ranging from 0 (pure SDS) to 0.30 to investigate whether the geometry of the surfactant aggregates (spherical-*vs*-cylindrical) would affect the conformational inversion observed for the PyCX-PAMAM-G0 dendrimers in the pure surfactant micelles. <*k*> for all the dendrimer samples was plotted against $[Py]_{loc}$ in Fig. 2D. The dendrimers bearing shorter linkers always yielded a straight line that passed through the origin. For PyC10- and PyC12-PAMAM-G0, the checkmark pattern was seen in all the experiments with different SDS to DTAB ratios indicating that the conformational change always exists. However, the pattern became significantly less pronounced as f_{DTAB} increased. The effect was quantified with the angle ϕ, which is the angle between the <*k*>-*vs*-$[Py]_{loc}$ straight line formed by the short linker dendrimers and the trend line formed by the PyC8-, PC10-, and PyC12-PAMAM-G0 samples. The increase in ϕ is attributed to a reduction in the dendrimer conformational change happening in the cylinder part of the rod-like mixed micelles. Because the cylinder part is closely packed with oppositely charged SDS and DTAB molecules, its palisade is more hydrophobic than the palisade of pure

SDS or DTAB micelles. As a result, the hydrophobicity gradient from the center of the micelle to the palisade region in the rod-like micelles is much less pronounced and the drive for the longer alkyl linkers to interact with the hydrophobic core is reduced. In an extreme case, the linear relationship between <*k*> and $[Py]_{loc}$ would be restored and ϕ would equal 180°. This was not observed in Fig. 2D probably because the PyCX-PAMAM-G0 samples are randomly distributed in the rod-like micelles. Consequently, some dendrimers are located in the hemispheres at the ends of the rod-like micelles, which are primarily constituted of SDS molecules. The chemical environment and hydrophobicity in this region are expected to be similar to those found in the interior of pure SDS micelles where the check mark pattern is observed. Therefore, the check mark pattern is always observed but becomes less pronounced as the cylinder part grows longer with increasing DTAB content. Another notable effect is the decrease in the slope of the <*k*>-*vs*-$[Py]_{loc}$ straight lines for the dendrimers with a short linker. This is attributed to the higher viscosity in the cylinder part of the mixed micelles due to the closer packing of the oppositely charged surfactants. As f_{DTAB} increases and the cylinder part becomes longer, a larger fraction of the dendrimers resides in the cylindrical section. These dendrimers experience a higher viscosity which leads to a lower rate of excimer formation.

To further demonstrate these conclusions, an alternative way was implemented to adjust the size of the cylindrical section of the rod-like mixed micelles by changing the NaCl concentration.

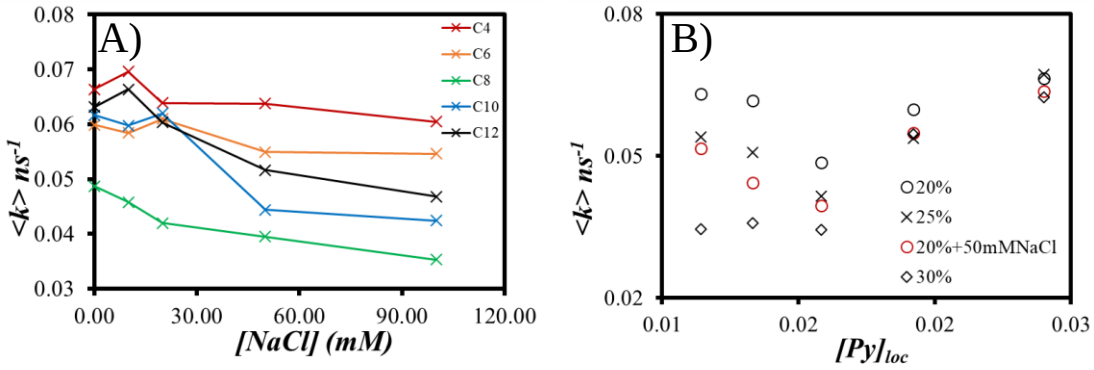

Figure 3. A) Change of <k> with NaCl concentration for PyCX-PAMAM-G0 samples in 40mMSDS and 10mMDTAB(20%DTAB). B) <k> of PyCX-PAMAM-G0 in surfactant aggregates.

The aggregation number (N_{agg}) of the mixed micelles prepared from a 50 mM surfactant mixture with f_{DTAB} equal to 0.20 was determined at NaCl concentrations of 10, 20, 50, and 100 mM by conducting fluorescence experiments to equal 228±3, 255±6, 305±11, and 395±17 respectively. N_{agg} of the mixed micelle increased with increasing NaCl concentration providing a means to continuously adjust the size of the micellar aggregates by simply adjusting the NaCl concentration.

<*k*> was then determined for all the PyCX-PAMAM-G0 samples in the 50 mM surfactant mixtures with f_{DTAB} equal to 0.20 for the same NaCl concentrations of 10, 20, 50, and 100 mM. If the prediction is true that the dendrimers distribute themselves between the more viscous cylindrical section and the less viscous hemispherical ends of the rod-like micelles, <*k*> should decrease with increasing micelle size, and the checkmark pattern should become less pronounced as reflected by an increase in ϕ. The <*k*>-*vs*-$[Py]_{loc}$ trends shown in Fig. 3B indicate that the checkmark pattern becomes less pronounced for the 50 mM mixed surfactant mixture with f_{DTAB} = 0.20 upon adding 50 mM NaCl. The trends obtained for the mixed micelles with f_{DTAB} equal to 0.20, 0.25, and 0.30 are also presented in Figure 3B for comparison.

CONCLUSION

This study represents the first example in the literature where the conformation of a series of hydrophobically modified PAMAM dendrimers (HM-PAMAM) was successfully characterized experimentally by PEF in DMF, DMSO, and in surfactant aggregates used as lipid membrane mimics. It was enabled by leveraging the high sensitivity of PEF with its ability to report on $[Py]_{loc}$ and the local density of a pyrene-labeled macromolecule through the parameter $\langle k \rangle$ obtained from the global MFA of the fluorescence decays acquired with the PyCX-PAMAM-G0 samples. Linear trends of $\langle k \rangle$-vs.-$[Py]_{loc}$ passing through the origin were obtained for the five PyCX-PAMAM-G0 samples in DMF and DMSO, and for samples with short linkers (X=4,6,8) in all surfactant aggregates, which suggests that the internal segments of dendrimers obey Gaussian statistics under these conditions. The $\langle k \rangle$ value for the dendrimers with longer linker (X=10,12) was observed to significantly deviate from the linear trend. This is a result of a conformational inversion that happens in pure micelles or similar environments because the long alkyl linker tends to interact more strongly with the more hydrophobic interior of the micelles. Such conformational change was demonstrated to be absent in the cylindrical part of the mixed micelles formed by the close packing of the SDS and DTAB molecules present in a 1:1 ratio by varying the DTAB content or NaCl concentration. In both experiments where the length of the cylindrical section of the mixed micelle increasing with increasing DTAB content or NaCl concentration, the checkmark pattern became less pronounced as reflected by an increase in ϕ. In conclusion, PEF-based experiments presented herein provide a new experimental means to study at the molecular level the interactions between HM-PAMAM and surfactant aggregates used as lipid membrane mimics. Such experiments would be extremely challenging to conduct with the conventional characterization methods applied to probe macromolecular conformation.

REFERENCES

1. S. Choudhary, *et al.* Impact of dendrimers on solubility of hydrophobic drug molecules. *Front Pharmacol*, **2017**, *8*, 261.
2. L. Albertazzi, *et al.* In vivo distribution and toxicity of PAMAM dendrimers in the central nervous system depend on their surface chemistry. *Mol Pharm*, **2013**, *10*, 249-260.
3. Fox LJ, Richardson RM, Briscoe WH. Pamam dendrimer - cell membrane interactions. *Advances in Colloid and Interface Science*. **2018**, *257*, 1–18.
4. Bergström M, Pedersen JS. Small-angle neutron scattering (SANS) study of aggregates formed from aqueous mixtures of sodium dodecyl sulfate (SDS) and dodecyltrimethylammonium bromide (DTAB). *Langmuir*. **1998**, *14*, 3754–3761.
5. Patel, S.; Duhamel, J. Macromolecular Conformation of Low Generation PAMAM Dendrimers Probed by Pyrene Excimer Formation. *Macromolecules* **2023**, *56*, 4012– 4021,

KRISTIJAN LULIC
Chemistry
Waterloo

Improving the Sensitivity of Pyrene Excimer Formation for Persistence Length Determination of Poly(alkyl methacrylate)s

Improving the Sensitivity of Pyrene Excimer Formation for Persistence Length Determination of Poly(alkyl methacrylate)s

Kristijan Lulic and Jean Duhamel*

Institute for Polymer Research, Waterloo Institute for Nanotechnology, Department of Chemistry, University of Waterloo, ON N2L 3G1, Canada

INTRODUCTION

The persistence length (l_p) of a polymer provides a quantitative measure of its ability to bend on a molecular level, influencing the mechanical properties observed for the bulk material.[1] Polymers possessing a larger persistence length will adopt an extended conformation in solution, resulting in a stiffer material with a larger modulus compared to polymers with a lower persistence length, that adopt a more coiled conformation.[2] Similarly to other physical quantities such as the glass transition temperature (T_g) or modulus, monomer types and their molar fraction incorporated in a copolymer determine the flexibility of the resulting polymer.[3] Structure-property relationships, such as that existing between the composition and flexibility of a copolymer are extremely useful to better understand the behaviour of a material. One such instance pertains to engine oil additives known as pour-point depressants (PPDs), which are typically random terpolymers of alkyl methacrylates.[4] Below a threshold temperature known as the pour-point,[5] paraffinic wax crystal growth takes place in the engine oil, which blocks the oil flow and can result in engine failure. PPDs modulate the viscosity of the engine oil at these lower temperatures by disrupting, and redirecting crystal growth through long alkyl side chains that are purposely incorporated into the PPD.[6] These terpolymers also contain shorter alkyl chain segments that act as spacers, increasing the flexibility of the macromolecule, so that it can more closely adhere to the contour of the wax crystals, thus enhancing the effectiveness of the PPD.[7]

Despite its importance in our fundamental understanding of macromolecules, the persistence length of many polymers remains unknown due to many experimental challenges associated with l_p determination. Static light scattering,[8] intrinsic viscosity,[9] or gel permeation chromatography (GPC) experiments are the typical techniques employed to obtain l_p,[10] but their application is plagued with numerous experimental constraints. Light scattering and viscosity experiments require polymers with a narrow molecular weight distribution (MWD), typically generated by living polymerization techniques.[11] Unfortunately, not all monomers can be anionically polymerized, leaving free radical polymerization and its associated broad MWD as the only viable option. In this case, the polydisperse polymer samples may be analyzed using a GPC instrument, equipped with light scattering and viscosity detectors, that separate the sample into monodisperse fractions.[11] However, the polymer must be soluble in the solvent used with the GPC instrument to avoid potential polymer-column interactions that would prevent any further analysis.[12] The determination of l_p with these techniques is based on the same physical principle consisting in probing the local density of a macromolecule through either its radius of gyration or intrinsic viscosity. Since a more flexible macromolecule with a shorter l_p would pack a greater number of

structural units per unit volume than a more rigid macromolecule with a longer l_p, the local density of a polymer can be utilized to determine its l_p by light scattering or viscosity measurements.

In this context, the photophysical phenomenon of pyrene excimer formation (PEF) between an excited and a ground-state pyrene labels covalently attached onto a polymer appears particularly appealing. The rate of PEF has been shown to be directly proportional to the local concentration ($[Py]_{loc}$) of pyrenyl labels in the polymer coil and thus responds to the local density of the polymer in solution in the same manner as light scattering or viscometry experiments do. Furthermore, fitting the fluorescence decay of a polymer randomly labeled with pyrene according to the fluorescence blob model (FBM) yields the number (N_{blob}) of structural units encompassed inside the volume probed by an excited pyrene also called a *blob*. Since a *blob* is the same for a polymer with a flexible or a rigid backbone, the associated N_{blob} is larger or smaller, respectively. Consequently, N_{blob} reflects polymer backbone flexibility and thus l_p.[13]

This correspondence has already been applied to determine l_p for a series of poly(alkyl methacrylate)s (PyC4-PAMAs)[14] and poly(oligo(ethylene glycol methyl ether methacrylate)s (PyC4-PEG$_n$MAs) that were pyrene-labeled through copolymerization of a methacrylate monomer with 1-pyrenebutyl methacrylate.[15] Regardless of chemical functionality, an increase in side chain length resulted in a substantial decrease in N_{blob} reflecting an overall loss in flexibility, and of course, an increase in l_p. However, l_p values for constructs with side chains longer than 18 carbon atoms were obtained with significant error because the polymethacrylate backbone appeared fully extended over the length scale probed by the pyrenyl label linked to the backbone via a four-carbon long spacer and N_{blob} no longer responded to changes in l_p. This lack of sensitivity for stiffer polymethacrylate backbones with longer side chains would be further compounded in more viscous solvents that would be typically obtained at lower temperatures. To address this problem, a series of PAMAs with the alkyl side chains made of 1 to 18 carbons, and three PEG$_n$MAs, where n = 9, 16, and 19 were randomly labeled with 1-pyreneoctyl methacrylate (PyC8MA). The eight carbon-long octyl linker was expected to increase the reach of the pyrenyl label, which should probe a larger *blob* occupied by a larger number (N_{blob}) of methacrylate units. The fluorescence decays of the resulting polymers were acquired and analyzed with the FBM to retrieve their N_{blob} values, which were compared to analogous polymers labeled with the 1-pyrenebutyl derivative affording a shorter four carbon-long linker. For a same structural unit, those constructs labeled with the PyC8MA derivative experienced a significant increase in N_{blob}, demonstrating that the FBM responded adequately to an increase in the length of the linker connecting the pyrenyl moiety to the polymethacrylate backbone. Since N_{blob} decreases with increasing solvent viscosity, the effect of solvent viscosity must be eliminated by working in a solvent whose viscosity approaches 0.74 mPa.s as determined earlier.[16] For this reason, the N_{blob} values of the polymers labeled with 1-pyreneoctyl are currently determined in o-xylene whose viscosity equals 0.76 mPa.s in order to extract l_p.

EXPERIMENTAL

Chemicals: Methyl methacrylate, *n*-butyl methacrylate, *n*-hexyl methacrylate, lauryl methacrylate, stearyl methacrylate, oligo(ethylene glycol) methyl ether methacrylate with an M_n of 500 and 950 g/mol, oligo(ethylene glycol) methyl ether with an M_n of 750 g/mol, monomethyl suberate, oxalyl chloride, pyrene, aluminum trichloride, triethylsilane, trifluoroacetic acid, lithium aluminum hydride, dimethylaminopyridine (DMAP), methacrylic anhydride (MAA), tetrahydrofuran, toluene, *o*-xylene, *N,N*-dimethylformamide, dichloromethane, hydrochloric acid, sodium

hydroxide, azobisisobutyronitrile (AIBN), diethyl ether, and methanol were purchased from Millipore-Sigma and used as received unless otherwise noted.

Synthesis of 1-pyreneoctyl methacrylate: Distilled dichloromethane (DCM, 50 mL) and 2 mL of monomethyl suberate (11.1 mmol) were added to a 100 mL round bottom (RB) flask. The headspace was purged with nitrogen for 15 minutes before addition of 1.2 mL oxalyl chloride (14.5 mmol, 1.3 eq.). After 30 minutes, the excess DCM and oxalyl chloride were gently removed by evaporation with air. The activated acid was then redissolved in 50 mL of DCM, followed by the addition of 6.8 g of molecular pyrene (6.8 g, 33.5 mmol, 3 eq.), and 5.4 g of aluminum trichloride (17.9 mmol, 1.6 eq.). The reaction was left to proceed at room temperature for 30 minutes before being cooled to 0 °C in an ice bath. The excess aluminum trichloride was quenched by slow addition of 1 M HCl. The precipitate was removed from the filtrate by suction filtration and it was then dissolved in 100 mL of trifluoroacetic acid, followed by the careful addition of 5.8 mL of triethyl silane (36.1 mmol, 2.5 eq.). After 2 hours at room temperature, the resulting product was washed thrice with 50 mL additions of cold hexane. The product was then dissolved in 100 mL of tetrahydrofuran (THF) before being added very slowly into a 250 mL RB flask filled with 4.5 g of lithium aluminum hydride (120 mmol, 10 eq.) at 0 °C in an ice bath. The reaction then proceeded at 70 °C under reflux for 2 hours before neutralizing unreacted lithium aluminum hydride with 1 M NaOH in an ice bath. The filtrate was then separated from the precipitate using suction filtration, with the solvent being removed by gentle air flow. The 1-pyreneoctanol product was then dissolved in 50 mL of DCM in a 100 mL RB flask, with 0.037 g of DMAP (0.3 mmol, 0.2 eq.). The headspace was purged with nitrogen for 15 minutes before careful addition of 1.7 mL of MAA (11.4 mmol, 5.0 eq.). The reaction was left to proceed overnight at room temperature. Any unreacted material was removed by a series of liquid-liquid extractions in a 125 mL separatory funnel (1 M NaOH, 1 M HCl, 1 M NaOH) with the product dissolved in the organic DCM layer. The 1-pyreneoctyl methacrylate (PyOcMA) product was then purified by column chromatography using toluene as the solvent.

Synthesis of poly(ethylene glycol) methyl ether methacrylate with M_n of 750 g/mol: Using 50 mL of DCM in a 100 mL RB flask, 2 g of poly(ethylene glycol) methyl ether with M_n equal to 750 g/mol was added with 0.15 g of DMAP (1.2 mmol, 0.2 eq.). The headspace was purged with nitrogen for 15 minutes before careful addition of 6.8 mL of MAA (45 mmol, 5.0 eq.). The reaction was left to proceed overnight at room temperature. Any unreacted material was removed by a series of liquid-liquid extractions in a 125 mL separatory funnel (1 M NaOH, 1 M HCl, 1 M NaOH) with the monomer being dissolved in the organic DCM layer. Excess solvent was removed under a gentle air flow.

Synthesis of poly(alkyl methacrylate)s randomly labeled with PyC8MA: A series of PyC8-PAMAs with side chains of n = 1, 4, 6, 8, 12, and 18 carbons were prepared by free radical copolymerization of the corresponding alkyl methacrylate and PyC8MA in toluene at 65 °C, using AIBN as the initiator. Preferential incorporation of either the monomer or PyC8MA, otherwise referred to as compositional drift, was avoided by stopping the copolymerization before the conversion reached 20%. The conversion was monitored by ^{1}H NMR, and once an appropriate conversion was achieved, the reaction was terminated by exposure to air. The resulting polymer was then purified by several precipitations in chilled methanol, followed by centrifugation. After completing the purification, residual solvent was removed by keeping the polymer sample in a vacuum oven at room temperature overnight. For each homopolymer, several polymer samples were prepared with varying amounts of PyC8MA to generate a series of polymer samples with several pyrene contents.

Synthesis of poly(oligo(ethylene glycol) methyl ether methacrylate)s labeled with PyC8MA: A series of PEG_nMA polymers with side chains of M_n equal to 500, 750, and 950 g/mol were prepared in a similar manner to the PyC8-PAMAs with a few adjustments to account for the difference in chemical composition. The free radical polymerization was conducted at 90 °C in THF, and the polymers were precipitated in chilled diethyl ether.

Characterization of molecular weight distribution and chemical composition of the PyC8-PAMAs and PyC8-PEG$_n$MAs: The number-(M_n) and weight-(M_w) average molecular weights of the polymers were obtained by gel permeation chromatography (GPC). A Viscotek GPC instrument equipped with three 300 × 8 mm^2 PolyAnalytik Superes linear mixed-bed columns (PolyAnalytik, London, ON, Canada), and a 305 triple detection system comprised of a differential refractive index, viscosity, and light scattering detectors was used with THF as the eluent for the PAMA samples. A TOSOH GPC-WS instrument equipped with a refractive index, viscosity and Wyatt DAWN HELEOS multiangle light-scattering detectors and with two TSKgel α-M 13 μm mixed bed columns running with DMSO as the eluent at 70°C was used for the PEG_nMA samples. The pyrene contents of both PyC8-PAMA and PyC8-PEG_nMA samples were determined using a Varian Cary 1 Bio UV Vis spectrophotometer. The concentration of PyC8MA was measured from the absorption of a PyC8-PAMA or PyC8-PEG_nMA solution at 344 nm determined with a 1 cm pathlength cell, and using a molar extinction coefficient of 42,250 $M^{-1}.cm^{-1}$ in THF.[15] Through application of Beer-Lambert's Law, the molar fraction of pyrene-labeled methacrylate units in the homopolymers was determined through Equation 1, where x is the molar fraction of PyC8MA units incorporated in the copolymer, and M and M_{Py} are the molar mass of the repeating structural unit and PyC8MA, respectively.[16] The pyrene content in terms of mole of pyrene per gram of polymer is denoted as λ_{Py}, obtained from an absorbance measurement carried out for a solution prepared with a known mass of polymer.

$$x = M/(M - M_{Py}+\lambda_{Py}^{-1}) \quad (1)$$

Fluorescence Analysis: Fluorescence measurements were conducted for solutions of the homopolymers in THF with a pyrene concentration of 2.5 μM. Samples were degassed under a gentle nitrogen flow for 30 minutes prior to measurement to eliminate oxygen, a known fluorescence quencher. Steady-state fluorescence spectra were obtained from 350 to 600 nm with the excitation wavelength set at 344 nm. The monomer and excimer fluorescence decays were acquired using a time-resolved fluorometer from HORIBA to excite the solutions at 344 nm and monitoring the emission at 379 nm and 510 nm, respectively. The FBM was then applied to globally fit the monomer and excimer fluorescence decays to determine N_{blob}, calculated through Equation 2, where f_{Mfree} is the molar fraction of unquenched monomer detected in the fluorescence decay of the pyrene monomer, $<n>$ is the average number of ground-state pyrenes within a *blob*, and x is the pyrene content of the sample determined with Equation 1.[15]

$$N_{blob} = (1-f_{Mfree})\times<n>/x \quad (2)$$

RESULTS AND DISCUSSION

A series of poly(alkyl methacrylate)s with side chains of 1, 4, 6, 8, 12, and 18 carbons and poly(oligo(ethylene glycol) methyl ether methacrylate)s with side chains of 9, 16, and 19 ethylene glycols randomly labeled with a 1-pyreneoctyl derivative were prepared by free radical polymerization. For each side chain length, several polymers were prepared with pyrene contents ranging between 2 and 12 mol%, in addition to a model compound with a pyrene content of less

than 1 mol% to determine the monomer lifetime. The pyrene contents were determined by UV-Vis absorption. The fluorescence decays were obtained by time-resolved fluorescence and analyzed with the FBM in order to determine N_{blob} for the samples, which was then plotted as a function of the pyrene content in Figure 1A. The constancy of N_{blob} with pyrene content demonstrates that the incorporation of the large 1-pyreneoctyl group does not affect the conformation of the polymer, as N_{blob} would drift to higher values if the large 1-pyreneoctyl derivative would significantly slow down backbone diffusion. These N_{blob} values were plotted in Figure 1B as a function of the molar mass of a structural unit (MW_{SU}) for the PyC4- and PyC8-labeled polymers to demonstrate that N_{blob} increased when the length of the linker connecting the pyrene moiety to the polymethacrylate backbone increased from 4 for 8 carbons. The increase in N_{blob} reflected the sensitivity of these fluorescence measurements to changes in the linker length used as a molecular parameter to adjust the N_{blob} value.

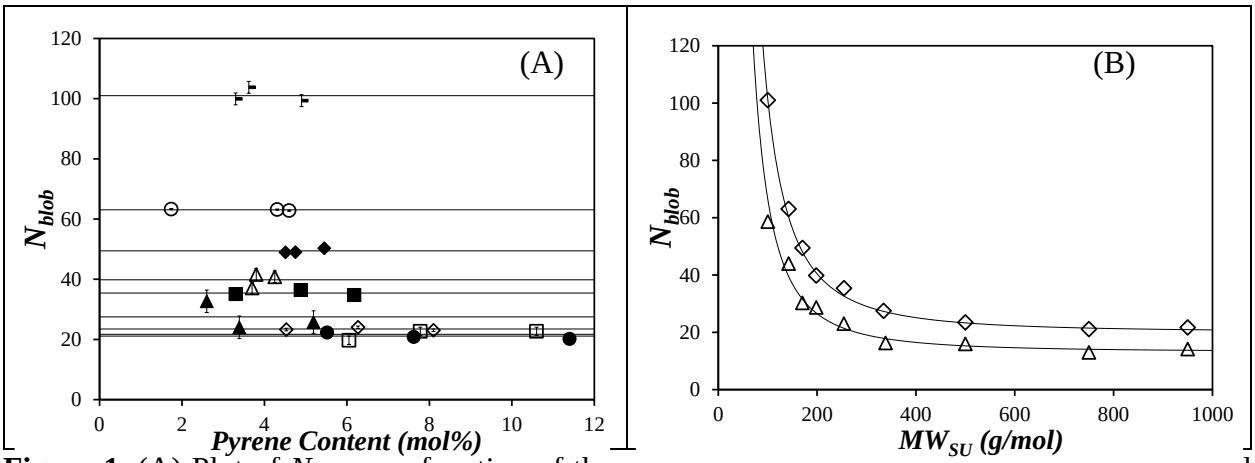

Figure 1. (A) Plot of N_{blob} as a function of the pyrene content in THF for the PyC$_8$-PAMA and PyC$_8$-PEG$_n$MA samples with varying side chain lengths (C$_1$MA, (▪)), (C$_4$MA, (○)), (C$_6$MA, (◆)), (C$_8$MA, (△)), (C$_{12}$MA, (■)), (C$_{18}$MA, (▲)), (PEG$_9$MA, (◇)), (PEG$_{16}$MA, (●)), (PEG$_{19}$MA, (□)). (B) Plot of N_{blob} as a function of repeating unit structural unit molecular weight for homopolymers in THF labeled with 1-pyreneoctyl methacrylate (◇), and 1-pyrenebutyl methacrylate (△).

The homopolymers labeled with a 1-pyreneoctyl and 1-pyrenebutyl derivative both exhibit a decrease in N_{blob} with increasing backbone rigidity and increasing MW_{SU} as indicated in Figure 1B. The increased extension of the polymethacrylate backbone induced by steric hindrance between the longer side chains led the excited dyes to probe a smaller volume within the polymer coil associated with a smaller N_{blob} value. Furthermore, both traces displayed a plateau region for MW_{SU} values greater than 500 g/mol, which is indicative of a fully extended chain. The N_{blob} values recovered with the PyC8-PAMA and PyC8-PEG$_n$MA samples are consistent with an increased reach of the 1-pyreneoctyl derivative inside the polymer coil, which should improve the determination of l_p from the N_{blob} values.

CONCLUSIONS

A key parameter for assessing the flexibility of a polymer is its persistence length, but the stringent requirements associated with the more traditional techniques used to characterize l_p limit its widespread determination, and as a result, the l_p of many polymers remains unknown. Previous work has demonstrated that PEF is a viable method to determine the persistence length of randomly

labeled, polydisperse, linear polymers based on the FBM analysis of fluorescence decays acquired with pyrene-labeled polymers. This research furthers this work by extending the length of the pyrene linker to probe a larger volume, in order to assess the persistence length of stiffer polymers in higher viscosity solvents typically observed at lower temperatures. The N_{blob} values retrieved from the FBM analysis were compared to those obtained earlier with the same homopolymers labeled with a 1-pyrenebutyl label with a short four carbon-long linker to illustrate how the increase in linker length is associated with an increase in the *blob* volume and the number (N_{blob}) of structural units inside it. PEF, in tandem with other characterization techniques may allow the determination of l_p for macromolecules of industrial importance such as the PAMAs investigated in the present study.

REFERENCES

(1) Mantelli, S.; Muller, P.; Harlepp, S.; Maaloum, M. Conformational Analysis and Estimation of the Persistence Length of DNA Using Atomic Force Microscopy in Solution. *Soft Matter* **2011**, *7*, 3412.

(2) Gardel, M, L. Synthetic Polymers with Biological Rigidity. *Nature* **2013**, *493*, 618 – 619.

(3) Li, T.; Li, H.; Wang, H.; Lu, W.; Osa, M.; Wang, Y.; Mays, J.; Hong, K. Chain Flexibility and Glass Transition Temperatures of Poly(n-alkyl (meth) acrylate)s: Implications of Tacticity and Chain Dynamics. *Polymer* **2021**, *213*, 123207.

(4) Cui, L.; Li, X.; Ren, F.; Lin, H.; Han, S. A Novel Pour Point Depressant with Diesel Cold-Flow Properties: Performance Evaluation of Benzene-Containing Ternary Copolymers. *Energy* **2024**, *288*, 129607.

(5) Moriceau, G.; Lester, D.; Pappas, G, S.; O"Hora, P.; Winn, J.; Smith, T.; Perrier, S. Well-Defined Alkyl Functional Poly(Styrene-co-Maleic Anhydride) Architectures as Pour Point and Viscosity Modifiers for Lubricating Oil. *Energy Fuels* **2019**, *33*, 7257 – 7264.

(6) Chen, J.; Cui, L.; Xi, B.; Lin, H.; Han, S. Influence of Polymers with Surfactant Properties as Pour Point Depressants on the Cold Flow Properties of Diesel Fuel. *Colloid Surface A* **2023**, *677*, 132390.

(7) Rizvi, S. Q. A. Dispersants.. In *Chemistry and Applications: Lubricant Additives*; Rudnick, L. R., Ed.; CRC Press: Boca Raton: Florida, 2017, pp 249 −255. DOI: 10.1201/9781315120621-3.

(8) Aime, J, P.; Ramakrishnan, S.; Chance, R, R.; Kim, M, W. The Effect of Substituent Groups on Polymer Conformation in Good Solvent: Polyoctene and Polydecene. *J. Phys.* **2008**, *51*, 963 – 975.

(9) Kikuchi, M.; Nakano, R.; Jinbo, Y.; Saito, Y.; Ohno, S.; Togashi, D.; Enomoto, K.; Narumi, A.; Haba, O.; Kawaguchi, S. Graft Density Dependence of Main Chain Stiffness in Molecular Rod Brushes. *Macromolecules* **2015**, *48*, 58 8–588.

(10) Christensen, B, E.; Nygaard Vold, I, M.; Vårum, K, M. Chain Stiffness and Extension of Chitosans and Periodate Oxidised Chitosans Studied by Size-Exclusion Chromatography Combined with Light Scattering and Viscosity Detectors. *Carbohydr. Polym*. **2008**, *74*, 559 – 565.

(11) Rudin, A. *The Elements of Polymer Science & Engineering*; Elsevier Science & Technology Books, 1998.

(12) Yekta, A.; Duhamel, J.; Adiwidjaja, H.; Brochard, P.; Winnik, M. A. Association Structure of Telechelic Associative Thickeners in Water. *Langmuir* **1993**, *9*, 881–883.

(13) Mathew, A. K.; Siu, H.; Duhamel, J. A Blob Model to Study Chain Folding by Fluorescence. *Macromolecules* **1999**, *32*, 7100 – 7108.

(14) Farhangi, S.; Weiss, H.; Duhamel, J. Effect of Side Chain Length on the Polymer Chain Dynamics of Poly(Alkyl Methacrylate)s in Solution. *Macromolecules* **2013**, *46*, 9738 – 9747.

(15) Little, H.; Thoma, J. L.; Yeung, R.; D'Sa, A.; Duhamel, J. Persistence Length and Encounter Frequency Determination from Fluorescence Studies of Pyrene Labeled Poly(oligo(ethylene glycol) methyl ether methacrylate)s. *Macromolecules* **2023**, *56*, 3562 – 3573.

(16) Zaragoza-Galán, G.; Fowler, M. A.; Duhamel, J.; Rein, R.; Solladié, N.; Rivera, E. Synthesis and Characterization of Novel Pyrene-Dendronized Porphyrins Exhibiting Efficient Fluorescence Resonance Energy Transfer: Optical and Photophysical Properties. *Langmuir* **2012**, *28*, 11195−11205.

EVANGELIN SRIDHAR
Chem. Eng.
Waterloo

Kinetics of Bio-Polyesters

Kinetics and Performance of Biobased Polyesters in Enhancing Wood Properties for Sustainable Applications

Evangelin Sridhar, Prof. Leonardo Simon

Institute for Polymer Research & Department of Chemical Engineering, University of Waterloo,

Waterloo, ON, Canada, N2L3G1

Abstract

Biobased polyesters, synthesized from renewable biological resources, offer a sustainable alternative to conventional petrochemical plastics, helping to mitigate environmental impact. These materials, such as polybutylene succinate (PBS) and polybutylene adipate terephthalate (PBAT), are increasingly used in biodegradable packaging and eco-friendly products [1,10]. In this study, we focus on thermosetting biobased polyesters designed with a crosslinked structure to improve thermal and mechanical properties, making them suitable for demanding applications [11]. One promising area for biobased polyester application is in wood modification. Wood, despite its many advantages, suffers from low dimensional stability and susceptibility to environmental degradation, limiting its durability and performance. Recent advancements in wood modification using biobased polyesters aim to chemically link these materials with wood, improving its dimensional stability, fungal resistance, and overall durability [5].

Furthermore, the use of dairy industry by-products, such as whey ultrafiltration (UF) permeate, provides a sustainable resource for producing biobased polyesters. Whey UF permeate, rich in lactose and minerals, has been successfully utilized in the production of high-value chemicals like 5-hydroxymethylfurfural (HMF) [8]. This research leverages the potential of UF permeate to create innovative wood stabilizers through in situ polycondensation reactions with organic acids, aiming to enhance the environmental stability of wood. Preliminary experiments using malic acid, citric acid, and lactose from whey permeate are explored to optimize the polymerization process for improved wood properties.

The primary objective of this study is to investigate the use of biobased polyesters, synthesized from organic acids and whey UF permeate(alcohols), as a method to enhance the dimensional stability of wood. The specific goals include: (1) studying the kinetics of biobased polyester formation through polycondensation reactions involving malic and citric acids with lactose and Whey permeate, (2) evaluating the impact of these polyesters on wood's moisture uptake and dimensional stability, and (3) optimizing the process conditions using thermal and spectroscopic analyses (DSC, FTIR, and TGA) to enhance wood's resistance to environmental changes and degradation. Through these efforts, the project seeks to develop a sustainable, eco-friendly solution for improving wood properties, contributing to the circular economy by utilizing dairy industry by-products.

The methodology for this study involves a comprehensive approach to characterizing and analyzing the materials involved in the wood modification process using biobased polyesters. The moisture content of the key components—Malic acid, Citric acid, lactose, and whey permeate—was measured using an Ohaus MB45 Halogen Moisture Analyzer, ensuring precise moisture removal for subsequent analyses. Fourier-Transform Infrared (FT-IR) spectroscopy was employed

to examine the monomeric spectra of the samples, with pellets prepared by mixing the dried samples with potassium bromide (KBr). This technique enabled the identification of functional groups and structural insights crucial for understanding the polymerization behavior.

Differential Scanning Calorimetry (DSC) was utilized to study the kinetics of polycondensation reactions, focusing on various combinations of Malic acid, Citric acid, lactose, and whey permeate. The samples were analyzed under controlled thermal cycles at different heating rates to capture the thermal transitions, such as melting points and enthalpy changes, critical for determining reaction kinetics. Thermogravimetric analysis (TGA) further complemented the study by assessing the thermal stability of the monomers across a broad temperature range, under nitrogen flow, to identify decomposition points and support the understanding of thermal behavior in the polycondensation process. These combined techniques provide comprehensive data for optimizing the polycondensation reactions for enhanced wood modification.

The moisture content of the monomers was carefully assessed as it directly influences the efficiency of polycondensation reactions and the polymerization process for wood modification. Excessive moisture can lead to incomplete polymerization, affecting the performance of the modified wood. Therefore, effective moisture control is essential for achieving optimal polymerization and ensuring the sustainability of the modification process. FTIR analysis of the monomers provided valuable insight into their molecular structure and functional groups. The spectra revealed that each monomer exhibited distinct functional group characteristics, including C=O stretching for carboxylic acids in malic and citric acids, and O-H stretching for alcohols in lactose and whey permeate. Temperature-dependent changes in the FTIR spectra of these monomers were observed, particularly in their functional group vibrations. For example, in malic acid, peaks associated with hydrogen bonding diminished at higher temperatures, indicating reduced intermolecular interactions. Similarly, the O-H stretching bands of citric acid and whey permeate weakened with increasing temperature, signifying disruption of hydrogen bonding. These thermal effects were consistent with the TGA findings, which showed degradation starting at temperatures of 152°C for malic acid and 172°C for citric acid, providing further understanding of the monomers' stability during thermal treatments.

The thermal behavior of the monomers was thoroughly investigated using thermogravimetric analysis (TGA) and differential scanning calorimetry (DSC). The TGA curves revealed that each monomer had distinct degradation temperatures, which informed the selection of appropriate DSC conditions. For instance, malic acid began degrading at 152°C, guiding the DSC temperature settings to avoid decomposition. The melting behaviors, identified through DSC, revealed that malic acid had a melting point of 132.6°C, while citric acid melted at 155.8°C, lactose at 218.4°C, and whey permeate at 146.4°C. These findings offer valuable insights into the thermal stability of the monomers and their suitability for polymerization reactions. The temperature conditions used in the DSC experiments allowed for an in-depth understanding of the monomers' thermal transitions, ensuring that the reactions proceeded under optimal conditions without exceeding degradation thresholds. These thermal analyses also provide essential data for understanding how these monomers interact during the in-situ polymerization process within wood modification, guiding future research into improving material properties through controlled thermal and chemical treatments.

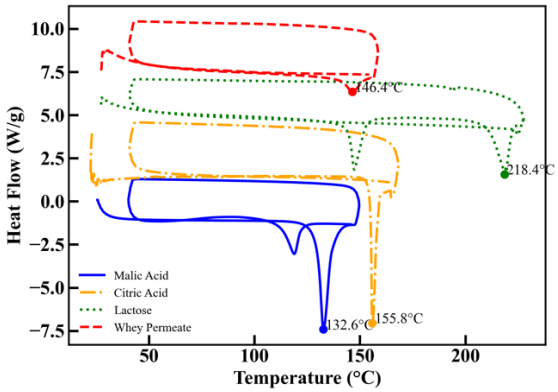

Fig. 1 DSC records of monomers

Differential Scanning Calorimetry (DSC) was used to analyze the thermal behavior of reactions between lactose or whey permeate and biobased acids (malic acid and citric acid), aiming to determine optimal reaction temperatures and quantify enthalpy changes, which reflect energy absorbed or released during the reactions. The optimal reaction temperatures were found to be 150°C for Lactose & Malic Acid and Whey Permeate & Malic Acid, 170°C for Lactose & Citric Acid, and 155°C for Whey Permeate & Citric Acid, ensuring complete reactions and avoiding undesirable side reactions. The enthalpy changes (ΔH) were calculated by integrating the areas under the DSC peaks, revealing higher energy release for Lactose & Malic Acid (175.6 J/g) compared to Lactose & Citric Acid (159 J/g), and greater energy release for Whey Permeate & Malic Acid (118 J/g) than for Whey Permeate & Citric Acid (87.53 J/g). These variations indicate differences in the energy profiles of the acid types and alcohols used. The analysis provided critical insights for optimizing the reaction conditions and further developing sustainable bio-polyester systems. Notably, the absence of endothermic melting peaks in the second heating curve confirmed that the reaction was complete during the first heating, ensuring no leftover reactants and no further reactions in the examined temperature range.

(a) *(b)*

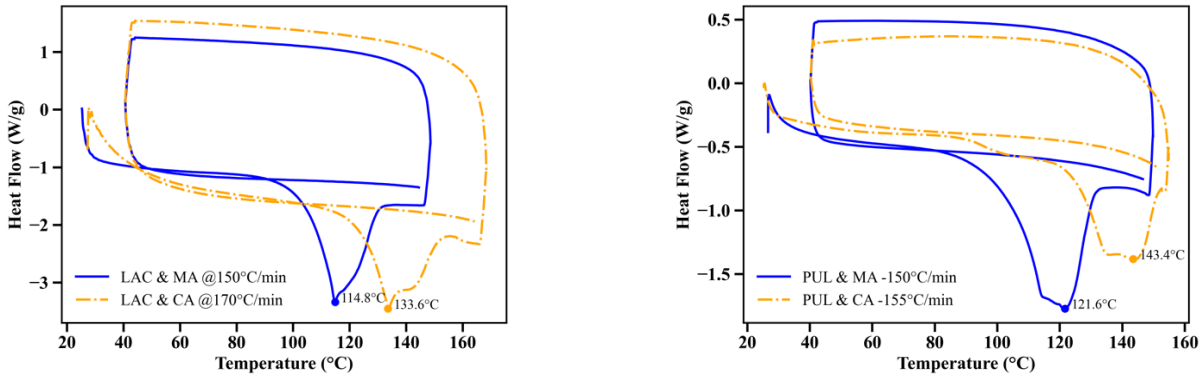

Fig. 2 DSC records of the bio-polyesters: a ***Lactose based Reactions*** and b ***Whey Permeate based Reactions***

These reaction kinetics of Lactose and Whey Permeate with biobased acids (Malic Acid and Citric Acid) are analysed at varying heating rates of 5°C/min, 10°C/min, and 20°C/min, highlighting the importance of heating rate optimization in understanding thermal events and reaction kinetics. Slower heating rates provide higher resolution of thermal events, enabling accurate identification of onset, peak, and endset temperatures, whereas faster rates accelerate reactions but reduce resolution, making precise parameter determination more challenging. The results showed that at lower heating rates (5°C/min), reactions proceeded gradually with better resolution, while higher heating rates (10°C/min and 20°C/min) led to earlier reaction initiation and a higher endset temperature, demonstrating the impact of heating rate on reaction kinetics. For example, the endset temperature in the Lactose and Citric Acid system increased from 151°C at 5°C/min to 158°C at 20°C/min, reflecting the temperature-dependent nature of the reaction kinetics. These findings were visually represented in the Conversion (α) vs Temperature and Heat Flow vs Temperature curves, further illustrating the influence of heating rate on the reaction behavior.

In conclusion, this study highlights the significant role of temperature, heating rate, and reaction kinetics in the development of biobased polyesters for wood modification. The FTIR and DSC analyses revealed critical insights into the molecular behavior and energy profiles of biobased acids and dairy by-products, underscoring the influence of heating rates on the thermal behavior and reaction efficiency. The Lactose & Malic Acid system exhibited the highest energy changes, while the Whey Permeate & Citric Acid system showed the lowest. These findings provide a solid foundation for optimizing polymerization conditions, ensuring the sustainable development of bio-based polyester systems that enhance wood stability and resistance for various applications, particularly in construction.

This research contributes to the advancement of sustainable wood modification technologies, promoting the use of renewable, eco-friendly materials. By refining the reaction kinetics and thermal control parameters, this study offers valuable insights that can lead to more efficient, bio-based alternatives for improving wood properties, ultimately supporting environmental sustainability and the development of greener construction materials.

References:

[1] Aliotta, L., Seggiani, M., Lazzeri, A., Gigante, V., & Cinelli, P. (2022). A brief review of poly (butylene succinate) (PBS) and its main copolymers: Synthesis, blends, composites, biodegradability, and applications. *Polymers, 14*(844). https://doi.org/10.3390/polym14040844

[2] Altgen, M., Awais, M., Altgen, D., Klüppel, A., Mäkelä, M., & Rautkari, L. (2020). Distribution and curing reactions of melamine formaldehyde resin in cells of impregnation-modified wood. *Scientific Reports, 10*, 3366. https://doi.org/10.1038/s41598-020-60418-3

[3] Jelen, P. (1979). Industrial whey processing technology: An overview. *Journal of Agricultural and Food Chemistry, 27*(4), 123-135. https://doi.org/10.1021/jf60224a037

[4] Kay, R., & Westwood, A. R. (1975). DSC investigations on condensation polymers I: Analysis of the curing process. *European Polymer Journal, 11*, 25-30. Pergamon Press.

[5] Karthäuser, J., Treu, A., Larnøy, E., Militz, H., & Alfredsen, G. (2024). Resistance against fungal decay of Scots pine sapwood modified with phenol-formaldehyde resins with substitution of phenol by lignin pyrolysis products. *Holzforschung, 78*(4), 320-328. https://doi.org/10.1515/hf-2023-0119

[6] Kinnertová, E., & Slovák, V. (2018). Kinetics of resorcinol–formaldehyde polycondensation by DSC. *Journal of Thermal Analysis and Calorimetry, 134*, 1215–1222. https://doi.org/10.1007/s10973-018-7532-0

[7] Kurkowiak, K., Mayer, A. K., Emmerich, L., & Militz, H. (2022). Investigations of the chemical distribution in sorbitol and citric acid (SorCA) treated wood—Development of a quality control method on the basis of electromagnetic radiation. *Forests, 13*(151). https://doi.org/10.3390/f13020151

[8] Pandey, S., Dumont, M.-J., & Orsat, V. (2021). Catalytic conversion of whey permeate into 5-hydroxymethylfurfural: Optimization and kinetic modeling approach. *Bioresource Technology, 340*, 125485. https://doi.org/10.1016/j.biortech.2021.125485

[9] Sun, W., Shen, H., & Cao, J. (2016). Modification of wood by glutaraldehyde and poly (vinyl alcohol). *Materials & Design, 95*, 137-144. https://doi.org/10.1016/j.matdes.2016.02.044

[10] Thomas, S., et al. (2013). *Handbook of Biopolymer-Based Materials.* Wiley-VCH Verlag GmbH & Co. KGaA.

[11] Zhang, Q., Song, M., Xu, Y., Wang, W., Wang, Z., & Zhang, L. (2021). Bio-based polyesters: Recent progress and future prospects. *Progress in Polymer Science, 116*, Article 101386. https://doi.org/10.1016/j.progpolymsci.2021.101430

HUNTER LITTLE
Chemistry
Waterloo

Using Time-Resolved Fluorescence to Gain New Insights into the Conformation of DNA Aptamers

Using Time-Resolved Fluorescence to Gain New Insights into the Conformation of DNA Aptamers

Hunter Little,* Karley Zimmer,† Ryan Johnson,† Richard Manderville,† Jean Duhamel*

* Institute for Polymer Research, Waterloo Institute for Nanotechnology, Department of Chemistry, University of Waterloo, ON, N2L 3G1, Canada

† Departments of Chemistry and Toxicology, University of Guelph, 50 Stone Road East, Guelph, Ontario N1G 2W1, Canada

INTRODUCTION

Aptamers are single-stranded oligonucleotides that are synthetically prepared. They are typically developed to bind target ligands with a high degree of affinity and specificity.[1–4] One area of applications being actively investigated is in bio-sensors to identify the presence of drugs or metal ions. One such ligand is tetracycline (TC) which is used as an antibacterial-treatment for human and animal infections and as a growth-promotor in livestock.[5] However, due to its widespread use, TC-resistant bacteria have become an increasing concern.[5] To limit unnecessary exposure and reduce the risk of bacterial resistance, techniques are being developed to detect TC. Using a TC binding aptamer (OTC2) modified to contain an internal fluorophore which responds to the binding of TC enables the detection of low TC concentration in the nanomolar range.[6] The fluorescence response is almost exclusively monitored by steady-state fluorescence (SSF) through the fluorescence spectra acquired before and after binding to the ligand. As such, while the binding equilibrium constant has been reported, little is known about the conformation of the aptamer, which is usually inferred from the Mfold-generated structure.[6]

To characterize the TC/OTC2 system in greater detail, time-resolved fluorescence (TRF) was applied. TRF monitors the emission of the fluorophore as a function of time, and has been used to characterize the conformation of numerous small constructs.[7–9] A series of the OTC2 aptamers consisting of the native aptamer, and aptamers which had been labelled at either the 28th or 40th nucleotide with a specifically prepared thiophene chalcone (Th6In) dye were studied.[10] The Th6In dye was selected to act as a FRET acceptor to TC with the purpose of increasing the sensitivity of detection,[10,11] while the labelling sites were chosen from a separate study indicating a strong FRET response at those positions. The structure of TC, and the Th6In-dye are shown in Figure 1, along with the Mfold predicted structure of the OTC2 aptamer.[6]

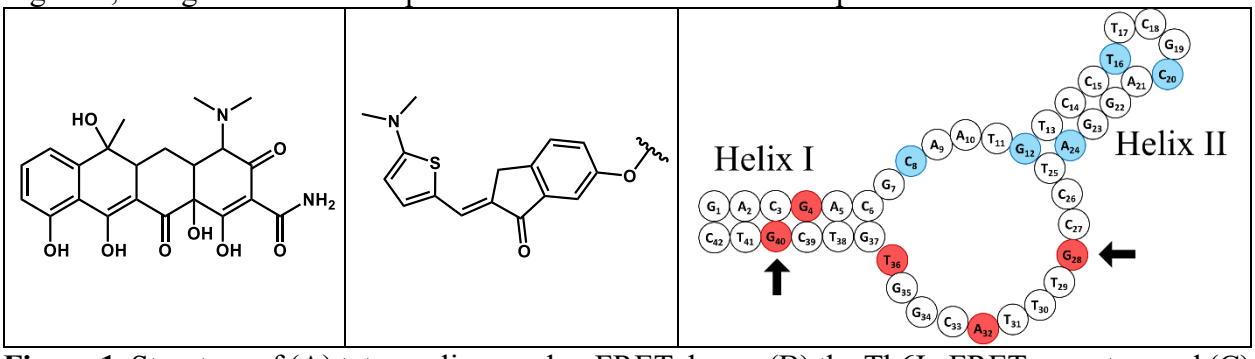

Figure 1. Structure of (A) tetracycline used as FRET donor, (B) the Th6In FRET acceptor, and (C) the Mfold-predicted structure of the OTC2 aptamer with FRET sensitive and FRET insensitive sites identified by red and blue, respectively, and nucleotides #28 and #40 indicated with arrows.

Three TRF experiments were conducted: 1) TRF decay acquisition to measure the average lifetime of the mixture constituted of TC ligand free and bound to the native OTC2 aptamer; 2) TR-FRET

to probe the time-response of TC bound to OTC2 as it undergoes FRET with nucleobases #28 and #40; 3) TRF anisotropy to characterize the OTC2 conformation from its hydrodynamic volume.

These experiments take advantage of the ability of FRET between a fluorescent donor (TC bound to OTC2) and an acceptor (the two Th6In-modified bases in OTC2) to act as a Spectroscopic Ruler reporting on the distance between donor and acceptor.[9] TRF anisotropy yields the rotational time (ϕ) which is proportional to the hydrodynamic volume of the tumbling body.[11] Therefore, a small molecule is expected to tumble quickly and have a correspondingly short ϕ-value, but upon binding to a larger construct, the value of ϕ is expected to increase to reflect the much slower tumbling of the combined complex. Therefore, FRET and TRF anisotropy were used to probe the binding and binding site of TC to the OTC2 aptamer as well as its conformation.

EXPERIMENTAL

TC was purchased from Sigma Aldrich and used as received. OTC2 was purchased from a commercial source while the OTC2-XTh6In samples were prepared using an ABI394 DNA/RNA synthesizer in the Manderville Lab from the University of Guelph. Dry TC was dissolved in a 50:50 water:ethanol solution to generate a solution of 0.4 mM. This TC solution was diluted with 10 mM Tris-HCl buffer to generate a $[TC]_{stock}$ = 0.97 μM for the dilution studies. A second stock solution containing 1.00 μM TC and 15.3 μM OTC2 aptamer was prepared. By mixing the two solutions, individual samples were prepared with a constant [TC] but with [OTC2] ranging between 0.02 and 15 μM. For anisotropy experiments on the native OTC2 aptamer, solutions were prepared at [TC] = 7.2 (±0.1) μM and [OTC2] = 15.0 (±0.1) μM to ensure a 2.1 (±0.1) excess of OTC2 aptamer per TC molecule. Finally, for anisotropy experiments where the Th6In-base was excited to act as a fluorescence probe, samples were prepared at a [OTC2-XTh6In] = 1.93 (±0.03) μM with or without 1.2 (±0.2) μM of TC. All fluorescence decays were acquired with a HORIBA DeltaFlex time-resolved fluorometer. The dyes were excited with delta diode lasers with emission maxima at 336 nm and 479 nm for TC and Th6In, respectively. All fluorescence decays were acquired with 20,000 counts at the decay maximum over 1,024 channels with a time-per-channel of 51.4 ps at 535 nm or 0.102 ns at 580 nm for the TC and Th dyes, respectively

RESULTS & DISCUSSION

The fluorescence decay fits for mixtures of TC and OTC2 acquired over a range of OTC2 concentrations required 2–3 decay times (τ). The longest decay time, τ_3 = 6.1 (±1.5) ns, contributed less than 1 (±1) % to the decays and remained constant within experimental error across all OTC2 concentrations. At high [OTC2], a τ_1 = 1.71 (±0.05) ns decay time was attributed to the TC bound to the aptamer, while at low [OTC2], a much shorter τ_2 = 0.43 (±0.04) ns decay time was attributed to the TC free in solution. These decay times agree well with those reported in the literature for TC bound and free in solution.[12,13] Using Equation 1, the average lifetime ($<\tau_{TC}>$) was calculated; it was found to match the 1.71 ns lifetime of TC bound to the aptamer at [OTC2] > 1 μM which corresponded to a 1:1 OTC2:TC molar ratio. Below the equimolar ratio, $<\tau_{TC}>$ decreased towards the 0.43 ns lifetime of unbound TC. The two main decay times along with $<\tau_{TC}>$ were plotted as a function of concentration of OTC2 in Figure 2A while a plot of the pre-exponential factors are shown in Figure 2B.

$$<\tau_{TC}>=\frac{\sum_{i=1}^{n} a_i \tau_i}{\sum_{i=1}^{n} a_i} \qquad [1]$$

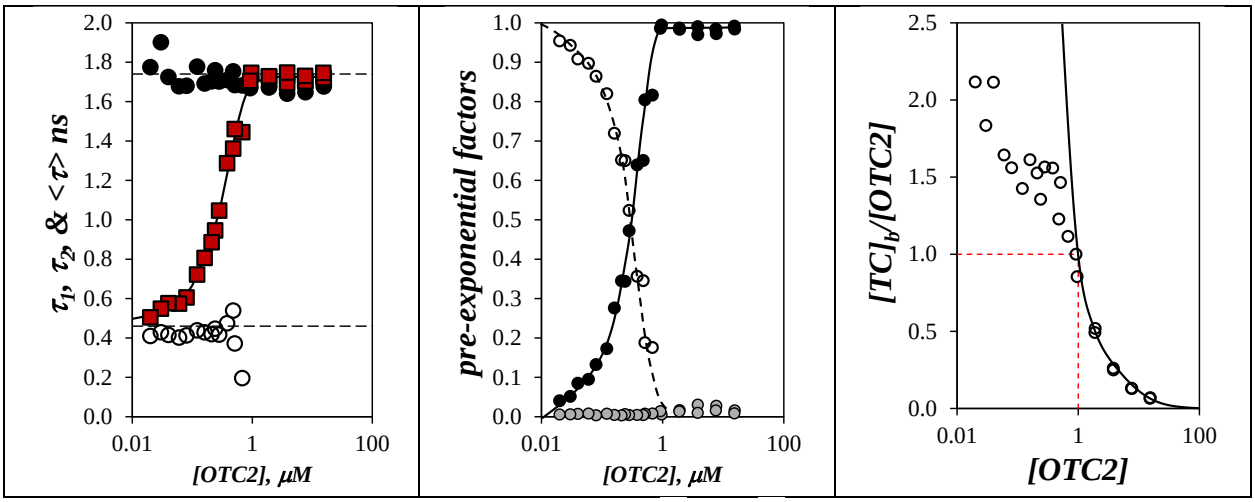

Figure 2. The (A) major contributing decay times (●) τ_1, (○) τ_2, and the average decay time (■) $<\tau_{TC}>$ with dashed lines indicating (bottom horizontal dashed line) $<\tau_{TC}> = 0.45$ ns, (top horizontal dashed line), $<\tau_{TC}> = 1.72$ ns. (B) pre-exponential factors (●) a_1, (○) a_2, and (◍) a_3 retrieved from the analysis of the TC fluorescence decay as a function of the OTC2 concentration. (C) The $[TC]_b/[OTC2]$ ratio plotted as a function of [OTC2] with the red dashed lines indicating the equimolar point were [TC] = [OTC2].

The pre-exponential factors from the TRF decays were then used to determine the concentration of TC bound to the aptamer ($[TC]_b$) which was in turn used to calculate the ratio $[TC]_b/[OTC2]$, as shown in Figure 2C. For [OTC2] > 1 μM, the molar ratio n_{TC}/n_{OTC2} equals $[TC]_b/[OTC2]$ which was to be expected due to the complete binding of TC to the OTC2 aptamer. Below 1 μM, the ratio $[TC]_b/[OTC2]$ is larger than 1 which suggests non-specific binding of TC to the aptamer.

The TR-FRET experiments were conducted by exciting TC and measuring the fluorescence response of TC at 535 nm and the Th6In-modified bases at 580 nm. Since FRET involved coupled kinetics between the donor and acceptor, a decay time in the TC fluorescence decay should be mirrored by a matching rise-time in the Th6In fluorescence decay. A 0.35 ns decay time with a contribution of 71 (±6)% in the TC decay was initially attributed to the dyes undergoing FRET, however no such mirroring rise time was found in the decay of Th6In which would be the case for FRET between TC and the Th6In-modified bases. Instead, the decay of Th6In was described by two decay times of 2.5 (±0.4) ns and 4.5 (±0.3) ns, which both contributed equally to the decay with pre-exponential factors of 50 (±10)% regardless of whether the Th6In-modified base was located at position #28 or #40. The Förster radius (R_o) was determined to equal 3.8 nm by assuming an orientation factor $\kappa = 2/3$. The absence of a 3.5 ns rise time in the Th6In fluorescence decay suggested that FRET occurred instantaneously implying that Th6In at position #28 and #40 were separated from TC by a distance much shorter than R_o. The short 3.5 ns decay time in the TC fluorescence decay could be attributed to a subfraction of dyes undergoing non-instantaneous FRET, with its rise-time being very difficult to detect in the Th6In decay. This conclusion agreed with the SS-FRET results depicted in Figure 1C which suggested that the bases #28 and #40 are close to the TC binding site. A TRF anisotropy study was then undertaken to probe the behavior of the aptamers in more details.

The anisotropy decays were fit according to the previously published procedure where the $I_{VV}(t)$ and $I_{VH}(t)$ decays are both acquired to the same number of counts at the decay maximum to

improve the signal-to-noise ratio for the $I_{VH}(t)$ decay before being fitted globally to retrieve the rotational time (ϕ) and initial anisotropy (r_o).[14] For free TC, and TC bound to the native aptamers, a single rotation time (ϕ_1) was required to fit the anisotropy decays. ϕ for TC alone in solution equaled 0.17 ns. Upon binding to the OTC2 aptamer, ϕ increased from 0.17 ns to 8.3 (±0.5) ns reflecting the much larger hydrodynamic volume of the aptamer compared to TC. This rotational time was then compared to the average rotational times ($<\phi>$) recovered for a series of DNA duplexes[8] as shown in Figure 3 where ϕ and $<\phi>$ were plotted as a function of the equivalent number of base-pairs if all nucleotides were involved in a base pair. If the 42-bp OTC2 adopted a rigid conformation in solution, it was expected to have a rotational time equivalent to that of a 21-bp duplex, which was supported by the fact that the rotational time landed on the calibration curve built with the $<\phi>$ value of the DNA duplexes. To further support this point, the two Th6In-labelled aptamers were also investigated with and without TC, by selectively exciting Th6In. Unlike when TC was used as the fluorescent probe, two rotational times (ϕ_1 and ϕ_2) were required to fit the $I_{VV}(t)$ and $I_{VH}(t)$ decays. The long rotational time, ϕ_1 = 7.7 (±0.6)ns, was attributed to the tumbling of the aptamer due to the good agreement with the rotational time of the aptamer using TC as the probe. The short rotational time, ϕ_1 = 1.5 (±0.2) ns, was attributed to rapid wobbling of the Th6In dye with respect to the aptamer within a 15° cone angle.

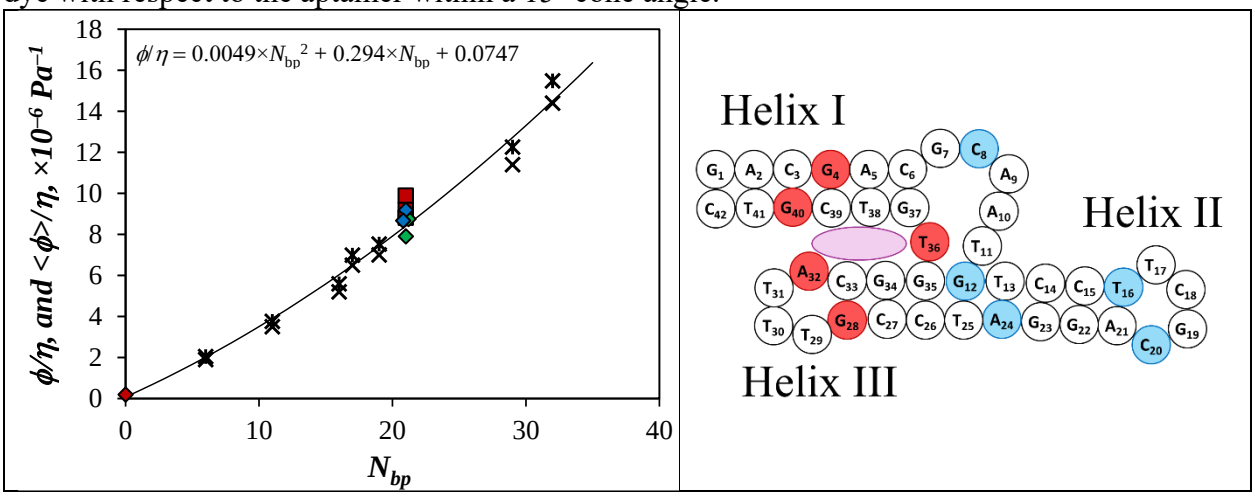

Figure 3. (A) Rotational time of (♦) TC isolated in solution, (■) TC bound to the aptamer and used as a fluorescence probe, (♦) OTC2-28TH with and without TC, (♦) OTC2-40TH with and without TC, compared to the average rotational time of (×) DNA duplexes, plotted as a function of the number of base pairs. One measurement from each of the Th-modified aptamers has been shifted by 0.2 bp for clarity. (B) Proposed structure of the OTC2 aptamer based on fluorescence experiments with FRET sensitive and FRET insensitive sites identified by red and blue, respectively. The proposed site of TC binding is depicted with the purple ellipse.

The results of the fluorescence anisotropy experiments suggest that the OTC2 aptamer has a closed, rigid structure regardless of whether TC is bound or not. While little information could be gleaned from the TR-FRET experiments, the FRET efficiencies determined by SSF could be interpreted to further refine the aptamer conformation. The Mfold-predicted structure of the OTC2 aptamer, shown in Figure 1C, is comprised of two helices (Helix I and Helix II) made of complementary base pairs and connected to each other by open loop regions. This is contradictory to the closed, rigid structure suggested by TRF anisotropy, and the SS-FRET experiments conducted at the University of Guelph which demonstrated that bases #4, 28, 32, 36, and 40 all

showed energy transfer from the TC donor to the Th6In acceptor, which could only occur if they were very close to the site of TC binding. In the Mfold structure, bases 28, 32, and 36 are all located in the loop region whose flexibility would take these bases away from the two bases in Helix I which must be physically close to the TC binding site and are more rigid due to the base pairing in that location. Instead, the FRET data lead to an alternative structure shown in Figure 3B which satisfies the results of both the TRF anisotropy, which suggest a compact, rigid structure, and the SS-FRET which requires the FRET-positive sites to be located in close proximity to the TC binding pocket, shown in purple. In this new structure, the complementary $C_{26}C_{27}G_{28}/C_{33}G_{34}G_{35}$ come together to form Helix III which is colinear with Helix II and capped with the ATTT loop. This new conformation locates the 5 FRET-positive sites around a pocket between Helix I and III which is the proposed TC binding-pocket, while also locating the FRET-inactive sites away from the binding pocket.

CONCLUSIONS

The MFold structure predicted for the OTC2 aptamer consists of two base-paired helices, connected by a disordered loop region. However, investigations done using SS-FRET and TRF anisotropy, challenge this structure. By FRET, the TC donor was determined to be located close to bases #4, 28, 32, 36, and 40, three of which were placed far away in the unstructured loop. Likewise, fluorescence anisotropy demonstrated that, due to the single rotational time of the aptamer with or without the TC ligand, the OTC2 aptamer had a compact structure which disagreed with the loops constituted of an unpaired strand of bases. The new conformation of the aptamer presented here satisfies both the FRET and anisotropy results by located the FRET-active nucleotides in close proximity by generating a third base-paired helix consisted of $C_{26}C_{27}G_{28}/C_{33}G_{34}G_{35}$, subsequently reducing the number of unpaired nucleotides and resulting in a more highly-ordered structure consistent with the single rotational times found for the aptamer.

The work presented here also represents the first example in the literature, where the structure of an aptamer has been probed using TRF techniques. The combined use of TR-FRET and anisotropy presented herein should provide a basis for future studies on other aptamers to either confirm or challenge the structure predicted by computational methods which might not consider all the information collected about aptamers in solution with or without their ligands.

REFERENCES

(1) Wang, T.; Chen, C.; Larcher, L. M.; Barrero, R. A.; Veedu, R. N. Three Decades of Nucleic Acid Aptamer Technologies: Lessons Learned, Progress and Opportunities on Aptamer Development. *Biotechnol. Adv.* **2019**, *37*, 28–50.

(2) Zhu, G.; Chen, X. Aptamer-Based Targeted Therapy. *Adv. Drug Deliv. Rev.* **2018**, *134*, 65–78.

(3) Ellington, A. D.; Szostak, J. W. In Vitro Selection of RNA Molecules That Bind Specific Ligands. *Nature* **1990**, *346*, 818–822

(4) Tuerk, C.; Gold, L. Systematic Evolution of Ligands by Exponential Enrichment: RNA Ligands to Bacteriophage T4 DNA Polymerase. *Science* **1990**, *249*, 505–510.

(5) Chopra, I.; Roberts, M. Tetracycline Antibiotics: Mode of Action, Applications, Molecular Biology, and Epidemiology of Bacterial Resistance. *Microbiol. Mol. Biol. Rev.* **2001**, *65*, 232–260.

(6) Zhao, Y.; Gao, B.; Chen, Y.; Liu, J. An Aptamer Array for Discriminating Tetracycline Antibiotics Based on Binding-Enhanced Intrinsic Fluorescence. *Analyst* **2023**, *148*, 1507.

(7) Wang, J.; Little, H.; Duhamel, J.; Li, X.; Markandeya, N.; Maurizot, V.; Huc, I. Application of Time-Resolved Fluorescence Anisotropy To Probe Quinoline-Based Foldamers Labeled with Oligo(Phenylene Vinylene). *Macromolecules* **2019**, *52*, 5829–5837.

(8) Duhamel, J.; Kanyo, J.; Dinter-Gottlieb, G.; Lu, P. Fluorescence Emission of Ethidium Bromide Intercalated in Defined DNA Duplexes: Evaluation of Hydrodynamics Components. *Biochemistry* **1996**, *35*, 16687–16697.

(9) Stryer, L.; Haugland, R. P. Energy Transfer: A Spectroscopic Ruler. *Biochemistry* **1967**, *58*, 719–726.

(10) Johnson, R. E.; Murray, M. T.; Bycraft, L. J.; Wetmore, S. D.; Manderville, R. A. A Modular Aldol Approach for Internal Fluorescent Molecular Rotor Chalcone Surrogates for DNA Biosensing Applications. *Chem. Sci.* **2023**, *14*, 4832–4844.

(11) Lakowicz, J. R. *Principles of Fluorescence Spectroscopy*, Third.; Springer: NY, USA, 2006.
(12) Hegde, K. R.; Puche, A. C.; Szmacinski, H.; Fuller, K.; Ray, K.; Patel, N.; Lengyel, I.; Thompson, R. B. Fluorescence Lifetime Imaging of Human Sub-RPE Calcification In Vitro Following Chlortetracycline Infusion. *Int. J. Mol. Sci.* **2023**, *24*, 6421.
(13) Mukherjee, M.; Sardar, P. S.; Ghorai, S. K.; Samanta, S. K.; Roy, A. S.; Dasgupta, S.; Ghosh, S. A Comparative Study of Interaction of Tetracycline with Several Proteins Using Time Resolved Anisotropy, Phosphorescence, Docking and FRET. *PLOS ONE* **2013**, *8*, e60940.
(14) Little, H.; Wang, J.; Duhamel, J.; Li, X.; Markandeya, N.; Maurizot, V.; Huc, I. Simplification in the Acquisition and Analysis of Fluorescence Decays Acquired with Polarized Emission for Time-Resolved Fluorescence Anisotropy Measurements. *Anal. Chem.* **2020**, *92*, 668–673.

AUTUMN CHEON
Chem. Eng.
Waterloo

Sustainable Air Filtration Materials Using Biomacromolecular Nanomaterials

Sustainable Air Filtration Materials Using Biomacromolecular Nanomaterials

Autumn Cheon[1,2] and Michael K.C. Tam[1,2]
[1]*Department of Chemical Engineering, University of Waterloo, ON, N2L 3G1, Canada*
[2]*Waterloo Institute for Nanotechnology, University of Waterloo, ON, N2L 3G1, Canada*

Introduction

High efficiency air filtration is a critical technology with applications in a variety of diverse fields. From the maintenance of global public health to environmental remediation to the production of microelectronics and other high precision devices, air filtration contributes immensely to modern life[1]. Unfortunately, most options for high efficiency filtration use non-biodegradable and unsustainable materials such as polypropylene or fibreglass. As an abundant natural material, cellulose is an excellent material for designing sustainable building filters. Processed into nanocrystalline particles, cellulose can be integrated with inexpensive and established traditional filter media to improve particulate removal performance and provide unique functionality[2].

Cellulose nanocrystals (CNCs) are an excellent choice for the stabilization of emulsions as Pickering emulsifiers. CNC Pickering emulsions are well-established in literature and have been used to construct hierarchical structures and generate superhydrophobic surfaces. Expanding on the engineering of 3D surfaces with a combination of micro- and nano-particles, a low-cost method to prepare reusable and biodegradable porous materials with effective particulate removal efficiencies and low airflow resistance can be developed. Natural materials such as woven cotton fabric are a durable substrate for such coatings[3].

Additionally, nanofibrous electrospun materials have been demonstrated to possess excellent air filtration performance and low resistance. By introducing functional cellulosic material to the electrospinning process, many new properties and functions can be generated. Nanoparticulate additives can improve fibre strength and durability, as well as increasing the productivity of electrospinning processes which is a critical consideration in the industrial-scale production of nanomaterials. The use of CNC also offers strategies to introduce new functions, such as antimicrobials, conductivity, and photocatalysis.

Experimental

Emulsion preparation and spray coating: A paraffin wax in water Pickering emulsion is used for spray coating. The aqueous phase was prepared first by dispersing 1 wt% CNC and 0.5 wt% NaCl into water and heating to 80°C. The salt ions screen the strong electrostatic interactions between the anionic CNC particles, improving surface coverage

of the Pickering emulsifier which reduces the resulting emulsion droplet size. Solid paraffin wax was added at a 1:9 wax to aqueous phase weight ratio (10 wt%) and given sufficient time to melt. A mechanical homogenizer (L5M-A, Silverson Machines Inc., Longmeadow, MA, USA) was used to emulsify the solution at 1200 rpm for 10 minutes. The emulsion was finally probe sonicated at 8 W for about 30 seconds.

For the spray application of the coating, a commercial siphon-fed spray gun (22032 118 Siphon Gun; Critter Spray Products, Thorndale, ON, CA) purchased from a local hardware store was used. For consistent operation and the elimination of human error, a mechanical apparatus built from a 3D printer was designed and utilized to precisely control the spray application parameters.

AC electrospinning of polymer-CNC blends: A polyvinyl butyral (Kuraray Mowital B60H) model system with technical grade (96%) ethanol solvent is used for preliminary testing with electrospinning techniques due to the cheap and relatively safe nature of the system. AC electrospinning techniques developed by collaborators at the Technical University of Liberec (Liberec, Czech Republic) were used to spin nanofibres onto a core as a nanofibrous sheath yarn, or into a pure nanofibre yarn. A schematic of the process is reproduced from (Madheswaran, 2021)[5] in *Figure 1*.

Preparation of nanoyarn composite filters: Novel filter morphologies that are enabled by the preparation of nanofibre yarns were investigated. By structuring the yarns on a scaffold, hierarchical morphologies could be constructed which may be beneficial in producing air filters with reduced pressure drop. A cartridge-style filter taking the form of a permeable cylindrical bobbin wound with the composite nanoyarns was prototyped. Composite nanoyarns were directly wound onto storage bobbins upon production, then later rewound onto the filtration cartridges using a custom winding device. The winding density, spacing between nanofibres, and number of layers, among other parameters, are continuously adjustable.

Mechanical strength testing of yarns: The tensile strength of each nanoyarn sample was tested using a mechanical strength testing device consisting of a motorized platform which moves vertically relative to a fixed base plate. Each part has a serrated clamp to hold the test sample on either end without slippage. A load cell continuously measures the vertical force on the clamp and the position of the moving side is controlled, stretching the sample at a controlled rate. The resulting tension force is recorded by the load cell. The target starting length for the samples tested was 30mm.

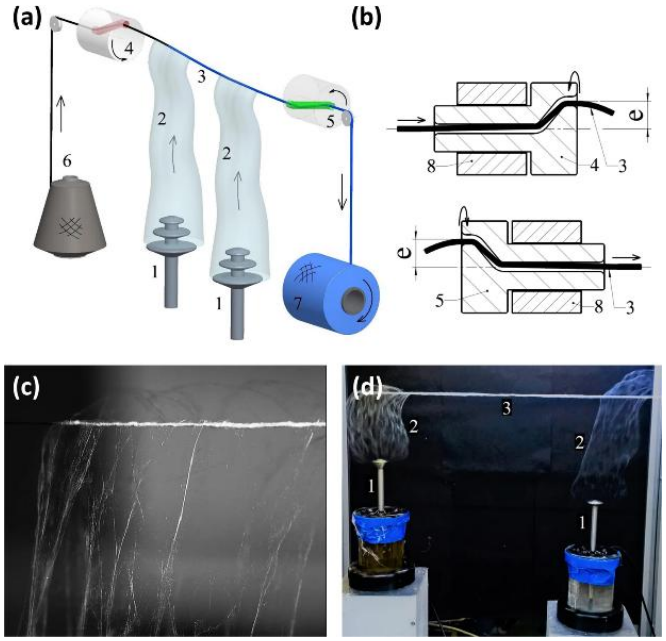

Figure 1. Schematic (a) showing the production of nanofibrous core yarns, the electrodes (1) produce nanofibre plumes (2) collected onto the core thread (3) through a twisting motion (4,5). Reproduced from Madheswaran et al. (Madheswaran, 2021)[5].

Air filter testing: Air filter testing was conducted using the TSI 3160 Automated Filter Tester manufactured by TSI Inc. (Shoreview, USA). Sodium chloride salt particles are generated and classified to produce a stream of challenge particles confined to a virtually monodisperse particle size distribution. The particles are passed through the sample and the difference in particle count upstream and downstream of the filter is measured using condensation particle counters. Differential pressure and flowrate are also recorded. The use of condensation particle counters allows for low challenge particle concentrations and precise characterization of very high efficiency filters (up to 99.999999% efficiency). For testing of cartridge-style filters, a specialized adapter is used to direct airflow through the sample.

Results and Discussion

Spray coated textiles present an interesting route for the production of moderate-efficiency air filters with very simple equipment. Preliminary data to be presented in my talk demonstrates improved air filtration characteristics owing to the modified structure of the filter medium, as evident in microscopy shown in *Figure 2*. In addition to the benefits demonstrated in the work to date, this platform shows particular promise for the addition of functionalized cellulose, where hydroxyl functional groups on cellulose are leveraged to modify and incorporate a variety of advantageous properties such as charge, antimicrobiality, photocatalytic activity, and gas adsorption.

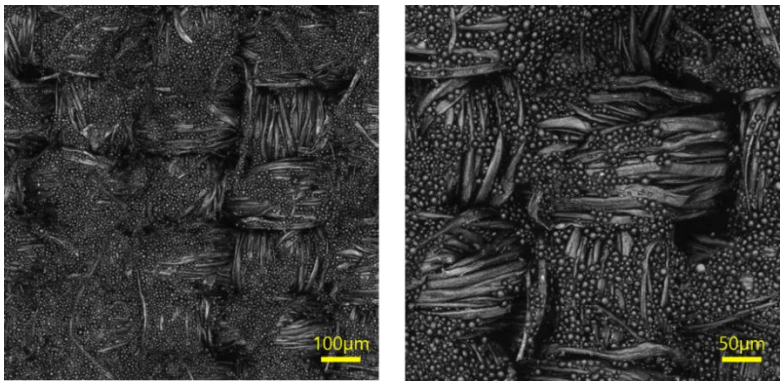

Figure 2. Confocal microscopy showing wax emulsion coated textiles.

Results of the mechanical strength testing of elecrospun nanofibre yarn demonstrates that the addition of CNC into electrospun nanofibrous materials produced under similar electrospinning parameters can withstand more force before breaking. This enables their processing into stronger and more complex structures through procedures like braiding, which is difficult with unreinforced nanoyarns as they are too weak to withstand the braiding process. The mechanical strength testing of the nanofibres yielded a plot of tension force of each sample against the net deformation of the sample. The results were then analyzed by determining the maximum force held by the fibre before failure and the deformation at which the failure occurred. The data for all samples tests were compiled into one plot (*Figure 3*), which shows a general tend of increasing toughness with the addition of CNC.

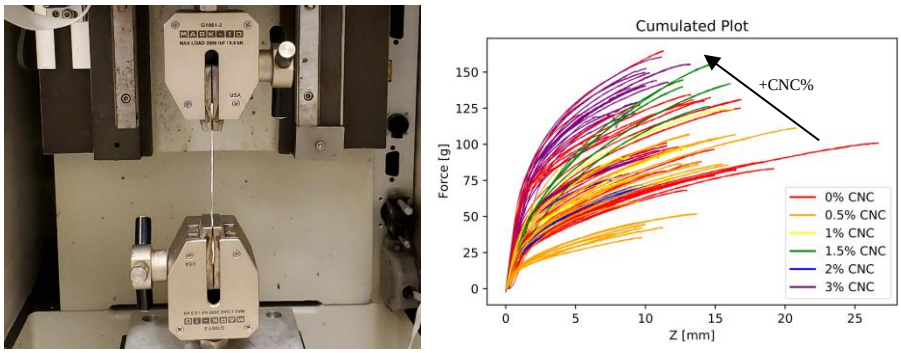

Figure 3. Mechanical strength testing of CNC-reinforced nanoyarns.

The filter properties of cartridge filters prepared from CNC-reinforced nanofibre yarns is also drastically improved compared to pure PVB nanofibre cartridges as shown in *Table 1*. While the mechanisms remain to be explored, this shows an interesting trend which will be worthwhile to pursue. This difference is possibly attributable to the fibre structure being much looser with the addition of charged CNC which causes the fibres to electrostatically repel one another during the spinning process. Looking at the results, the quality factor (QF) is increased by 109% with the addition of 0.3% CNC, which is an

important measure of filter performance and a drastic change for a small addition of our nanoparticle additive.

Table 1. Confocal microscopy showing wax emulsion coated textiles.

Property	**Pure PVB**	**0.3% CNC**	**% Change**
Resistance [mmH_2O]	41.17	100.4	+144
Penetration [%]	30.73	0.2472	-99.2
QF [mmH_2O^{-1}]	0.029	0.060	**+109**
Mass of NF [g]	0.598	0.572	-4.35
Filter Thickness [mm]	1.49	1.64	+9.73

Conclusions

This work has shown preliminary strategies for the development of sustainable alternatives to ecologically persistent plastics and other fibrous materials used in high performance air filters. Wax emulsion and other spray-based techniques show promise in the production of textile-based filters with moderate air filtration performance, providing a quick and simple route to upgrade the air filtration properties of any textile without requiring industrial infrastructure. Future work includes the inclusion of additional functionality including antimicrobiality, photocatalysis, and gas adsorption through the use of modified CNC.

Electrospinning in particular is a valuable technology for the design of nanofibrous materials with excellent air filtration properties. Enhancements in the mechanical and filtering properties of the resulting nanofibrous materials is a promising area of study which needs further exploration. In the future, we would also like to explore the use of sustainable polymer systems including polylactic acid, polycaprolactone, and cellulose acetate instead of our model system using polyvinyl butyral.

References

[1] M. W. First, "Hepa Filters," *Journal of the American Biological Safety Association*, vol. 3, no. 1, pp. 33–42, Mar. 1998, doi: 10.1177/109135059800300111.

[2] D. Trache et al., "Nanocellulose: From Fundamentals to Advanced Applications," *Front. Chem.*, vol. 8, May 2020, doi: 10.3389/fchem.2020.00392.

[3] Y. Habibi, L. A. Lucia, and O. J. Rojas, "Cellulose Nanocrystals: Chemistry, Self-Assembly, and Applications," *Chem. Rev.*, vol. 110, no. 6, pp. 3479–3500, Jun. 2010, doi: 10.1021/cr900339w.

[4] D. Riccardis and M. Federica, "Electrospun Nanofibrous Membranes for Air Filtration: A Critical Review," *Compounds*, vol. 3, no. 3, Art. no. 3, Sep. 2023, doi: 10.3390/compounds3030030.

[5] D. Madheswaran et al., "Composite yarns with antibacterial nanofibrous sheaths produced by collectorless alternating-current electrospinning for suture applications," Journal of Applied Polymer Science, vol. 139, no. 13, p. 51851, 2022, doi: 10.1002/app.51851.

NOAH GALLANT
Chemistry
Waterloo

Characterizing the Size and Structure of Pyrene-Tagged SDS and DTAB Micelles

CHARACTERIZING THE SIZE AND STRUCTURE OF PYRENE TAGGED SDS AND DTAB MICELLES

Presented By: Noah Gallant
Supervisor: Dr Jean Duhamel

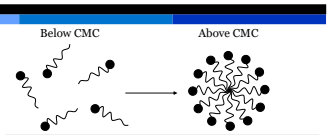

Sodium Dodecyl Sulphate (SDS)	Dodecyl Trimethyl Ammonium Bromide (DTAB)
Anionic Surfactant	Cationic Surfactant
N_{agg} of 71	N_{agg} of 51
CMC of 8 mM	CMC of 15 mM

CMC - concentration at which micelles begin to form
N_{agg} - number of surfactant molecules per micelle

Pyrene Excimer Formation in Time -Resolved Spectroscopy

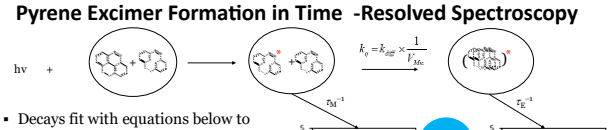

- Decays fit with equations below to obtain <n>, the average number of dyes per micelle (<n> = –ln(f_{Mfree}))

$$[Py^*] = [Py^*]_o \times \left[f_{Mdiff} \times \sum_{i=1}^{\infty} a_i e^{-\frac{t}{\tau_i}} + f_{Mfree} e^{-\frac{t}{\tau_M}}\right]$$

$$[Py^*] = [Py^*]_o \times \left[\sum_{i=1}^{\infty} \frac{\langle n \rangle^i e^{\langle n \rangle}}{i!} e^{-\left(\frac{1}{\tau_M} + ik_q\right)t}\right] + e^{-\langle n \rangle} e^{-\frac{t}{\tau_M}}$$

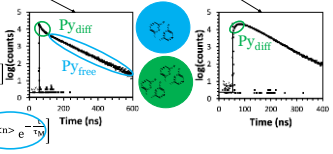

Determining N_{agg}

$$N_{agg} = \frac{[\text{Surfactant in micelle}]}{[\text{Micelle}]} = \text{Slope} \times ([\text{Surf}] - CMC_{SDS} - [DTAB]_{free})$$

N_{agg} of 50 mM 90% SDS 10% DTAB

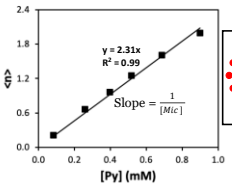

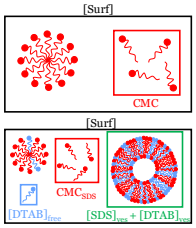

- N_{agg} calculation:

N_{agg} = slope × ([Surfactant] − $[DTAB]_{free}$ − CMC_{SDS})
$N_{agg} = 2.31\ mM^{-1} \times (50\ mM - 0.05\ mM - 8\ mM)$
$N_{agg} = 97$

Analyzing Micelle Size and Structure

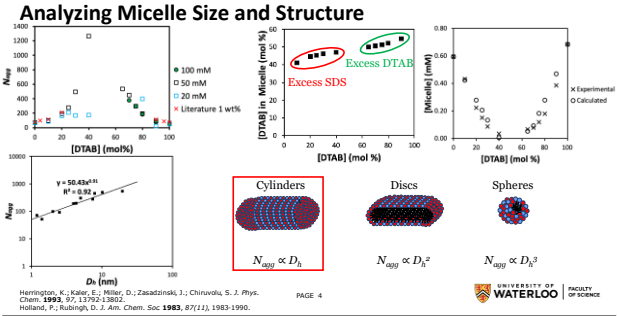

Cylinder Self -Assembly Mechanism

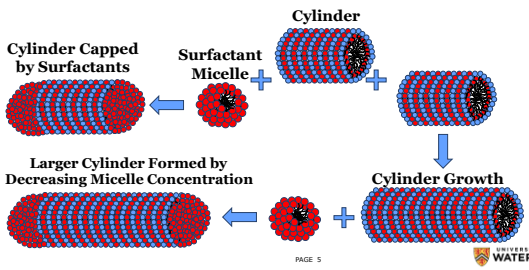

Comparing with Published Results

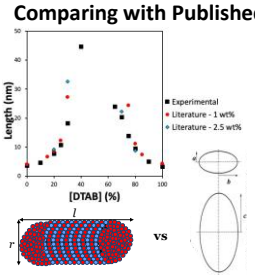

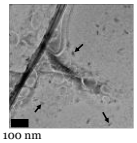

Conclusions

- Approaching a 1:1 surfactant composition favors the formation of larger micelles
- Mixed micelles appear to be cylindrical in structure

Future Work

- Determine N_{agg} for 10 – 65% DTAB at 100 mM
- When completed redo measurements at 20 mM
- Obtain additional TEM images

DREW DAVIDSON
Chem. Eng.
Waterloo

Protecting Firefighters from Cancer through Multifunctional Electrospun Nanocomposites

Protecting Firefighters from Cancer through Multifunctional Electrospun Nanocomposites

30/04/25

Drew Davidson

Kamkar Lab Group - Multiscale Materials Design Lab

ArcticEdge Technologies

Cancer-free Fire Gear

Problem and Goal

- Cancer is attributed to Per/Polyfluorinated Alkyl Substances (PFAS) in firefighting suits [1]
- Current lack of effective alternatives
- Objective: Replace PFAS based components of firefighter gear with a safe alternative material
  - Primary focus: Moisture Barrier Layer
  - Secondary focus: Outer Shell

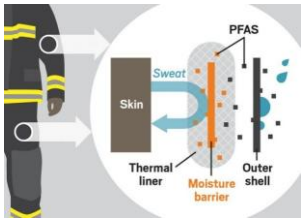

Image: (McElvery, R.,*ACS Chemical and Engineering News*) [2]

Current Approaches

- Silicone-based moisture barrier
- Polyurethane-based moisture barrier
- Hydrocarbon-based outer finishes

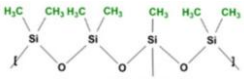

Figure 1: Chemical Structure of Silicone-Based Barrier [3]

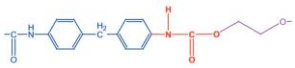

Figure 2: Example Chemical Structure of a Polyurethane Barrier [4]

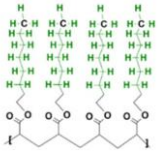

Figure 3: Chemical Structure of Hydrocarbon-Based Finish [3]

Polymer Composite Synthesis Process

- Polymer solution is combined with nanoparticles to enhance flame resistance, chemical stability and impermeability to liquids
- Electrospinning provides control over material porosity, thread diameter to influence breathability and heat transfer
- Alternatively can be coated onto existing textile base

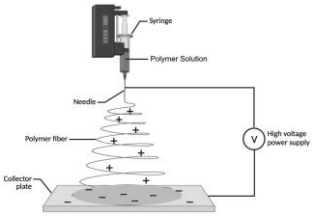

Figure 4: Electrospinning of Polymer Nanocomposite Fiber

Effect of Treatment on Thermal Properties

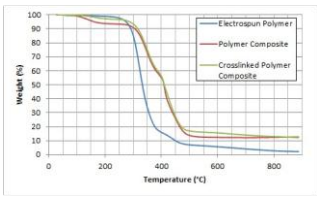

Figure 5: Thermogravimetric Analysis of Polymer Before and After Incorporation of Nanoparticles

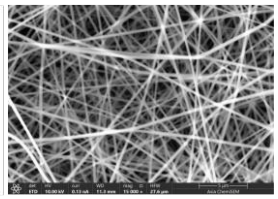

Figure 6: Electrospun Polymer Nanofiber

References

[1] Paul E. Rosenfeld et al., Perfluoroalkyl substances exposure in firefighters: Sources and implications, Environmental Research, Volume 220, 2023, 115164, ISSN 0013 -9351

[2] McElvery, R. (2020, July 1). Protective gear could expose firefighters to PFAS. ACS Chemical & Engineering News, 98(26). Retrieved from https://cen.acs.org/environment/persistent -pollutants/Protective -gear-expose-firefighters-PFAS/98/i26.

[3] Mazumder, Nur-Us-Shafa & Lu, Jingtian & Hall, Andrew & Kasebi, Arash & Girase, Arjunsing & Masoud, Farzaneh & Stull, Jeffrey & Ormond, Bryan. (2023). Toward the future of firefighter gear: Assessing fluorinated and non-fluorinated outer shells following simulated on -the-job exposures. Journal of Industrial Textiles. 53. 1-29. 10.1177/15280837231217401.

[4] Kausar, Ayesha. (2017). Polyurethane/Epoxy Interpenetrating Polymer Network. 10.5772/67678.

KARTHICK RAJ SELVAM
Chem. Eng.
Waterloo

Silk Nanofibers for Drug Delivery: A Solution Blow Spinning Approach

SILK NANOFIBERS FOR DRUG DELIVERY - A SOLUTION BLOW SPINNING APPROACH

Karthick Raj Selvam (PhD student, Dept. of Chemical Engineering)
Supervised by Dr.Tizazu Mekonnen

UNIVERSITY OF WATERLOO | FACULTY OF ENGINEERING

BACKGROUND AND MOTIVATION

APPLICATIONS
- Sustained Drug Release
- Wound Healing
- Tissue Regeneration
- Cosmetic delivery

PROPERTIES OF SILK NANOFIBER
- Biocompatible
- Biodegradable
- High surface area
- Good Mechanical strength
- Thermal and chemical stability
- Low immunogenicity
- Easy functionalization

ADVANTAGES OF SBS
- ✓ Cost effective
- ✓ Scalability
- ✓ High throughput
- ✓ Energy efficient
- ✓ Environment Friendly

UNIVERSITY OF WATERLOO | FACULTY OF ENGINEERING

METHODS – SERICIN EXTRACTION

METHOD I	METHOD II	METHOD III
Without high temperature/pressure/ chemicals	Using Autoclave	Using sodium carbonate
40 hours	3 hours	2 hours
High energy consumption	High energy consumption	Low energy consumption
Incomplete removal	Incomplete removal	Complete removal
No degradation	Degradation might occur	No degradation

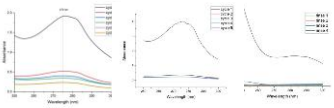

UV Analysis for checking the presence of sericin after each treatment cycle

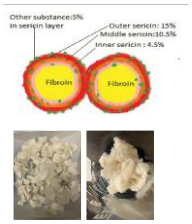

Before & After sericin removal

UNIVERSITY OF WATERLOO | FACULTY OF ENGINEERING

METHODS – OBTAINING REGENERATED SILK FIBROIN

(i) Silk fibers after sericin removal

(ii) Dissolved in 9M LiBr to remove impurities

Phase separation using ethanol

(iii) Regenerated fibroin separated from LiBr

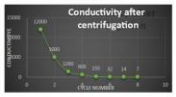

(iv) Centrifuged till all residual ions are removed

(v) Fibroin paste obtained after centrifugation

(vi) Freeze drying

(vii) RSF powder

UNIVERSITY OF WATERLOO | FACULTY OF ENGINEERING

SOLUTION BLOW SPINNING

Rheology to determine the appropriate solution concentration

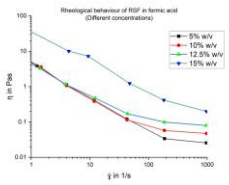

Solution Blow spinning setup

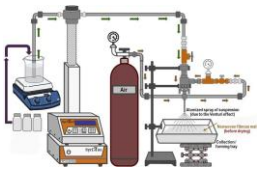

UNIVERSITY OF WATERLOO | FACULTY OF ENGINEERING

CONCLUSION AND FUTURE PLAN

Silk Nanomat obtained through SBS

Solution blow spinning is shown to be a promising method to produce non -woven Regenerated silk nanofiber mats

FUTURE PLAN
- ❑ Obtain silk nanofibers with combinations of CNC and chitosan nanoparticles for enhanced mechanical and anti-microbial properties
- ❑ Introduce drug nanoparticles (ex, curcumin) in the spinning solution and obtain functionalized nanomats

UNIVERSITY OF WATERLOO | FACULTY OF ENGINEERING

MAGGIE WONG
Chem. Eng.
Waterloo

Engineering Biomimetic Strain-Stiffening into Polyacrylamide Hydrogels

ENGINEERING BIOMIMETIC STRAIN-STIFFENING INTO POLYACRYLAMIDE HYDROGELS

04/30/2025

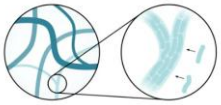

2025 IPR Symposium

Maggie Wong, MASc Candidate
Chemical Engineering

Supervisor: Dr. Elisabeth Prince

UNIVERSITY OF WATERLOO | FACULTY OF ENGINEERING

THE EXTRACELLULAR MATRIX (ECM)

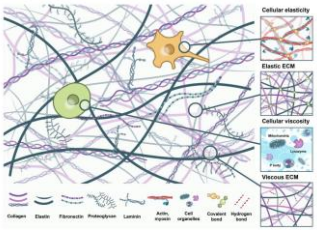

Liu, Z., Ling, X. D., Liang, K., Chen, Y., Niu, Y., Sun, L., Li, J., & Du, Y. (2024). Viscoelasticity of ECM and cells—Origin, measurement and correlation. *Mechanobiology in Medicine* , *2*(4), 100082. https://doi.org/10.1016/j.mbm.2024.100082

UNIVERSITY OF WATERLOO | FACULTY OF ENGINEERING

POLYACRYLAMIDE (PAAm) HYDROGELS

- High flexibility for functionalization
- Tunable mechanical properties
- Biocompatible

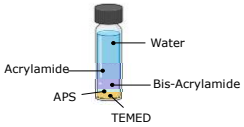

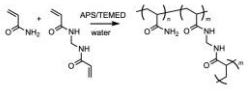

How can we modify PAAm hydrogels to achieve ECM-mimicking properties?

Mitra, F., & del Campo, A. (2024). Polyacrylamide Hydrogels as Versatile Biomimetic Platforms to Study Cell–Materials Interactions. *Advanced Materials Interfaces*, *11*(34), 2400404. https://doi.org/10.1002/admi.202400404

UNIVERSITY OF WATERLOO | FACULTY OF ENGINEERING

HYPOTHESIS 1:

An **increase in crosslinking density** reduces the excess length of the chains that can be pulled out under strain, resulting in strain-stiffening of the hydrogel network under shear deformation.

Low Crosslinking Density

High Crosslinking Density

UNIVERSITY OF WATERLOO | FACULTY OF ENGINEERING

HYPOTHESIS 2:

Introducing charges into the polymer backbone causes electrostatic repulsion of the polymer chains, resulting in chain extension and strain-stiffening under shear deformation.

Neutral Gel

Charged Gel

UNIVERSITY OF WATERLOO | FACULTY OF ENGINEERING

HYPOTHESIS 3:

Polymerization using **reversible addition-fragmentation chain transfer (RAFT)** increases network homogeneity, resulting in even stress distribution andstrain-stiffening under shear deformation.

Free Radical Network

RAFT "Living" Network

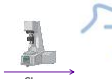

UNIVERSITY OF WATERLOO | FACULTY OF ENGINEERING

DYLAN MCQUARRIE
Chem. Eng.
Waterloo

Leveraging Diels-Alder Adducts for Recyclable Thermosets

LEVERAGING DIELS -ALDER ADDUCTS FOR RECYCLABLE THERMOSETS

3/31/2025

Dylan McQuarrie,
Chemical Engineering

UNIVERSITY OF WATERLOO | FACULTY OF ENGINEERING

Plastic Waste Crisis

In 2019, > 450 million tons of plastic were produced (only ~ 9% of plastics are recycled)

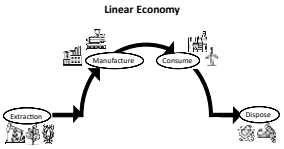

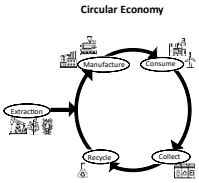

UNIVERSITY OF WATERLOO | FACULTY OF ENGINEERING

Dynamic Covalent Chemistry

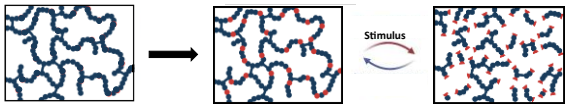

Crosslinked thermoset

Deconstructable crosslinked thermoset

Reprocessable thermoset fragments

Thermoset: Permanent chemical crosslinks, non-recyclable, extremely durable and persistent.

UNIVERSITY OF WATERLOO | FACULTY OF ENGINEERING

Dynamic Covalent Chemistry – Diels-Alder

Diels-Alder (DA) reaction is a thermally reversible reaction:

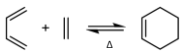

- Environmentally benign method (catalyst free, solvent free)
- Uses current recycling infrastructure (thermally reversible)

UNIVERSITY OF WATERLOO | FACULTY OF ENGINEERING

Dynamic Covalent Chemistry – Diels-Alder

Stage 1: Design thermally cleavable comonomer

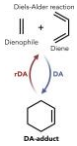

Stage 2: Copolymerize comonomer with various vinyl monomers

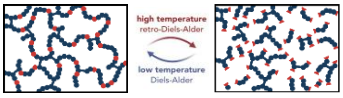

Deconstructable crosslinked thermoset

Reprocessable thermoset fragements

UNIVERSITY OF WATERLOO | FACULTY OF ENGINEERING

Future Outlooks

- Polymerize the thermally cleavable comonomers with various vinyl monomers using various comonomer loading concentrations.
- Characterize degradation of thermally cleavable monomers.
- Characterize the mechanical and thermal properties of the dynamic polymers to the virgin vinyl polymers.
- Illustrate circularity (compression molding, injection molding, etc.)

UNIVERSITY OF WATERLOO | FACULTY OF ENGINEERING